SOLID OXIDE FUEL CELLS DEVELOPED BY THE SOL-GEL

PROCESS FOR OXYGEN GENERATION

BY JOSHUA S. FINCH

A Dissertation submitted to the

Graduate School - New Brunswick

Rutgers, The State University of New Jersey

in partial fulfillment of the requirements

for the degree of

Doctor of Philosophy

Graduate Program in Ceramic and Materials Engineering

Written under the direction of

Professor Lisa C. Klein

and approved by

_____

_____

_____

_____

New Brunswick, New Jersey

May, 2008

ABSTRACT OF DISSERTATION

SOLID OXIDE FUEL CELLS DEVELOPED BY THE SOL-GEL

PROCESS FOR OXYGEN GENERATION

by JOSHUA S. FINCH

Dissertation Director:

Professor Lisa C. Klein

Electrochemical fuel cells convert chemical energy directly to electrical energy through the reaction of a fuel and an oxidant. Solid oxide fuel cells (SOFC) are solid-state devices that operate at temperatures around 800°C, using a solid oxygen electrolyte. The goal of this thesis is to prepare a defect-free solid oxygen electrolyte by a sol-gel process that is capable of (a) functioning in a fuel cell and (b) producing measurable oxygen when operated as an oxygen generator.

Sol-gel processing was chosen for membrane development because it offers a means of applying high-purity layers with controlled doping and a variety of geometries. In this study, the sol-gel process was used to produce yttria-stabilized zirconia (YSZ) electrolyte membranes as well as the electrodes required for an operational fuel cell. Zirconium oxychloride (ZOC) was used as the precursor material for the electrolyte. The YSZ solution was prepared by mixing yttrium nitrate and ZOC in a 50/50 ETOH and water solvent. The reaction was catalyzed with 1.5M NH_4OH. Viscosity and solution

application techniques were varied to monitor the effect on membrane development. The YSZ layer was sintered to full density.

The sol-gel process was used to synthesize supported lanthanum strontium manganate (LSM) electrodes separated by a YSZ electrolyte. The LSM solution was made by mixing strontium nitrate, lanthanum chloride, and manganese acetate solutions. The LSM layers were sintered but were porous. After the membranes were assembled by successive layering and sintering, the membranes and completed fuel cells were characterized using TGA, XRD, FE-SEM, a gas pressurization technique, and electrochemical testing.

The YSZ membrane exhibited a stable tetragonal crystal phase and formed a triple phase boundary (TPB) with the cathode. The three phases are the electrode, the electrolyte, and air. Electrochemical testing showed successful membrane development. Although oxygen production was not measured quantitatively, voltage was produced during hydrogen testing. A maximum voltage of 0.352V was obtained using forming gas as a fuel. The relationship between the TPB and oxygen production is critical. By using the sol-gel process, it is possible to form a TPB where the YSZ electrolyte is dense.

TABLE OF CONTENTS

LIST OF TABLES

LIST OF FIGURES

1.0 INTRODUCTION

Alternative fuels, as defined by the Energy Policy Act of 1992 (EPAct), include ethanol, natural gas, propane, hydrogen, biodiesel, electricity, methanol, and p-series fuels. The act was passed by Congress to reduce U.S. dependence on imported petroleum by requiring certain fleets to acquire alternative fuel vehicles, which are capable of operating on non-petroleum fuels [1-4]. In 2003, President Bush announced a program called the Hydrogen Fuel Initiative (HFI) during his State of the Union Address. This initiative, supported by legislation in the Energy Policy Act of 2005 (EPAct 2005) and the Advanced Energy Initiative of 2006, aims to develop hydrogen, fuel cell and infrastructure technologies to make fuel-cell vehicles practical and cost-effective by 2020 [5, 6]. While many of the methods have been under investigation for decades or even more than a century, bringing focus on these alternative energy sources has greatly accelerated research within the respective technologies. The focus of this research is on a type of fuel cell intended to use hydrogen.

Electrochemical fuel cells produce electricity similar to the idea of how a battery functions. These cells are different from batteries in that they consume reactant, which must be replenished, while batteries store electrical energy chemically in a closed system. Additionally, while the electrodes within a battery react and change as a battery is charged or discharged, a fuel cell's electrodes are catalytic and relatively stable [5]. Essentially, a battery will run "dead" over time while a fuel cell, negating thermal and chemical wear, could theoretically work as long as the reactant can be fed to the system. High temperature fuel cells offer an environmentally friendly technology to convert

gaseous fuels such as hydrogen, natural gas or gasified coal into electricity at high efficiencies. In addition to efficiency, higher than those obtained from the traditional energy conversion systems, a fuel cell provides many other advantages like reliability, modularity, fuel flexibility and very low levels of NO_x and SO_x emissions [7].

In fuel cells, chemical energy is converted directly to electrical energy. The product is water with some unused gases or reactants such as hydrogen and oxygen. A fuel cell with a solid oxide electrolyte operating at high temperatures produces electricity. This is known as a solid oxide fuel cell (SOFC). The same solid oxide electrolyte can be used to produce oxygen that is up to 99.1% pure which is desirable for applications that require small amounts of oxygen in lab work or for medical use [8]. Current methods for producing these fuel cells include the epitaxial growth of films, tape casting, vapor deposition, powder processing, and numerous others methods [9-14]. Although these processes have proved successful, they either come at a high cost or do not allow for certain geometries or other physical properties. This work will investigate the development of solid oxide fuel cells through the sol-gel method and their resulting microstructures, electrolyte/electrode interfaces, mechanical and electrochemical properties, and performance specifically in oxygen generation.

2.0 LITERATURE REVIEW

2.1 Electrochemical Fuel Cells

The function of a fuel cell is to produce an electrical current that can be directed outside the cell to do work. Usually hydrogen gas (sometimes hydrocarbon-rich alcohol) is the fuel required to produce power in the system [15]. Several kinds of fuel cells exist and each operates with the direct conversion of a fuel and oxidant reaction into electrical energy. Direct methanol, proton exchange membrane, alkaline, and regenerative fuel cells are a few of the technologies studied today [16-18]. Some of these devices can also function to produce gases and concentrate oxygen. Once again, the focus of this work is on a form of solid oxide fuel cell (SOFC) to produce pure oxygen from air.

Typically, a fuel cell is constructed with two electrodes which will interface on either side of an electrolyte as in a basic battery structure. In a hydrogen fuel cell, the electrodes are porous to allow the fuel to contact the electrolyte/electrode interface. When hydrogen flows across the anode, a catalyst causes the gas to split into hydrogen protons and electrons (Eq. 1). The electrolyte only conducts the positively charged ions (H^+) that combine with oxygen at the cathode (Eq. 2). The electrons produced at the anode are directed through the external circuit to the load [19]. A diagram of a typical fuel cell structure can be seen in Figure 1 [1]. The chemical reactions that occur in the system depicted are listed below:

Anode side:
$$2H_2 \rightarrow 4H^+ + 4e^- \qquad \text{(Eq. 1)}$$
Cathode side:
$$O_2 + 4H^+ + 4e^- \rightarrow 2H_2O \qquad \text{(Eq. 2)}$$
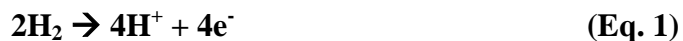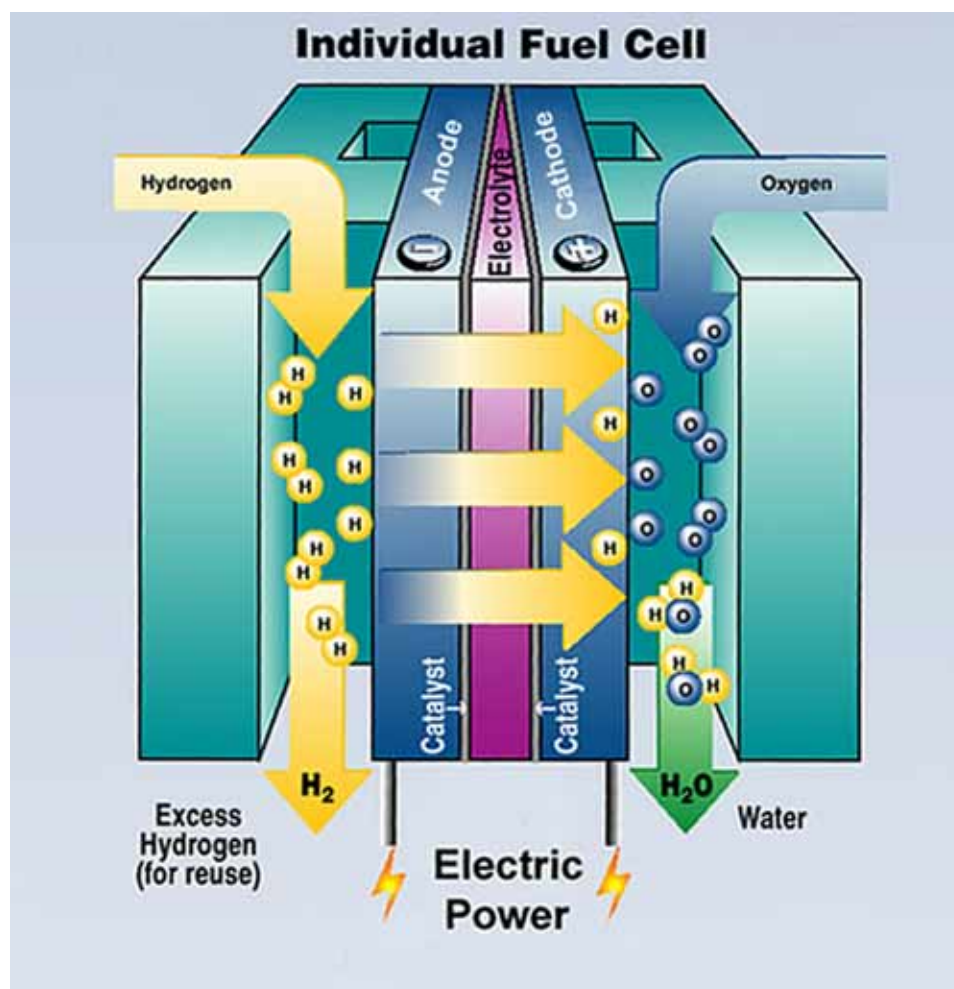
Figure 1: Schematic of a fuel cell that conducts H$^+$ [1]

<u>Net reaction:</u>

$$2H_2 + O_2 \rightarrow 2H_2O \qquad \qquad \textbf{(Eq. 3)}$$

The electrons that are produced on the anode side of the system are conducted through an electric circuit to power the load and are then used in the cathode during the reaction of hydrogen protons and oxygen gas. In this system both the protons and electrons travel from the anode side to the cathode.

2.2 Solid Oxide Fuel Cells

A solid oxide fuel cell (SOFC) can also use hydrogen to produce electricity but the electrolyte conducts negative oxygen ions via oxygen vacancies instead of hydrogen protons. In a solid oxide fuel cell, however, electrons flow from the anode to the cathode but the oxygen ions flow from the cathode to the anode. A schematic of this system is depicted in Figure 2 [20]. When an oxygen molecule contacts the cathode/electrolyte interface, it catalytically acquires four electrons from the cathode and splits into two oxygen ions (Eq. 4). The oxygen ions diffuse into the electrolyte material and migrate to the other side of the cell where they reach the anode. As the ions encounter the fuel at the anode/electrolyte interface there is another catalytic reaction, giving off water, carbon dioxide, heat, and, the most important product, electrons (Eq. 5). The electrons transport through the anode to the external circuit and back to the cathode, providing a source of useful electrical energy in an external circuit [21].
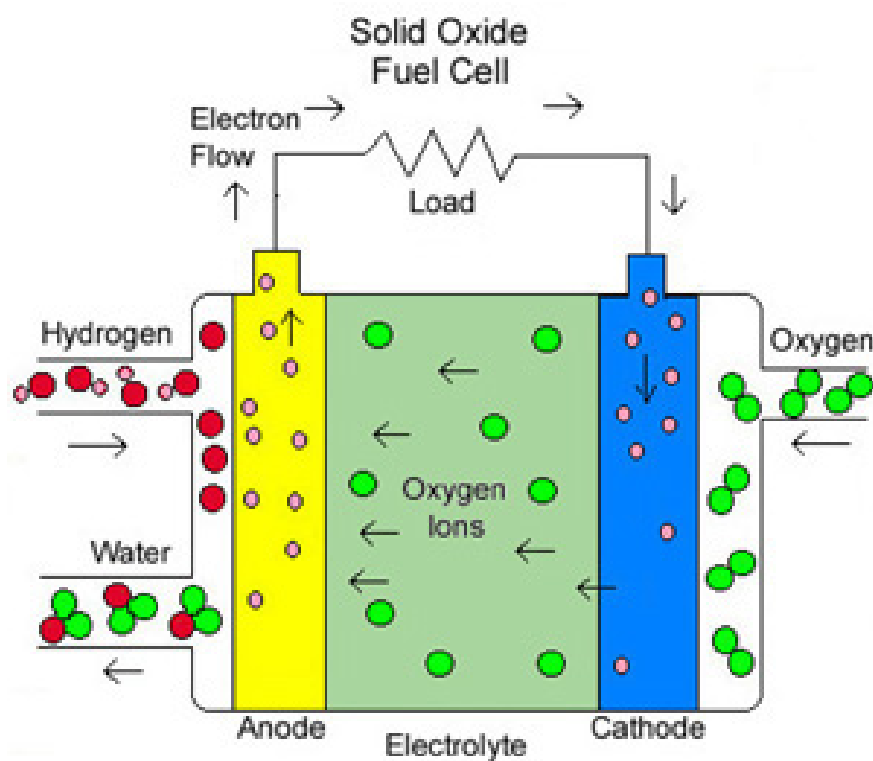
Figure 2: Schematic of a solid oxide fuel cell. Conducts O^{2-} [20]

Cathode Side:

$$O_2 + 4e^- \rightarrow 2O^{2-} \qquad\qquad \text{(Eq. 4)}$$

Anode Side:

$$2H_2 + 2O^{2-} \rightarrow 4e^- + 2H_2O \qquad\qquad \text{(Eq. 5)}$$
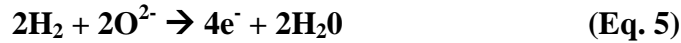
Fuel cells use hydrogen and oxygen to produce electricity. To generate oxygen, a SOFC can be used with air and applied electricity flowing from the anode when used as an electrical source. The system has the same setup and the anode and cathode are referred to as such, as if these were part of an electrical source in which the cathode is positive and the anode is negative. The electrical current does remain the same as does the directionality of the ions during power generation but now the product, oxygen, occurs at the anode and the function of the system is essentially reversed. Therefore, air must be fed to the cathode and with the application of the electric current oxygen ions are allowed to recombine into oxygen gas at the anode. The electrical load in this system is less important and only the electron flow is necessary [22].

Ambient air is a mixture of gases about one fifth of which is oxygen. The oxygen can be "extracted" from the other constituents including any moisture in the atmosphere. The air flows through a porous cathode and interacts with the electrolyte membrane, where the oxygen atoms are charged by the current. These ions are transported through the electrolyte, and molecules of oxygen are reformed on the other side. More specifically, as mentioned above in Eq. 4, when an oxygen molecule contacts the cathode/electrolyte interface, it is reduced, acquiring four electrons from the cathode and splitting into two oxygen ions. The ions diffuse into the electrolyte material and are

conducted to the other side of the cell to the anode. Essentially, without oxygen and hydrogen as fuel, the SOFC is inactive. In the absence of these gases and with the application of electric current the electrolyte will become ionically conductive.

As in any fuel cell, the electrolyte plays a key role. In this SOFC, the electrolyte must permit only oxygen ions to pass between the anode and cathode. If free electrons or other substances could travel through the electrolyte, they would influence the chemical reaction, and any gas penetration would negate the purpose of the system. The SOFC must be operated at an elevated temperature to increase ionic conductivity and allow oxygen atoms to enter the system at the cathode where the following electrochemical reactions cause an oxygen reduction [23-24].

Cathode side:

$$O_2 + 4e^- \rightarrow 2O^{2-} \qquad \text{(Eq. 6)}$$
$$H_2O + 2e^- \rightarrow H_2 + O^{2-} \qquad \text{(Eq. 7)}$$

The oxygen ions are transported through the crystal lattice of the electrolyte as electrons would through a conductor. Upon reaching the anode, there is oxygen evolution through a recombination process [23-24].

Anode Side:

$$O^{2-} \rightarrow O + 2e^- \qquad \text{(Eq. 8)}$$
$$O + O \rightarrow O_2 \qquad \text{(Eq. 9)}$$

Comparisons of an SOFC run for electricity and one for oxygen/hydrogen generation in which a water reactant was used can be seen in Figure 3 [24].
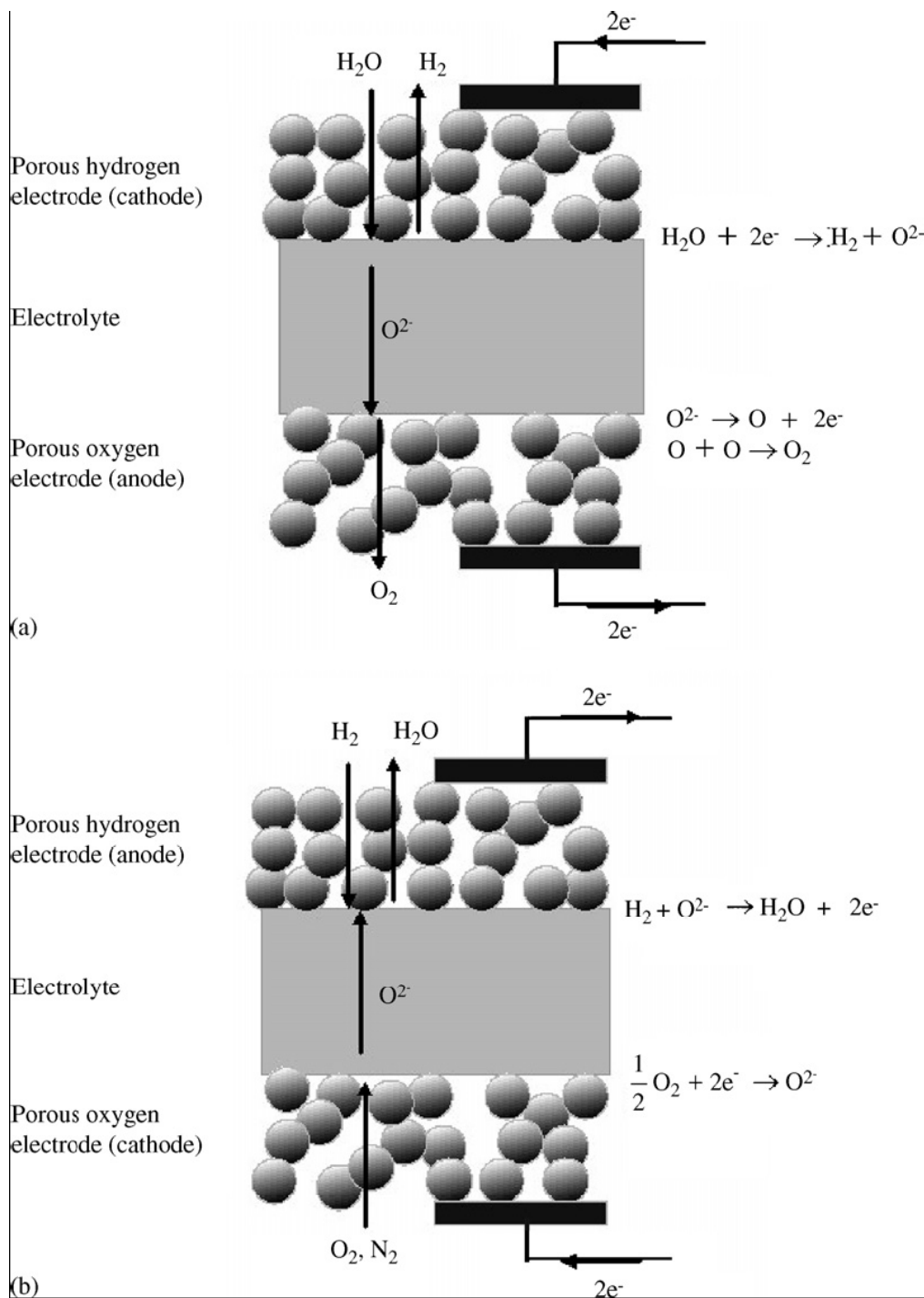
Figure 3: (a) SOFC used to produce H$_2$ and O$_2$ (b) SOFC used to produce water and electricity [24]

2.2.1 Ionic Transport

Understanding ionic conduction is important in determining the proper material systems necessary for certain applications. In general, ceramic materials are semi-conductors or electronic insulators. Many of these ceramics along with some of those that are electronic conductors tend to display extremely poor ionic conduction, if at all. A group of solid materials referred to as solid electrolytes, or sometimes fast ionic conductors, show a relatively high ionic conductivity [25]. Solid electrolytes can transport an array of different cations or anions depending upon the material system in use. However, the most widely researched electrolytes are for hydrogen (H^+) and oxygen (O^{2-}) transport [26].

The ionic conduction of any given material that is considered a fast ion conductor is dependent upon many factors. In a fuel cell, the electrolyte/electrode interface, microstructure, density, and temperature can all greatly affect the performance of the ion conductor [27]. Fuel cell systems can be optimized through material processing and operational procedures.

To understand why a material may be a good ionic conductor it is important to have a brief overview in basic conductivity. Frequently, more than one charge carrier can contribute to conduction in a material such as ions, electrons, and electron holes [26, 28]. Therefore, the total conduction in a system would be the sum of the individual conduction of each species. We will only consider electronic and ionic conduction (Eq. 10).

$$\sigma_{tot} = t_{(electron)}\sigma_{tot} + t_{(electron)}\sigma_{tot} \qquad\qquad \textbf{(Eq. 10)}$$

The fraction of the total conductivity contributed by each charge carrier is referenced as the transference number for that species (Eq. 11)

$$t_i = \sigma_i / \sigma_{tot} \qquad \qquad \textbf{(Eq. 11)}$$

The sum of transference numbers must sum to one whole unit. For a material to be strong ionic conductor $t_{(electron)}$ must be much lower than $t_{(ion)}$:

$$t_{(electron)} \ll t_{(ion)} \approx 1.0 \qquad \qquad \textbf{(Eq. 12)}$$

The mobility of an ion correlates with the ease by which defects can move within the lattice of the crystal structure [26]. For the ion to move through the lattice under the driving force of an electric field it must have sufficient thermal energy to pass through the intermediate positions between the lattice sites [28]. Kroger-Vink notation is associated with the motion of a species through a lattice and can be referenced later for yttrium stabilized zirconia (YSZ), the chosen electrolyte for this experimental oxygen generation system [26, 29].

Overall, it is the inherent nature of the crystal structure that will determine whether or not a material can conduct electrons, ions, or neither. But specifically, in ionic materials, the mobile carriers are the charged ionic defects. Instead of carrying electrons or electron holes as in electronic conduction, the concentration of vacancies and interstitials allow for ionic mobility. Charged point defects permit diffusive motions in the ion sublattices [26, 30].

2.2.2 Electrolyte

There have been a small group of ionic conductors that have proven useful as an electrolyte. Cerium oxide, bismuth oxide, and zirconia are the best known. Each has been tested using different molecular structures such as oxides and hydroxides, an array of dopants, and different processing techniques [31-43]. All of the testing has been directed towards optimizing the performance and durability of the material. As stated above, their ability to function as an ionic conductor is strongly dependant upon temperature. The operating temperatures for successful conduction range from 600-1000°C. Doping the materials has shown an increase in conductivity at lower temperatures allowing ion exchange in the range of 500-800°C which is reasonable for application purposes [44-46].

Since it is possible to increase the conductivity at lower temperatures, doping and processing must affect the crystal structure of these electrolytes as well. By obtaining the proper crystal phase, the thermal expansion and stability of the structure is modified to fit the needs of the electrode interface preventing cracking and membrane separation as well as ensuring a high ionic conductivity. The electrolyte must also be structurally and chemically stable, be gas tight, have a low electronic transference number, and it's properties must be relatively pO_2 independent [25, 47].

2.2.3 Anode

Developing a proper set of electrodes is important to the functionality of the system as well. An electronically conductive material is needed to form the electrodes where reduction and recombination occurs with similar thermal behavior to that of the

electrolyte. In solid oxide fuel cells used to generate power, several anodic materials have been explored. Referred to as the fuel electrode, the anode experiences highly reducing environments. Along with being electronically conductive, the material used as an anode must have a thermal expansion coefficient close to that of the electrolyte, good stability, and a high catalytic activity to oxidize the fuel, namely CO and H_2 [48]. Ni-YSZ cermets of varying Ni content meet most of these requirements and are the most commonly used anodes in fuel cells today with YSZ electrolytes [48, 49]. The performance of a Ni/YSZ cermet anode depends critically on the microstructure of the porous YSZ framework and the distribution of the nickel. This dependence and the requirement that the structure remain stable over long periods of time at the operating temperature puts focus on the processing techniques used in the development of the anode. Conventional Ni/YSZ anodes may either support the electrolyte or be supported by the electrolyte. Nickel and rare-earth doped ceria has begun to gain popularity as an anode material as well [31, 48].

2.2.4 Cathode

The cathode material is also sometimes referenced by its environment as the air electrode. This compound must also possess many of the same properties as the anode material such as electronic conductivity, thermal stability, good thermal cycling sustainability, and a similar coefficient of expansion to the electrode. Doped manganese, cobalt, chromium, carbon, and iron oxides have been researched at length due to their stability and conductivity [48, 50-53].

The electrocatalytic properties of Sr-doped lanthanum manganese oxide (LSM) have proven to be unfavorable at lower temperatures compared to that of other oxides. Although all of the oxides mentioned have the same perovskite structure, LSM has significantly slower kinetics for oxygen transfer at the electrolyte interface [48, 54]. However, the reactivity of the compounds with faster kinetics (CoO_3 and FeO_3) at low temperatures is too high causing thermal expansion issues and membrane separation [48]. It has also been observed at temperatures exceeding $1200^{o}C$ that there is a high reactivity between YSZ and LSM. This causes a formation of $La_2Zr_2O_7$ and $SrZrO_3$, both of which have very low conductivity and hinder the overall performance of the fuel cell. The formation of these compounds also leads to grain boundary resistivity and a reduction in the triple phase boundary, which will be discussed in the next section [48, 55-57]. Despite these drawbacks, LSM has become one of the more popular cathode materials used in solid oxide fuel cells due to the wide use of midrange temperatures ($700-900^{o}C$) for application and similar behavioral characteristics to those of YSZ.

2.3 Triple Phase Boundary

The total oxygen reduction reaction requires the presence of gaseous oxygen and good electronic conductivity in the electrode material as well as the possibility for created oxide ions to be transported away from the reaction site into the bulk of the electrolyte. The triple phase boundary (TPB) between electrode, electrolyte and gas phase in the bulk of the electrode can meet the requirements. Therefore, the resistance of the electrode is decreased by extending the length of TPB, which results in a lower impedance of oxygen

reduction, and increases the oxygen diffusion in the electrolyte [52]. Optimal operating temperatures must be considered due to the TPB as well. During sintering, new phases may form due to electrode/electrolyte reactions. Any new phases that may be present will result along the TPB. Therefore, dependent upon the material system, the higher the operating temperature the higher the probability will be that the interface will degrade and reduce current density (A/cm^2) of the SOFC [58].

The power output of a fuel cell that utilizes electronically conducting electrodes such as LSM is believed to be dependent upon the TPB width. Investigations have shown impedance spectra relating to a constriction resistance, where all of the current had to pass through a narrow triple phase boundary. This constriction accounted for most of the resistance of thick electrolyte samples but was relatively small for thin film electrolytes. Also, mixed conductor membranes with a finer microstructure enlarged the triple phase boundary area produced relatively high hydrogen production rates in SOFC testing [59-60]. Improper electrolyte/electrode interfaces increase the activation energy needed for the reduction of oxygen. Oxygen vacancies at the TPB are found to be responsible for the lower energy barrier. When only reacting with the electrode oxygen vacancies are not formed and the gas cannot be readily dissociated [61]. Figure 4 is a cross-sectional representation of a triple phase boundary interface.

For solid oxide fuel cells, composite electrodes, electrodes doped with the electrolyte material, have shown improved cell performance due to an increased density of reaction sites. These reaction sites are due to the increased surface area of the triple phase boundary [61-62]. Deng et al. [62] studied the relationship of grain and pore size and the area of the TPB. Results have shown that a finer grain size increases the TPB
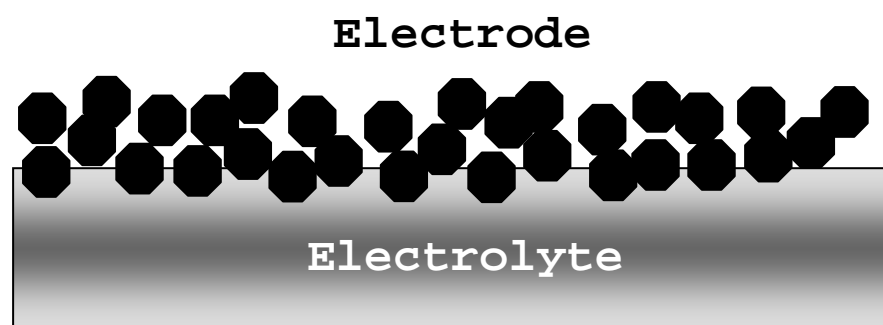
Electrode

Figure 4: Triple Phase Boundary (2D)

length exponentially, while the pore sizes and porosity can be optimized to promote a larger area of the triple phase boundary. It was reported that composite electrodes with 20-30% porosity and a 2-5μm average pore size yielded higher TBP surface areas. This result was consistent for all grain sizes although a smaller average grain size is preferable [62]. The resultant data from this study can be seen in Figure 5 [62].

2.4 Material Systems

The more favored electrolyte materials will be discussed in the following sections by compound. Table 1 and Figure 6 show a few comparison studies done on ZrO_2, CeO_2, and Bi_2O_3 based ionic materials [63, 64].

2.4.1 Bismuth Oxide

Bismuth oxide systems exhibit high oxide ion conductivity and have been proposed as good electrolyte materials for applications such as solid oxide fuel cells and oxygen sensors. However, due to their instability under conditions of low oxygen partial pressures there has been difficulty in developing these materials as alternative electrolyte materials compared to the better understood cubic stabilized zirconia electrolyte. Bismuth oxide and doped bismuth oxide systems exhibit a complex array of structures and properties depending upon the dopant concentration, temperature and atmosphere [65]. Aluminum doped bismuth vanadate is one of the most stable bismuth compounds but has a significantly lower conductivity than zirconia materials [64]. One study reported a relatively high conductivity using bismuth oxide as a dopant in scandium

Figure 5(a)
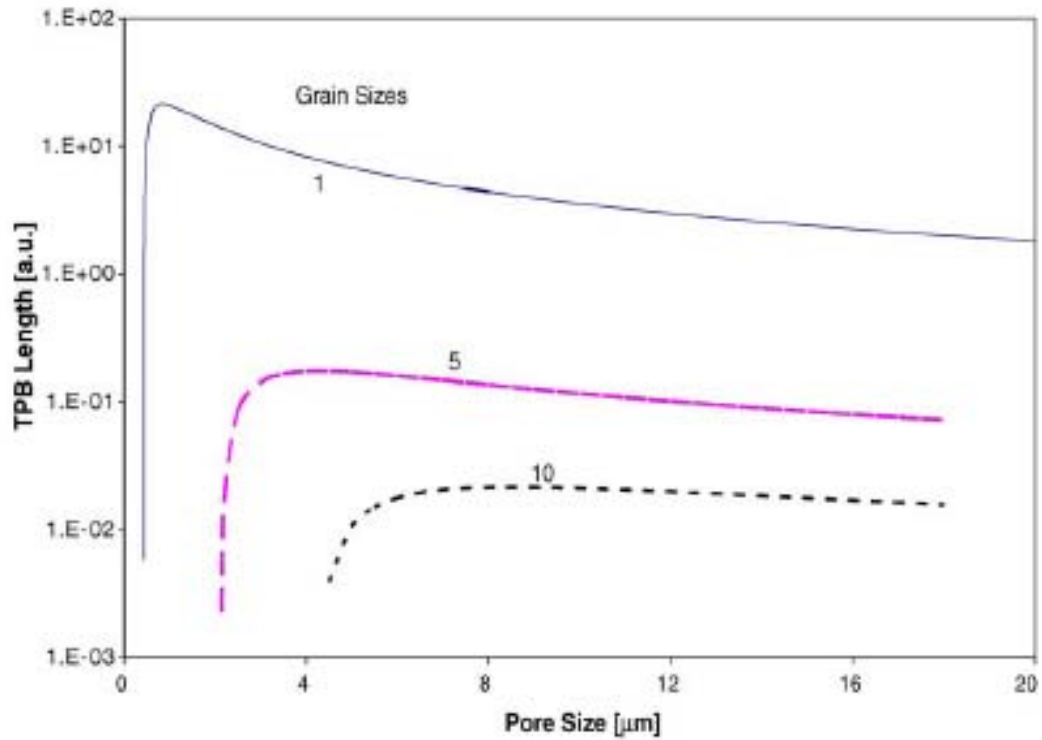
Figure 5(b)
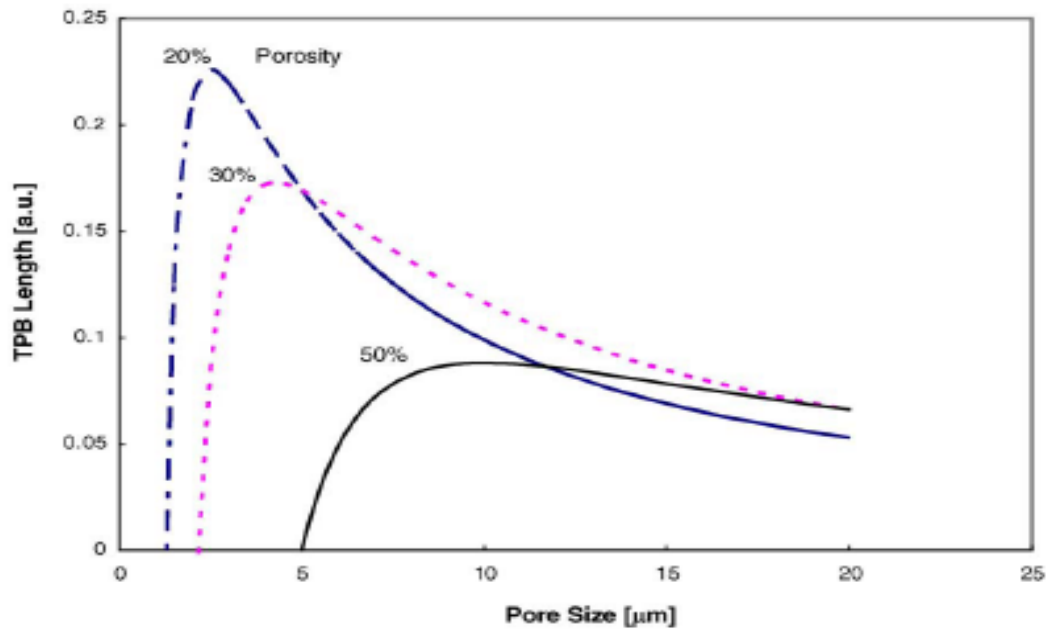
Figure 5: (a) Relationship between the TPB length and pore size. The porosity is 30% (b) Relationship between the TPB length and pore size at different porosities of 0.2, 0.3, and 0.5 and solid grain size of 5μm [62]

Table 1: Comparison of electrolyte materials for SOFC [63].

Electrolyte	Operating Temperature (^{o}C)	Ionic Conductivity σ (S/cm)	Other Features
ZnO-doped YSZ	800	0.0289	Degradation of the cell components and interfacial reaction
GdAlO$_3$, Ca-doped GdAlO$_3$	1000	0.0132, 0.057	New material with little data on its oxygen ion conductivity
ZrO$_2$ co-doped with ScO$_3$ and CeO$_2$	800	0.120	High sintering temperature
BIMEVOX	400	0.02	Good stability over time, high density
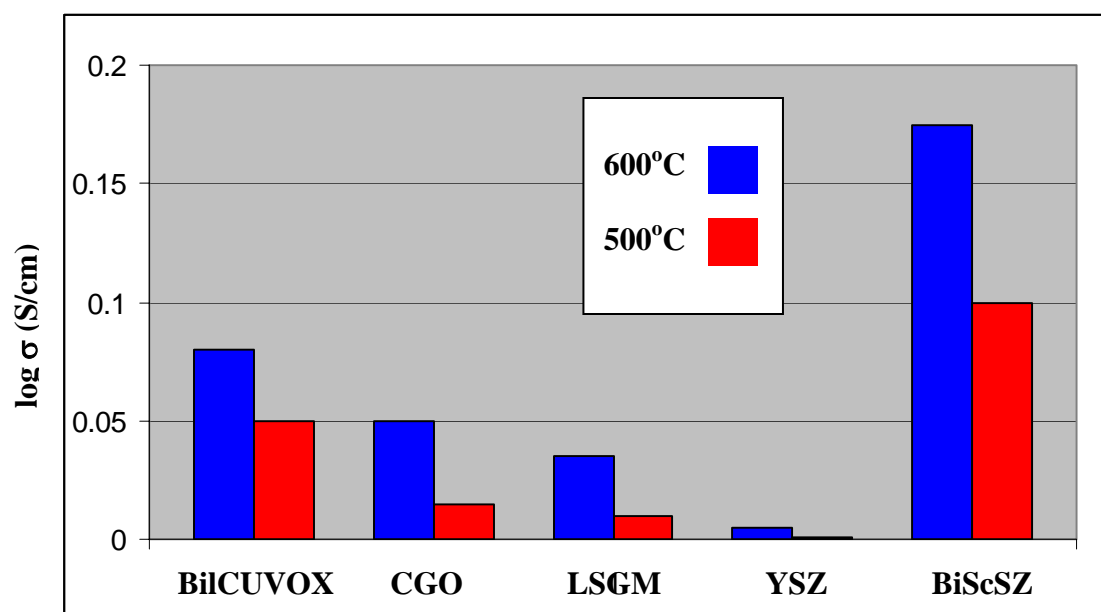
Figure 6: Total conductivity at 600 and 500°C of 2 mol% Bi2O3 doped ScSZ in air sintered at 1500°C in comparison to other most promising oxide ion conductors [64]

stabilized zirconia. This was reported as one of the highest conductivities found using bismuth oxide and was comparable to that of zirconia materials [64].

2.4.2 Cerium Oxide

Acceptor doped CeO_2, such as Gd-CeO_2, has been considered as potential oxide ion electrolytes for the development of solid oxide fuel cells as well as other applications, including oxygen pumps and sensors for various gases due to their high ionic conduction [66-68]. Successful conduction occurs around $600^{o}C$. Such a low-temperature has several advantages over the high temperature electrolyte such as flexibility in the choice of the electrodes, bi-polar materials, seals, as well as long-term stability and costs [69]. The main concern with the CeO_2 based electrolytes are related to large grain-boundary (especially at low temperatures) impedance, which results in a huge total resistance of the system, and hence shows poor current density. Also, unlike zirconia based electrolytes, CeO_2 based compounds exhibit poor mechanical stability. Accordingly, current research work has been directed to the development of solid electrolytes with optimized microstructure to lower the total resistance by various wet-chemical methods for applications in advanced SOFCs and other solid-state ionic devices [68]. Other research has found strong ionic conductivity in CeO_2-ZrO_2-$YO_{1.5}$ which forms a stable fluorite structure. But there are thermal expansion issues that need to be addressed [69]. It can also be seen in Table 1 that a zirconia electrolyte using ceria and scandium oxide yielded quite a high conductivity. In fact, it is one of the highest conductivities reported for an aliovalent doped ceramic under $1000^{o}C$ [63]. But because of scandium's scarcity and difficulties associated with its extraction, it is very expensive [70].

Investigations using a ceria based composite for an electrode reported it to be a promising cathode and also anode for the electrochemical oxygen generator. This electrode composite was used in conjunction with a samaria doped ceria electrolyte [71].

2.4.3 Zirconium Oxide

Zirconium oxide (Zirconia) has been researched extensively for many purposes. It possesses many desirable properties such as high hardness and mechanical strength. It is also fairly inert, has a low specific heat, and is a good thermal insulator [72, 73]. Zirconia exhibits three crystal phases. At one atmosphere of pressure, zirconia has a monoclinic structure up to $1170^{o}C$. There is a stable tetragonal phase upwards of $1170^{o}C$ until $2370^{o}C$ is reached when the crystal structure transforms into a stable cubic structure [74]. Due to these phase changes, zirconia has been a useful material in transformation toughened ceramics which exhibits a large volume change resulting in stresses in the structure [75, 76]. When cooling zirconia from the cubic phase, metastable tetragonal and cubic phases remain even as most of the structure reverts to its original monoclinic crystal phase. Many researchers have tried to analyze and explain the remaining phases at low temperatures relating it to particle size, lattice strain, and impurities [77-86].

When developing zirconia as an electrolyte, metastable phases in the temperature range of the monoclinic phase are unimportant. The tetragonal and cubic phases have displayed considerable ionic conductivity while the monoclinic phase has an insufficient structure for ion mobility [87]. Stabilizing these crystal phases at lower temperatures is an important focus for developing zirconia as an effective electrolyte. The ability to

stabilize the cubic phase where the ionic conductivity is facilitated is technologically important [88, 89].

2.4.4 Yttrium Stabilized Zirconia

Zirconia can be used for the electrolyte due to its electrical insulation and ability to conduct oxygen ions in the proper crystal phases, namely cubic or tetragonal. As stated above, ZrO_2 experiences destructive lattice changes, causing cracking, when it is thermally cycled and the aforementioned phases are not stable. The addition of some oxides, such as yttria, decreases these changes. The fully stabilized zirconia (F-YSZ) has no lattice changes from room temperature up to $2500^{o}C$ [75, 90]. Its crystalline structure is a cubic solid solution. Moreover, pure zirconia is a relatively low ionic conductor. However, due to the addition of aliovalent oxides, oxygen ion vacancies are created through which ionic conduction can occur. Y_2O_3 also creates ion vacancies making it easier for O^{2-} to move from one site to the next [91]. Hence, the dopant increases the ionic conductivity of the zirconia. This is also a result of the fluorite structure that is developed. The fluorite structure has shown the most promising results in ionic conductivity. The structure can be seen in relation to the basic cubic structure in Figure 7 [92, 93]. Within YSZ, yttrium (3+) substitutes for zirconium (4+), and, to maintain charge neutrality, some oxygen lattice site vacancies are formed. At high temperature, thermally activated oxygen ion transport becomes easier using these vacancy sites [94, 95].

Figure 7(a)
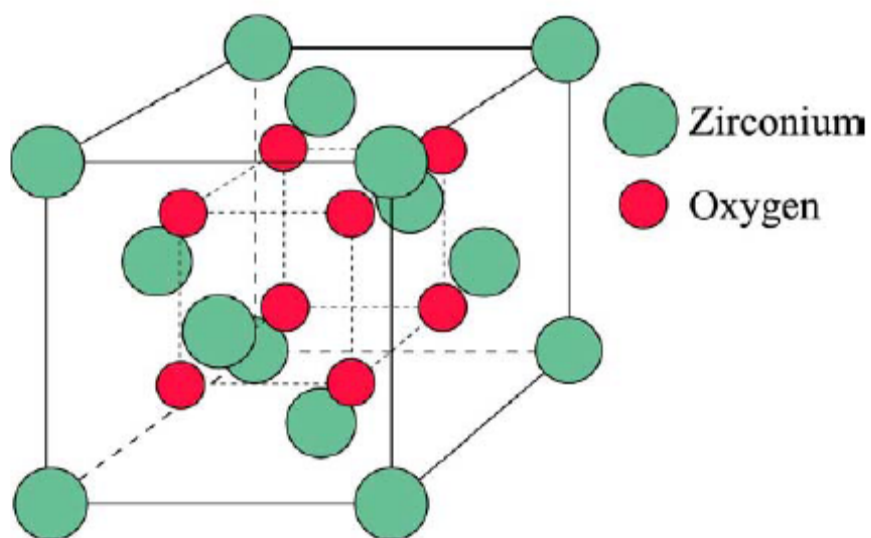
Figure 7(b)
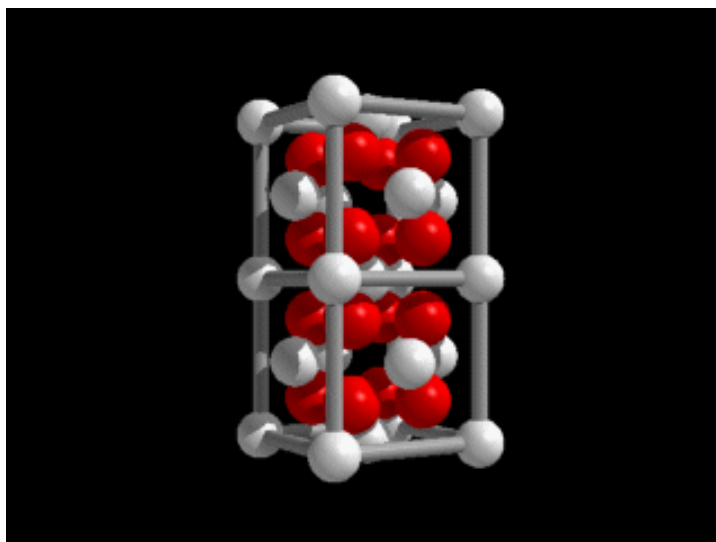
Figure 7: (a) The fluorite structure is a simple cubic structure [92]
(b) Two fluorite unit cells [93]

Overall, doping the electrolyte with yttria decreases the lattice changes, stabilizes the proper phase, and increases ionic conductivity. Although even with the addition of Y_2O_3 the ionic conductivity is too low at room temperature. The ceramic electrolyte has to work at high temperatures, typically 800^oC or greater [96-98]. Efforts to reduce the operating temperature for fuel cells have been strong during the past few years. Research has shown that grain boundaries and impurities are two of the strongest factors limiting ionic conductivity at low temperatures [44, 91].

Many studies have been done on YSZ and variations of the compound. Processing and application techniques have been tested to determine a cost-effective way to develop a zirconia membrane with a higher ionic conductivity. YSZ electrolyte compositions have been thoroughly investigated based on the mole and weight percent of the dopant. Powder pressing techniques of commercially available YSZ powders at 11 and 15 weight percent have been extensively researched by Brosha et al. [99] yielding very high ionic conductivity at temperatures as low as 550^oC with the proper sintering cycles and electrode compositions [99-101]. Precipitated zirconia solutions varying in mole percent including 3%, 7.5-11%, and 13% yttria have been analyzed by XRD and Raman spectroscopy to determine the stable crystal structure in sol-gel processing. Many of the sol-gel derived YSZ compounds resulted in a mixture of tetragonal and cubic crystal phases with a heavy emphasis on the former [102-104].

2.4.5 Electrodes

As previously mentioned, the mixed oxide, lanthanum strontium manganate or LSM ($La_{1-x}Sr_xMnO_3$) is a popular cathode material. LSM has reasonable electrical

conductivity and a high catalytic activity for oxidation of O^{2-}. It also has a thermal expansion coefficient very close to that of ZrO_2 (the basis of the electrolyte). The microstructure of this LSM is a compromise between a porous layer and a dense one. This allows the gas to diffuse through the electrode layer and a density high enough to provide good conductivity through the material [105, 106].

Research has shown that in oxygen generation, anodic materials like the Ni-YSZ cermet compound are unnecessary to the electrochemical reactions involved. Sr-doped $LaMnO_3$ has shown reversible oxidation-reduction behavior [107].   For power generation, the reduction takes place at the LSM cathode and recombination is at the anode involving H_2 gas and O^{2-}. In oxygen generation, reduction takes place at the LSM cathode but with no abrasive fuel at the anode side. As the oxygen ion (O^{2-}) reaches the anode it loses two electrons and needs to combine as seen in Eq. 9: $O + O \rightarrow O_2$. Therefore, a SOFC using an YSZ electrolyte and LSM for both electrodes would be sufficient for oxygen generation and, in fact, has been used for oxygen production. This has been accomplished with many production techniques including spin-coating and slip casting [108-110].

2.5 Oxygen Generation

The production of oxygen has been reported using Pt, CeO_2, LSM, YSZ, and LSM/YSZ composite materials [109-112]. The preferred YSZ electrolyte for both power and oxygen generation is 8 mole % Y_2O_3. This composition is reported to have a high activation energy for electrical conductivity permitting non-conductive electrolyte films

as thin as 5μm [113-116]. Oxygen generators have been formed using one processing method for all components or a combination. Molecular beam epitaxy and vapor deposition are proven methods that come at a relatively high cost. Powder compaction, slip casting, tape casting, and YSZ precipitation are some of the less expensive methods and can allow for a number of geometries.

Planar and tubular designs are the most common for SOFCs. To collect oxygen, a tubular design would be preferred to avoid unnecessary additions in order to contain the gas. An example of the different cell designs can be seen in Figure 7 [21, 117]. The cell in Figure 8(a) was designed for power generation. The electrodes were extruded and the YSZ electrolyte was applied using electrochemical vapor deposition. Due to low power densities tubular SOFCs are usually suitable only for stationary power generation and not very attractive for transportation applications.

Figure 8(b) represents a planar SOFC construction. The cell components are configured as thin, flat plates. The interconnection is ribbed on both sides forming gas flow channels and serves as a gas separator contacting the anode and the cathode of separate fuel cells when stacked. When stacked, the total power generated by the fuel cells operating together can be used for more demanding applications such as transportation. The cells are fabricated by low-cost conventional ceramic processing techniques such as tape casting, slurry sintering, screen printing, or by plasma spraying [117].

Figure 8(a)
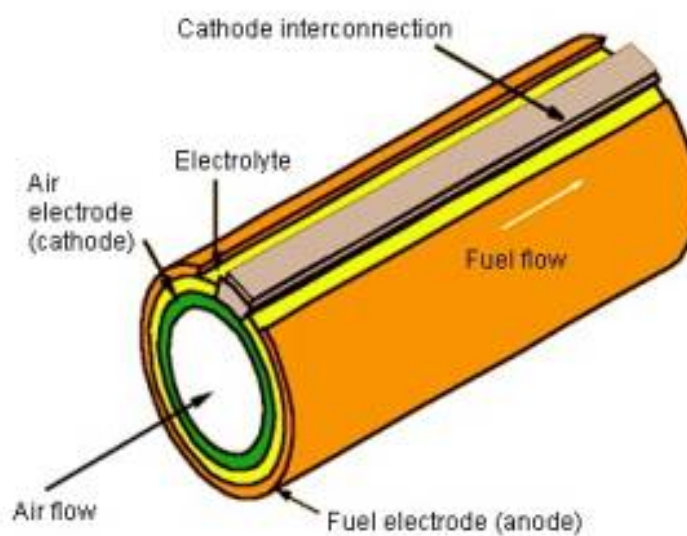
Figure 8(b)
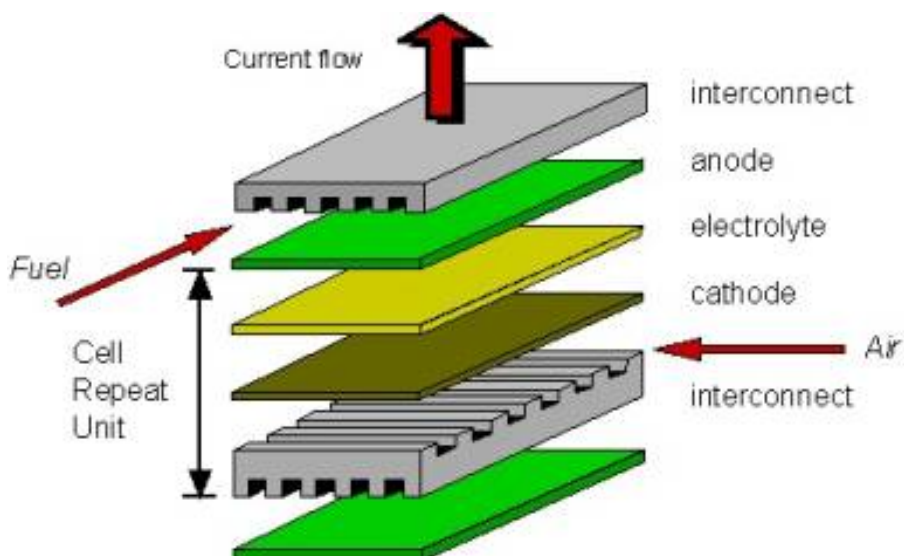
Figure 8: (a) Configuration for a tubular design SOFC (b) Configuration for a planar design SOFC [21, 117]

While these designs may be suitable for oxygen and power generation, a design that can facilitate collection of gases due to its shape would be preferred for oxygen evolution. Figure 9 is the proposed oxygen generation system for this project. The unit is cylindrical and closed on one end while the collected oxygen can be extracted on the other side. All of the films in the system, electrodes and electrolyte, are developed through sol-gel processes allowing for shape conformity. The actual shape of the solid oxide fuel cell is given by the substrate. It is a commercially available porous alumina tube (Norton/Saint Gobain), to which the films can easily be applied. The material provides the proper support and shape of the fuel cell and is a high temperature ceramic that can withstand thermal cycling beyond the temperatures necessary. The design of the substrate reduces the need to modify the cell after the films have been applied.

2.6 Sol-Gel Processing

Solid oxide fuel cell systems are based on thick film, thin film, or bulk technology. This is achieved through any number of processes including epitaxial growth, tape casting, lithography, and many other deposition methods. In this system, the entire fuel cell is developed through sol-gel processes with the exception of the substrate. The method is advantageous in many ways related to this project as well. Sol-gel allows for:

-low temperature development of materials

-ease of chemical doping

-inexpensive processing
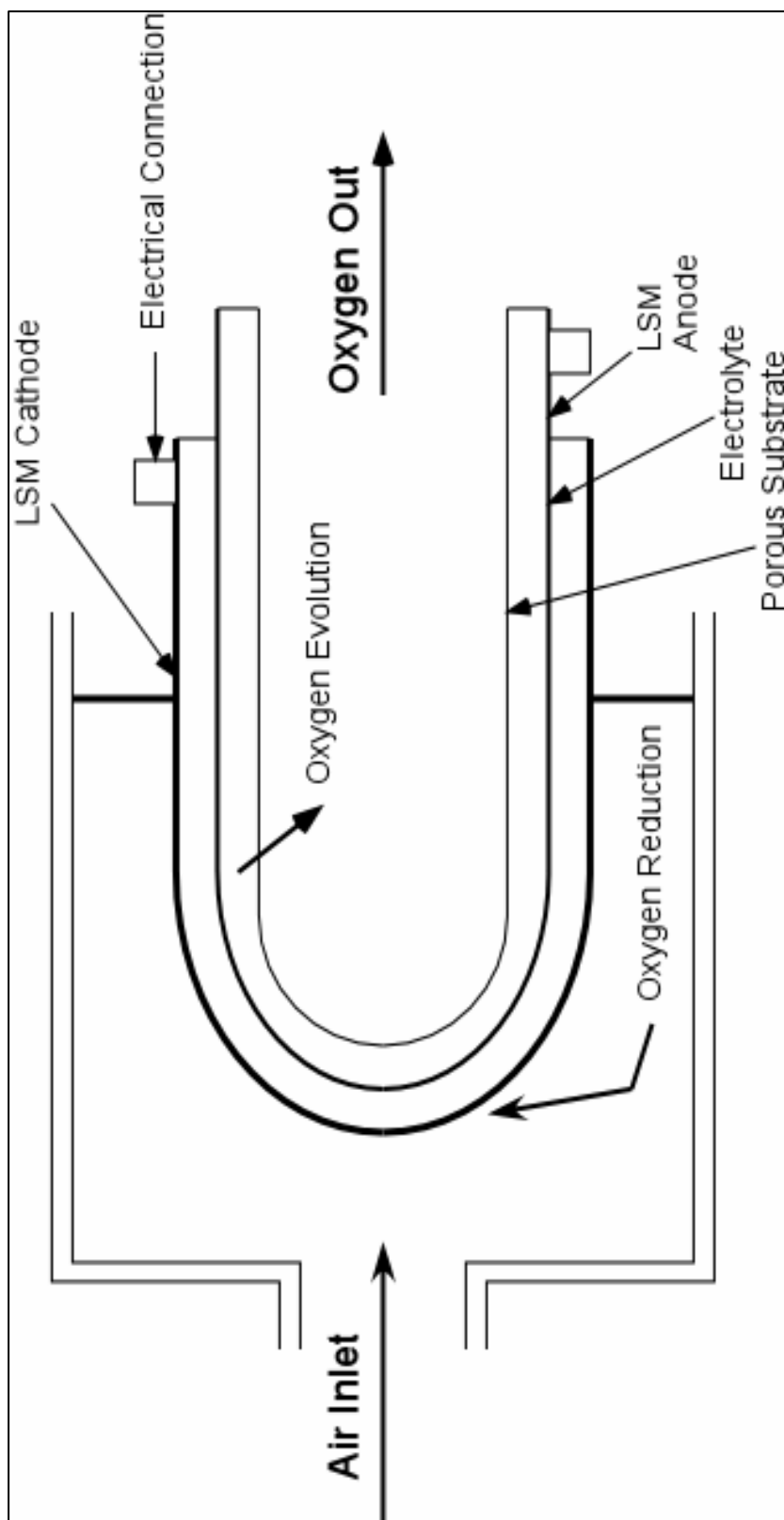
Figure 9: Proposed SOFC design

-film development for different shapes

-large area applications

-fast deposition

-good layer thickness control through viscosity

The sol-gel process is a chemical synthesis of the oxides from the soluble precursors involving the hydrolysis and condensation of metal alkoxides. Organic and inorganic salts of the metal species are mixed to produce the overall stoichiometry for the required material. The reactions are listed (Eq. 13 and Eq. 14) [118]. They represent reactions in the precursor for the solution. Hydrolysis occurs when the metal cations (M) are solvated by water molecules. Condensation occurs when one hydroxyl (OH) is present in the coordination sphere of M [119]. The salts are dissolved in a liquid medium, preferably water, so that thin layers can be applied directly to the supporting materials. Multiple layers can also be used to build up desired thickness [120, 121]. The liquids increase in viscosity upon application to form a solid gel. The gel requires heat treatment to develop the proper crystal phases.

Hydrolysis:

$$-M\text{-}OR + H2O \rightarrow -M\text{-}OH + ROH \qquad \textbf{(Eq. 13)}$$

Condensation:

$$-M\text{-}OH + RO\text{-}M\text{-} \rightarrow -M\text{-}O\text{-}M\text{-} + ROH \qquad \textbf{(Eq. 14)}$$

The solvents used in the solution are needed for dopant distribution, reaction, and mixing in the sol. This liquid can be applied easily as a film and the solvent removed

during sintering, which leads to the grain structure of deposited materials. This process is inexpensive and results in a thin membrane and electrodes that improve its electrical performance and alleviate many of the material design problems, including sealants and membrane sustainability.

The anodic layer, oxygen conductor layer, and cathodic layer can be applied by placing successive coatings on top of a porous ceramic support tube. The sol-gel process can be performed either by brush, dip, or spin-coating, depending on the nature of the substrate and thickness and quality of the film required.

3.0 METHOD OF ATTACK

The objectives of this research were to (1) build a solid oxide fuel cell using sol-gel processing, (2) characterize the precursor solutions for LSM and YSZ, (3) examine the microstructure of the sol-gel layers, (4) demonstrate the presence of a triple phase boundary, (5) find a process that leads to a functioning solid oxide electrolyte membrane, (6) evaluate the SOFC performance.

There have been numerous investigations on the use of sol-gel processing in fuel cell development including sol-gel electrodes, doped electrolytes, and connective layers to prevent membrane separation [122-128]. Prior research done has included a sol-gel process in the development or improvement of a fuel cell. However, there is no investigation of an entirely sol-gel derived solid oxide fuel cell. Therefore, this study was carried out to find conditions for sol-gel derived electrodes and electrolytes that resulted in the proper structure. The entire development and performance of a solid oxide fuel cell for oxygen production under strictly sol-gel processing was investigated.

Sol-gel derived membranes for both the electrodes and the electrolyte were formed using solution deposition methods. Each membrane was formed by repetitive layering and sintering of the sol-gel material. The approximate thickness of each membrane was determined by the weight gain of the entire sample. Complete samples were electrochemically tested for fuel cell performance and then microstructurally evaluated. These samples were characterized using a gas pressurization technique. The solutions used for layering were characterized by XRD, spectroscopy, and TGA.

4.0 EXPERIMENTAL PROCEDURES

4.1 Substrate Preparation

Pressed alumina thimbles were ordered from Fisher Scientific (catalog #09960E, 45x127mm thimble-AL889). These thimbles are a porous ceramic manufactured by Norton/Saint Gobain. Geometrically, the commercial substrates are a cylindrical structure with one closed end and the opposite side open. The original length of the cylinder is approximately 11cm with a hemispherical top extending a little more than 2cm further, and 3cm is cut off of the open end. The substrate is marked about 1cm from the open end around the entire substrate indicating an area used for handling, which leaves $94.2cm^2$ for the active surface of the sample. The substrate is heated to 300^oC for 15 minutes to remove any moisture, and then the weight is recorded.

4.2 Electrical Distribution

4.2.1 Platinum Layer for Current Collector

The substrate surface is covered with a platinum paste to increase the electronic conductivity of the current collector. Heraeus Pt conductor paste was obtained from the Heraeus Corporation (product #LP11-4493). A thinner (Heraeus Corporation, product #RV-372) is added to the paste to obtain a consistency similar to water. Approximately 3 drops of thinner are required for 1g of paste. A total of 2g of thinned Pt paste is applied to the entire substrate using a wide brush, excluding the part of the tube used for

handling. After this layer is applied, the sample is heated to $150^{\circ}C$ for 15 minutes. Any loose Pt is lightly brushed away to smooth the surface. This process is repeated until the desired weight gain is observed. Usually 3-4 Pt layers results in approximately $0.03g/cm^2$.

4.3 Solution Preparations

Most reagents were purchased from different sources. The vendors, product numbers, and details can be found in the appendix.

4.3.1 Lanthanum Strontium Manganate (LSM) Solution

The lanthanum strontium manganate solution is prepared at room temperature. The main constituents consist of 1 part strontium nitrate solution, 2 parts lanthanum chloride solution, and 3 parts manganese acetate solution by volume. In this work, 110ml of electrode solution was prepared twice for each sample, one batch prepared for the anode and one for the cathode.

The strontium nitrate solution is prepared by dissolving 3.2570g of strontium nitrate ($Sr(NO_3)_2$) in 16.7ml of distilled water. The lanthanum chloride solution requires 12.3781g of lanthanum chloride ($LaCl_3*7H_2O$) to be completely dissolved in 50ml of distilled water. The lanthanum solution is then added to the strontium solution. The next step involves the addition of the manganese acetate solution to the strontium/lanthanum mixture. This solution is prepared by dissolving 8.6470g of manganese acetate ($Mn(CH_3OO)_2*4H_2O$) in 33.3ml of distilled water. Once the three solutions have been

allowed to mix, 10g of citric acid ($C_6H_8O_7$) is added followed by 10ml of ethylene glycol ($C_2H_6O_2$). The citric acid and ethylene glycol are added as complexing agents. Finally, 10 drops of 0.1M NH_4OH is added and the solution is allowed to stir for 30 minutes. The flowchart is depicted in Figure 10.

4.3.2 Yttria-stablilized Zirconia (YSZ) Solution

The YSZ solution is prepared in batches of 200ml. The electrolyte sol is prepared on a hotplate at approximately 80^oC while stirring. First, 60ml of distilled water and 60ml of ethanol are mixed and allowed to reach temperature on the hotplate. The zirconia precursor is a commercially available zirconium oxychloride solution (ZOC), and 20ml of this solution is added to the mixture. Yttria is added as a powder, specifically from 1.24g of yttrium nitrate ($Y(NO_3)_3*6H_2O$). When the solution is at temperature, 60ml of 1.5M NH_4OH is added slowly in 1ml amounts using a pipette. White agglomerates form quickly when adding the base and must be allowed to dissolve before more is added to prevent gelation. Once the base is added the solution is stirred at 80^oC for 1 hour and then allowed to cool. Figure 11 shows the flowchart for the electrolyte sol.

Many layers are required to create the electrolyte membrane. The solution usually must be prepared several times during the processing of a sample. The electrolyte sol was not used after the solution had aged two weeks.
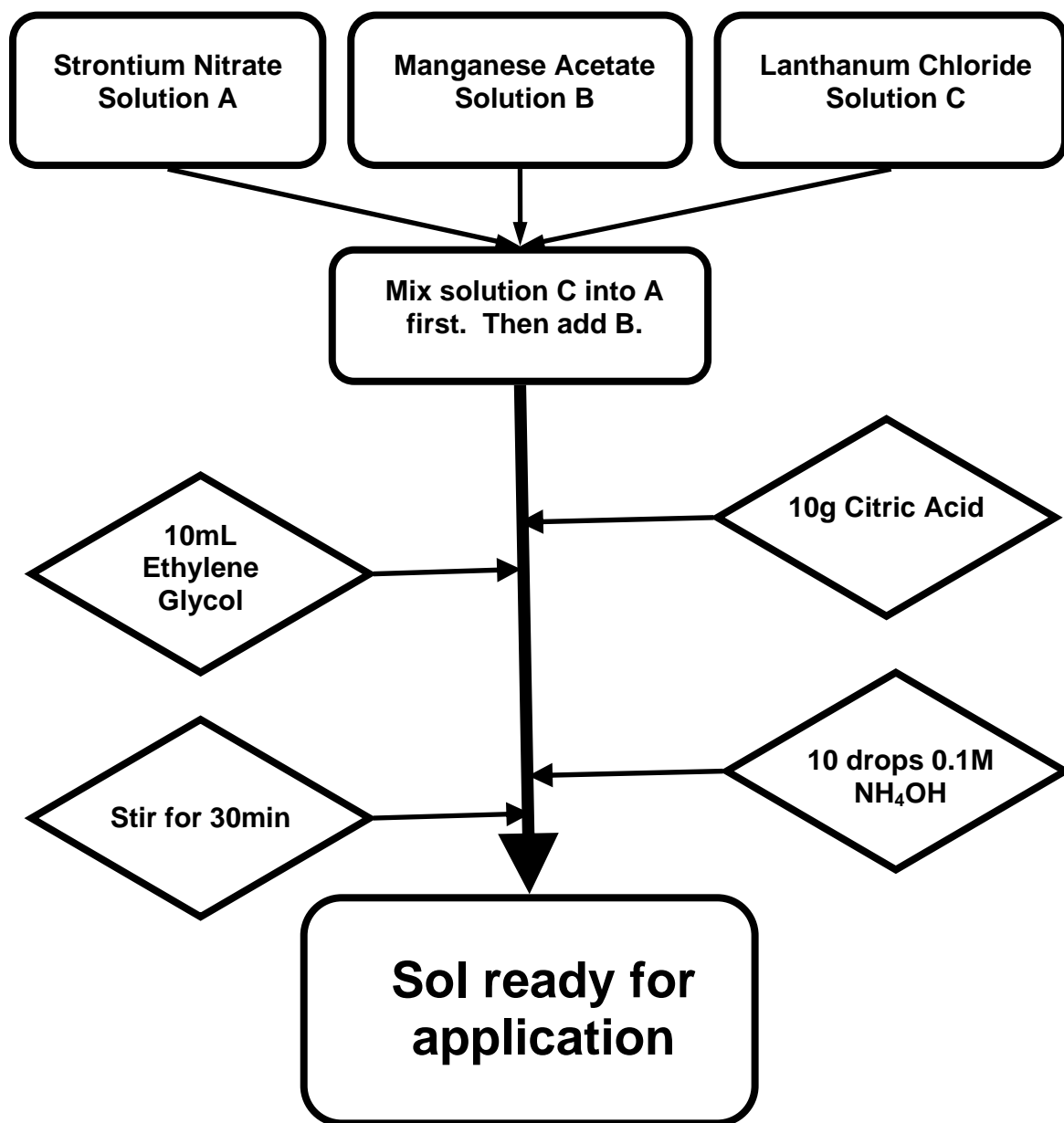
Figure 10: Procedural flowchart for LSM electrode sol

60 mL of distilled H_20 at $80^{o}C$

20 mL ZOC

60 mL Ethanol

1.24g $Y(NO_3)_2$

60 mL 1.5M NH_4OH

Heat and stir 30mins

Sol ready for application
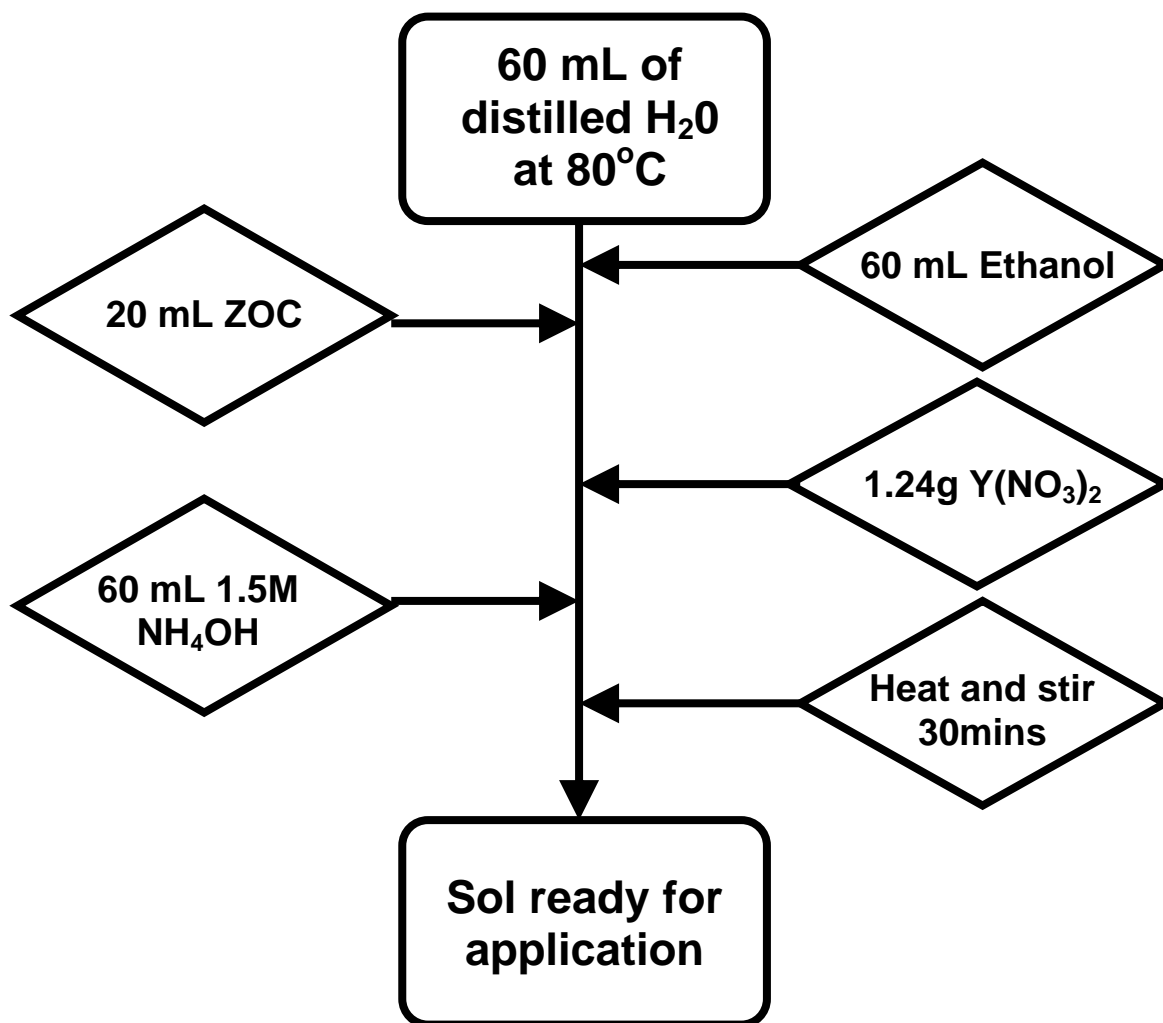
Figure 11: Procedural flowchart for electrolyte sol

4.4 Layer Assembly

Similar processes are used to form the fuel cell electrode and electrolyte membranes. They only differ in the number of layers required for their thickness and their overall heat treatment cycles. All samples were coated layer by layer to develop each membrane. After each layer is applied, the sample is sintered to the proper temperature.

The geometry of the sample prohibits application techniques such as spin coating and spray coating. Two methods of applying the electrolyte solution were tested. Some samples were dip coated and some were entirely brush coated. Previous studies have shown that dense YSZ films can be deposited via dip coating on porous anodes for SOFCs [129]. A mechanical dipping arm was used at low speed for consistent even coating of each layer on the sample. One dip would coat the sample enough for one layer. Brush coating means the solution is applied with a flat artist's brush. Three coatings are required to develop one layer when brush coating.

4.4.1 Anode Application

The anodic membrane is applied first to the substrate. A small amount of the Pt layer is left exposed around the circumference of the sample near the handling area to allow for electrical connections in later use. Twenty layers of LSM are required to reach the desired weight of 1g. Each layer is fired to 1100°C with no hold, except that the 5th, 10th, and 15th layers are fired to 1100°C and held for 30 minutes. The final layer is fired at 1200°C for 30 minutes to ensure the membrane will remain stable during the thermal

cycling of the electrolyte and cathode. All sintering cycles have a heating rate of 900°C/hr. Faster rates resulted in cracking of the alumina substrate.

4.4.2 Electrolyte Application

The YSZ sol is applied to almost the entire surface of the sample stopping 0.5cm before the LSM anode ends. Each membrane, including the cathode, stops just before the end of the previous membrane. This is to ensure membrane separation and prevent a short circuit. Therefore, every membrane has approximately 0.25-0.5cm exposed at the open end of the sample.

As stated above, three coatings of the sol are required for one layer. Each coat is allowed to dry before the next application. The sintering temperatures for the electrolyte are similar to the electrode layers but are sintered for different time periods. Every 4th layer remains at temperature for 12 minutes while the rest of the layers sinter for 6 minutes. Any excess (non adhered YSZ) is not brushed away after firing. The sample is weighed after every 4th layer until the desired weight is reached. A weight gain of 1.5-2.0g corresponds to a membrane thickness of approximately 20μm. The application of about 50 layers is required to reach the desired weight. The final heat treatment is at 1200°C for 60 minutes.

4.4.3 Cathode Application

The LSM for the cathode membrane is applied and sintered in the same manner as the anode. For this membrane however, 10 layers produces a catalyst surface. The LSM anode layer needs to be thicker than the cathode layer, because it has to provide a barrier

between the substrate and the electrolyte layer. The entire layering process from the anode layer to the cathode layer is represented in Figure 12.

4.5 Sample Completion

4.5.1 Platinum Connections

Platinum patches to aid in current distribution are applied generously over the anode surface with the Hereaus Pt paste. The paste is thinned and applied in the same manner as the platinum conductivity layer. Approximately $50cm^2$ of the surface is covered in Pt although only $1cm^2$ is needed to test for resistance in the circuit to determine if there is an electrical short. The paste is heated to 900^oC, this time for only 5 minutes.

Platinum wire is wound around the sample allowing it to contact with all Pt patches on the anode. A second Pt wire is wound around the end of the sample above the handling area where the original Pt layer is exposed. The wires are adhered to the surface of the samples using another Pt paste from the Ferro Corporation (Platinum Conductrox conductor paste-3804). This paste must also be fired after application to 900^oC for 5 minutes.

Once the Pt wires are attached and the sample has cooled, a digital multimeter (DMM) is used to measure resistance between the top and bottom Pt layers. If there is a $0.0k\Omega$ reading then there is a short in the sample. Obtaining a high resistance reading is desired.
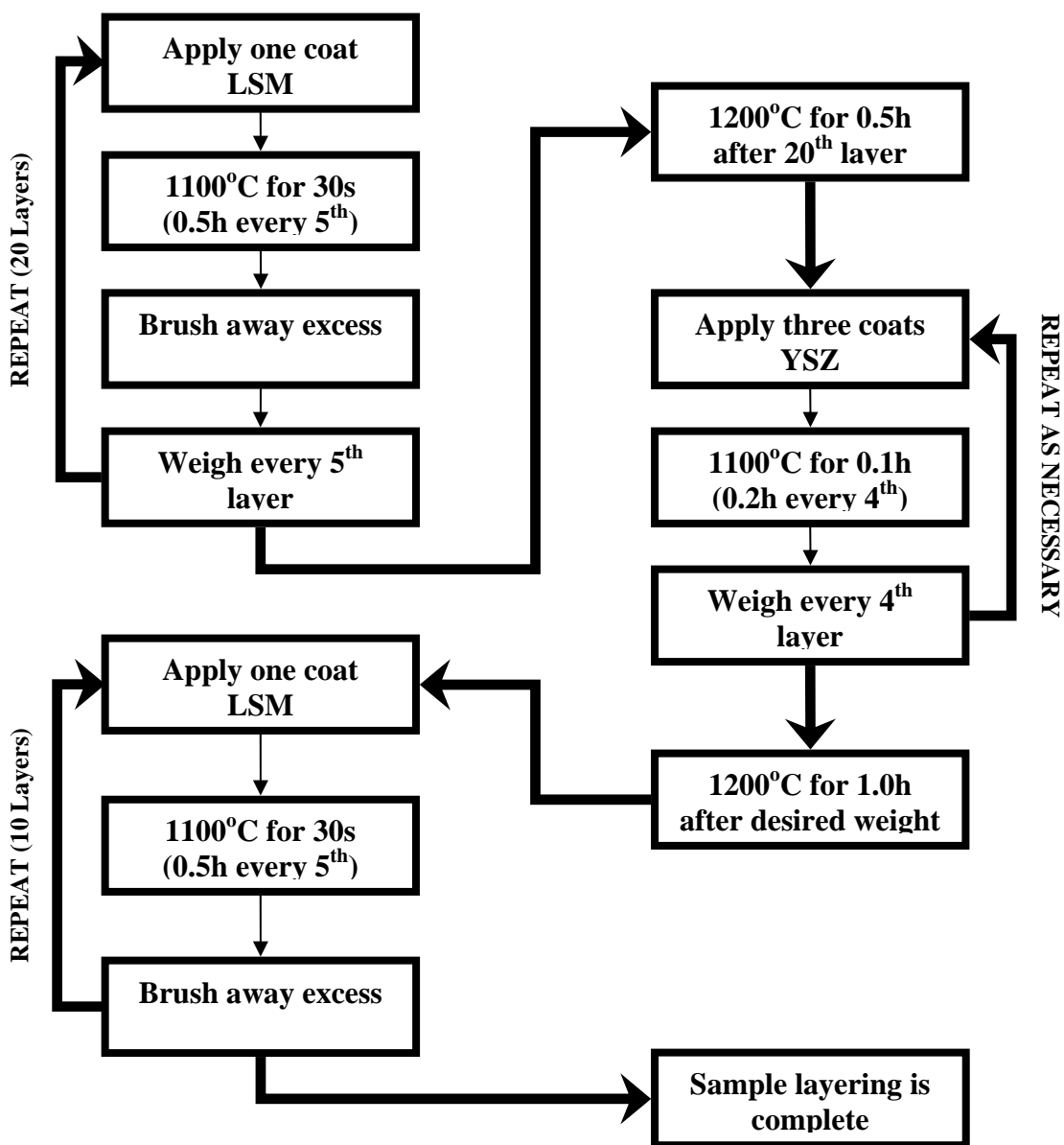
Figure 12: Procedural flowchart for laying the sol-gel membranes for SOFC

<u>4.5.2 Capping the Fuel Cell</u>

To complete the fuel cell, the open end of sample must be prepared to extract any gas accumulated. Dense alumina end caps have been prepared by Norton/Saint Gobain to fit the sample so the end can be capped and sealed. There is a hole in the middle of the end cap used to insert a dense alumina straw where the accumulated gas can exit the fuel cell. The end cap and straw are cemented together and then cemented to the sample using Omega Bond 600 high temperature cement by Omega Engineering Inc.

4.6 Electrochemical Testing

A large tube furnace was used for sample testing. The attached Pt wires were long enough to extend outside the furnace for connection. Two multimeters and a power supply are needed to test the fuel cell. The cathode wire was connected to the positive lead on the power supply and also the COM lead of DMM 1. The anode wire was then connected to the voltage lead of DMM 1. Another connection was made between the anode wire and the current lead of DMM 2. Finally, the COM lead of DMM 2 connects to the negative voltage supply lead. The circuit diagram can be seen in Figure 13.

<u>4.6.1 Monitoring Oxygen Production</u>

The extraction straw was connected to a tubing system that directs the flow of gas to either an oxygen sensor or simply a buret filled with water to observe gas bubbles. The fuel cell was then heated to 800°C and a variable voltage was applied by the power
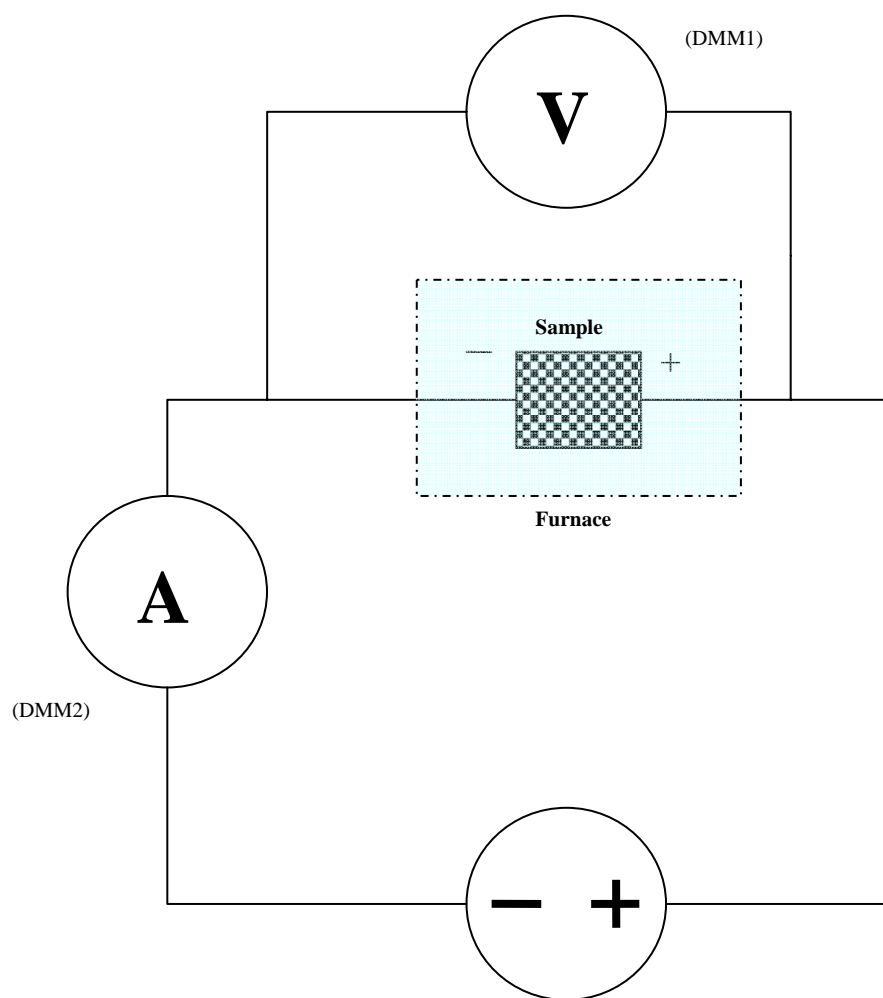
Figure 13: Furnace and electrical schematic for electrochemical testing

source. The voltage in the system was measured by DMM 1 and any current generated was measured by DMM 2. The fuel cell is monitored at temperature for 30-60 minutes to observe gas flow. The voltage is varied from 1-5V to reach approximately 300mA of current within the system. Several cycles are recorded for each sample of current and temperature. The results were reproducible. If a leak occurred, samples could be patched and resealed with high temperature cement.

4.6.2 Testing for Performance as a Fuel Cell

Samples were also tested for performance as a fuel cell. A forming gas comprised of 7% H_2 and 93% N_2 was introduced into the cell through the extraction straw and monitored by a standard Cole-Palmer flowmeter with a measurable limit of 150PSI. At an operating temperature of $800^{o}C$, with no applied voltage, the forming gas was introduced to the anode side and the PSI was then gradually increased and any resulting voltage was recorded. The cathode side of the fuel cell remained in air.

4.7 Thermal Analysis

Thermogravimetric analysis was done to investigate the thermal behavior of the YSZ solution using the Perkin Elmer 1700X/TGA 7. The analysis measured the temperatures at which weight loss occurred. The solutions were put in a drying oven at $70^{o}C$ for 48 hours or until a hardened gel or powder was present. The material was then ground using a mortar and pestle for use in the TGA.

4.8 X-Ray Diffraction

Previous investigations of Y_2O_3-ZrO_2 systems have reported phase changes at specific temperatures [130, 131]. X-ray diffraction was used along with data analysis to confirm that phase changes had occurred when sintered above specific temperatures. Once again, the YSZ solution was dried in a drying oven. The resulting material was sintered at 1100^oC, 1150^oC, and 1200^oC for times ranging from 0.5 to 4 hours. X-ray diffraction powder patterns were collected using a Siemens D500 Diffractometer and the data were analyzed using the Siemens DACO microprocessor.

The powders were exposed over a 20° to 90° 2θ range using a step width and count time of 0.05 and 1 second respectively. The phases were identified using JADE software which compared the pattern to ZrO_2(#72948) and YSZ(#90884, #90885) reference files. The cell parameters for monoclinic, tetragonal, and cubic zirconia can be seen in Table 2 [132]. Figure 14 shows the overlapping diffraction patterns for the three phases between 27° and 33° [132].

4.9 Particle Size Analysis

Particle sizes of the YSZ and LSM solutions were analyzed using the Zeta Potential Analyzer (ZetaPALS) manufactured by the Brookhaven Instrument Corporation. Sample information was collected and mapped by the BIC Particle Sizing Software.

Using a pipette, 2 drops of solution is added to distilled water in a standard

Table 2

Sample	Unit cell parameters, ±0.02 Å								
	t-ZrO$_2$			c-ZrO$_2$	m-ZrO$_2$			
	a	c	c/a	a	a	b	c	β, deg
ZrO$_2$	3.60	5.18	1.44	5.09	5.15	5.20	5.31	99.25
YSZ	3.61	5.17	1.43	5.09	5.18	5.21	5.31	99.23
ZrO$_2$ reference [3]	3.60	5.18	1.44	5.09	5.15	5.20	5.31	99.20

Table 2: Cell parameter for three zirconia phases [132]
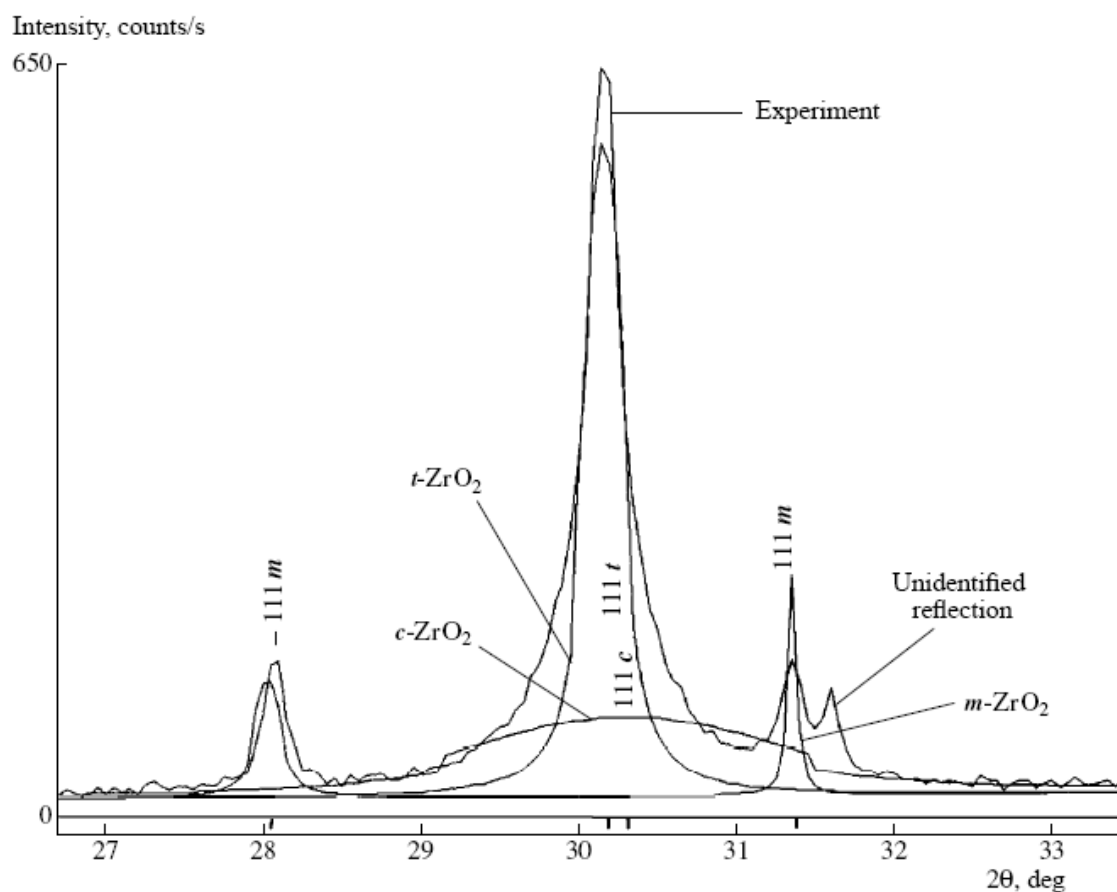
Figure 14: Overlapping XRD patterns for the three ZrO₂ phases between 27° and 33° [132]

cuvette. The sample is put in the ultrasonicator for 10min to separate agglomerates. The equipment uses dynamic light scattering to obtain particle size data using visible light and a background correction determined by the base solution, water. Each sample was analyzed at 658nm. A total of four solutions were analyzed every other day for 10 days. The first YSZ and LSM solutions made were analyzed every other day starting 24 hours after being developed. The second set of solutions was tested every other day starting 2 hours after they were developed.

4.10 Viscosity

A slight variation on the electrolyte sol was also investigated to observe the effect of viscosity vs. weight gain of the YSZ layer. 20ml of ethylene glycol was added before the reaction is catalyzed by the addition of ammonium hydroxide (NH_4OH). The viscosity of EG sols were compared daily with non-EG sols using a Brookfield LVDV-II+ viscometer. A large circumference spindle, #2, was used in all measurements. The solutions were coated on different samples of the same area, referred to as check pieces, to observe any difference in the layers required for weight gain.

4.11 Mechanical Strength

To determine the stability of a membrane under gas pressure, samples were sealed using silicone caulk to the end of a plastic tubing system connected to a flow meter. The sample is placed in water and nitrogen is pumped into the opposite end of the flow meter.

A pressure gauge reports the PSI and if the pressure can be sustained by the sample with no bubbles observed exiting the surface of the sample. The pressure is increased until the sample membrane fails.

4.12 Electrical Measurements

While the cell is heated as described in section 4.6, current and voltage are monitored using the two multimeters attached to the system. Two comparisons are drawn during the electrochemical testing. Voltage is monitored against the temperature while maintaining a constant current.

The second analysis compares voltage and current density (A/cm^2). To measure impedance and obtain polarization data, the sample is held at a constant temperature, most commonly 810^oC. The voltage is increased slowly from 0-1V and the resulting current is recorded.

When monitored as a fuel cell for energy production, the sample is held at operating temperature (800^oC) and H_2 is introduced slowly, increasing the pressure by 5PSI and allowing the system to stabilize.

4.13 Scanning Electron Microscopy

The FEI/Philips XL30 Field Emission Scanning Electron Microscope at Princeton University was used for all sample imaging. Samples were destroyed as necessary to obtain cross sections of the membranes where complete layering (Pt/LSM/YSZ/LSM/Pt)

had occurred. The samples were cut using a fine tooth hand saw to sizes appropriate for SEM analysis, normally less than 1cm^2. The edge of each sample that had all five layers present was polished lightly using a Leco VP-150 polishing wheel at approximately 100 RPM with Leco silicon carbide C weight 1200/1400P grit paper until smooth. Samples were mounted on aluminum SEM studs using double-sided carbon tape. No samples were gold coated allowing YSZ charging to more easily distinguish the membranes.

5.0 RESULTS

5.1 Solution Characterization

5.1.1 Particle Size Analysis

The particle size was determined for two YSZ solutions (A and B) and two LSM solutions (A and B). For the A solutions, measurements were made between 0 and 10 days, and a final measurement after 40 days. For the B solutions, five measurements were made between 0 and 10 days, and again after 40 days. When using LSM solutions, the layering process was finished within 10 days and the remainder of the solution discarded. After 10 days of using the YSZ solution, a new solution was prepared. This was due to the volume of YSZ solution used. No solutions were used past 14 days.

The samples were analyzed using dynamic light scattering at a wavelength of 658nm, with a baseline correction factor determined by the properties of the water mixing base (η=0.890cP, RI=1.330) and the count rate. Ten runs of 1 minute each were run on each sample. After the 10 day analysis the solutions were aged one month at room temperature while stirring to monitor their behavior after expiration.

Figures 15 and 16 show the average particle size for the YSZ and LSM solutions, respectively. The average particle sizes for both YSZ solutions are similar and follow the same trend. The trend is a slight decrease at 4 days, an increase to the initial size by 10 days, and a gradual increase over long times. The LSM solutions follow the same behavior as YSZ and initially decrease in particle size after 4 days of mixing. The particle size increases very slowly as the solution ages. The particle size of the two LSM

Figure 15

Figure 16
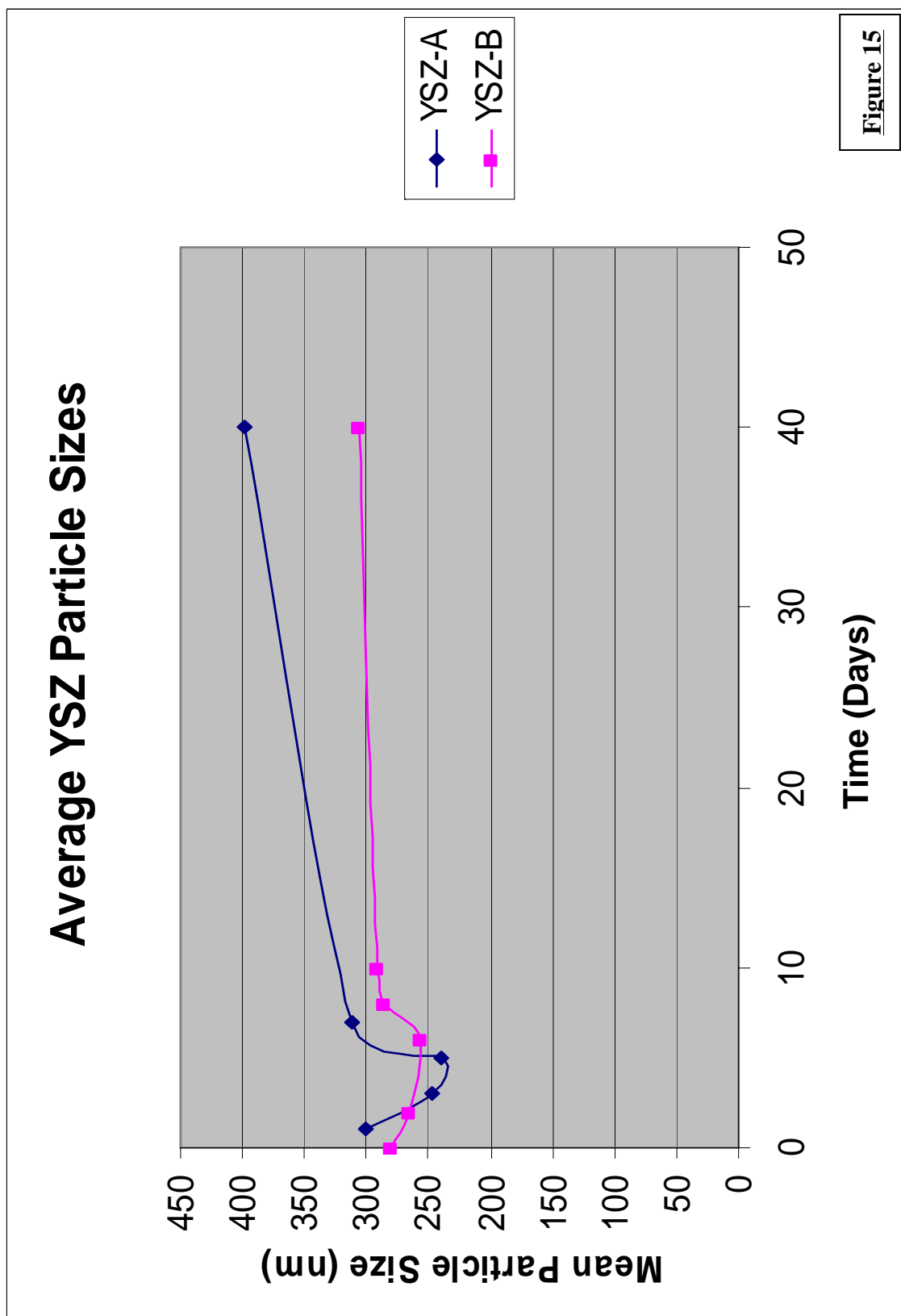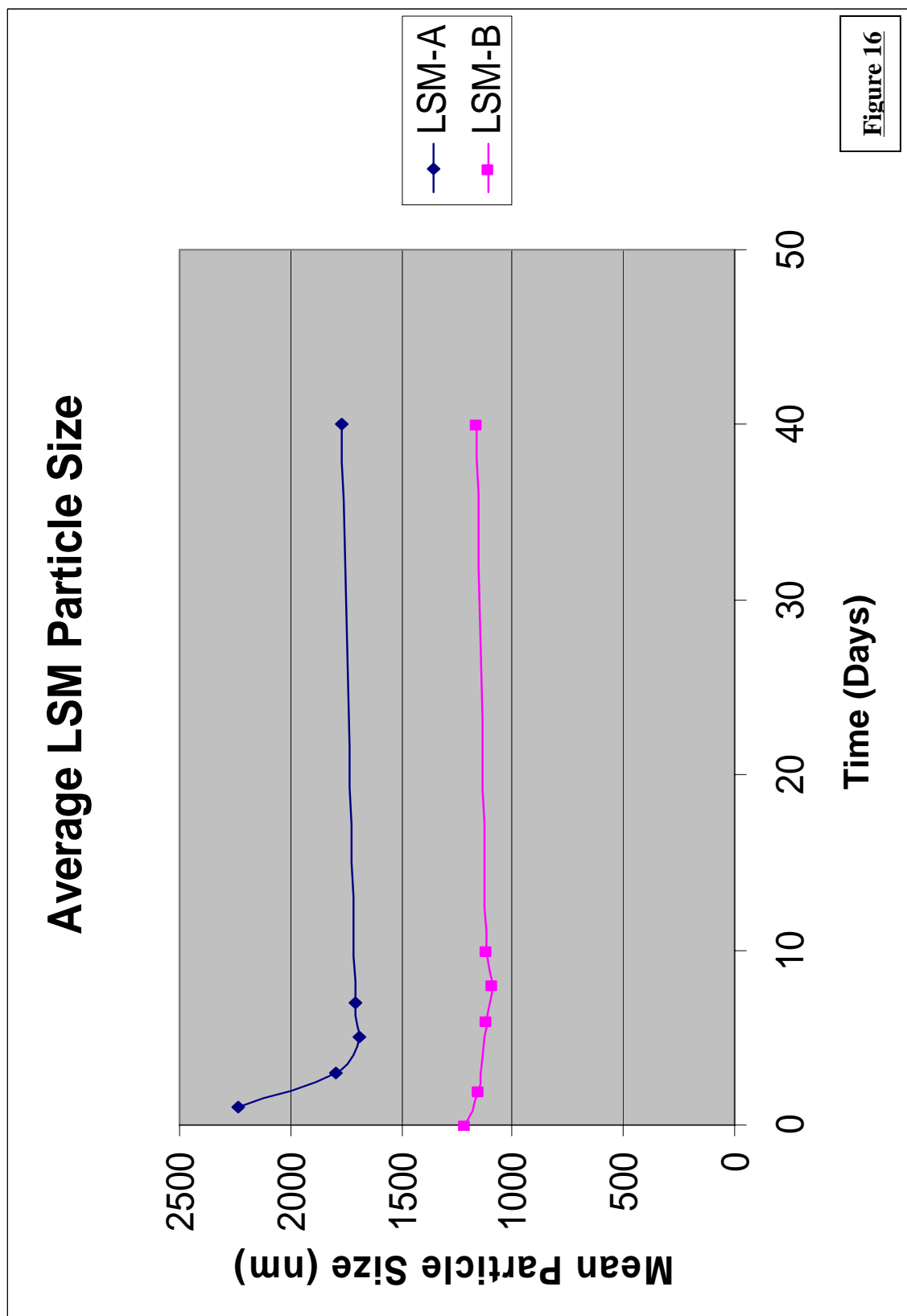
solutions differed by ~500nm. The measured particle size for LSM was 3 to 5 times greater than for YSZ.

5.1.2 Thermogravimetry

The same YSZ solutions that were analyzed in the particle size experiment were analyzed using thermogravimetry. YSZ-A, YSZ-B, and YSZ-X ("expired" YSZ-A: solution aged for 40 days) were investigated. All three samples exhibited similar thermal behavior.

The thermogravimetric traces are shown in Figures 17, 18, and 19. The solutions were originally dried at $70^{o}C$, so there is still some water remaining. Therefore, there is an initial weight loss up to approximately $100^{o}C$ while water is removed. The rate of weight loss decreases then slows until $200^{o}C$. This corresponds to the removal of the alcohol (EtOH). A third reaction occurs between $200^{o}C$ and $300^{o}C$ where there is a sharp drop in weight percent. This is a range in which nitrates and bound water are removed.

The final reaction occurs from $300^{o}C$ to $400^{o}C$ where the weight loss slows once again. In this temperature range, decomposition and dehydroxylation of zirconia gels have been reported to occur [133, 134]. Weight loss is essentially over by $600^{o}C$ and that weight is maintained within the limitations of the experiment, up to $1250^{o}C$. All three samples lost over 50% of their initial weight with the final values ranging between 44-49%. YSZ-A and YSZ-X were nearly identical, losing 56% of their weight. YSZ-B lost 51% of its weight. Previously, a slight difference in particle size was noted between YSZ-A and YSZ-B, with YSZ-B having less variation in its particle size when aged.

Figure 17

TG: YSZ-B

Weight %

Temp °C

YSZ-B

TG: YSZ-X

Figure 19
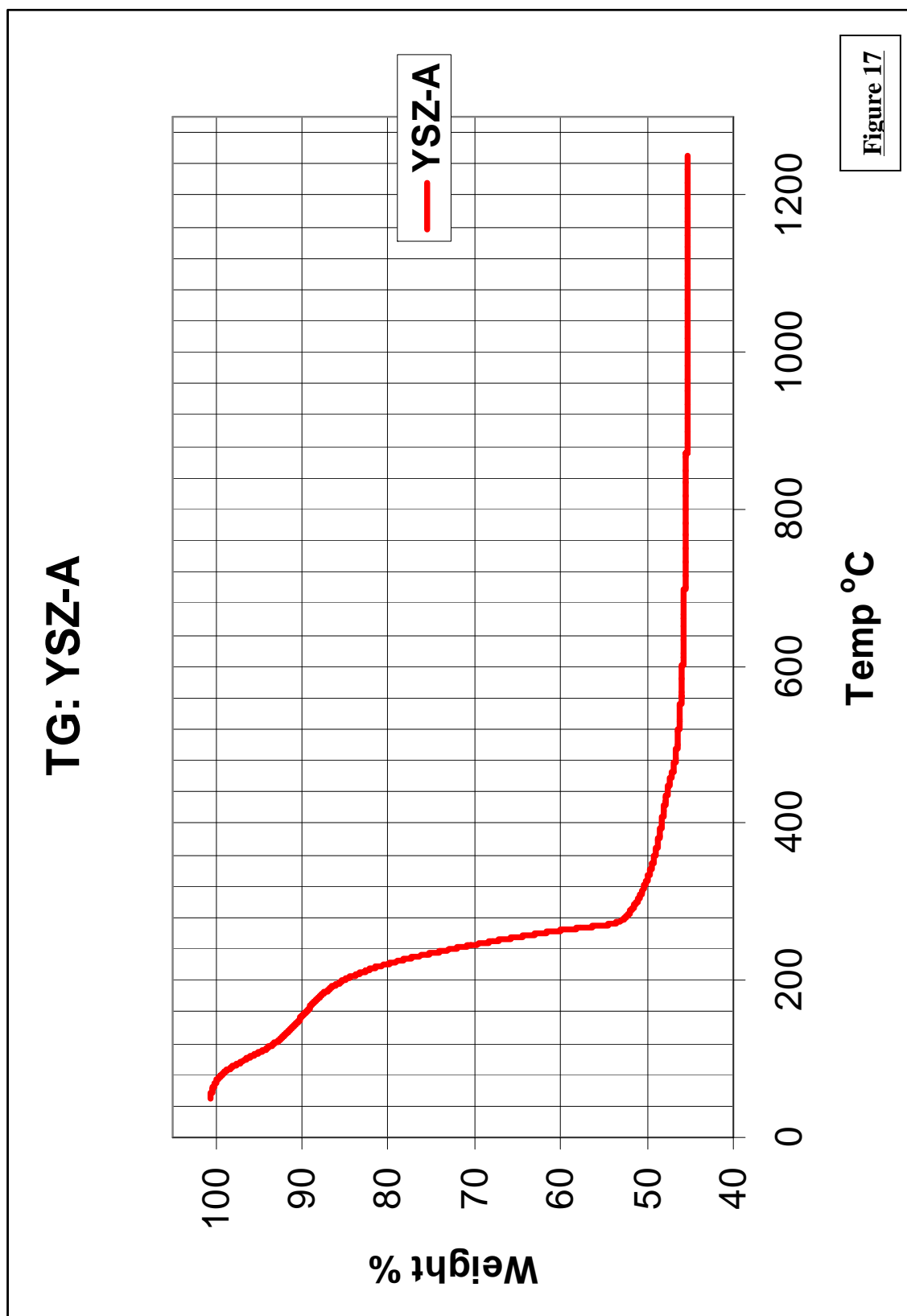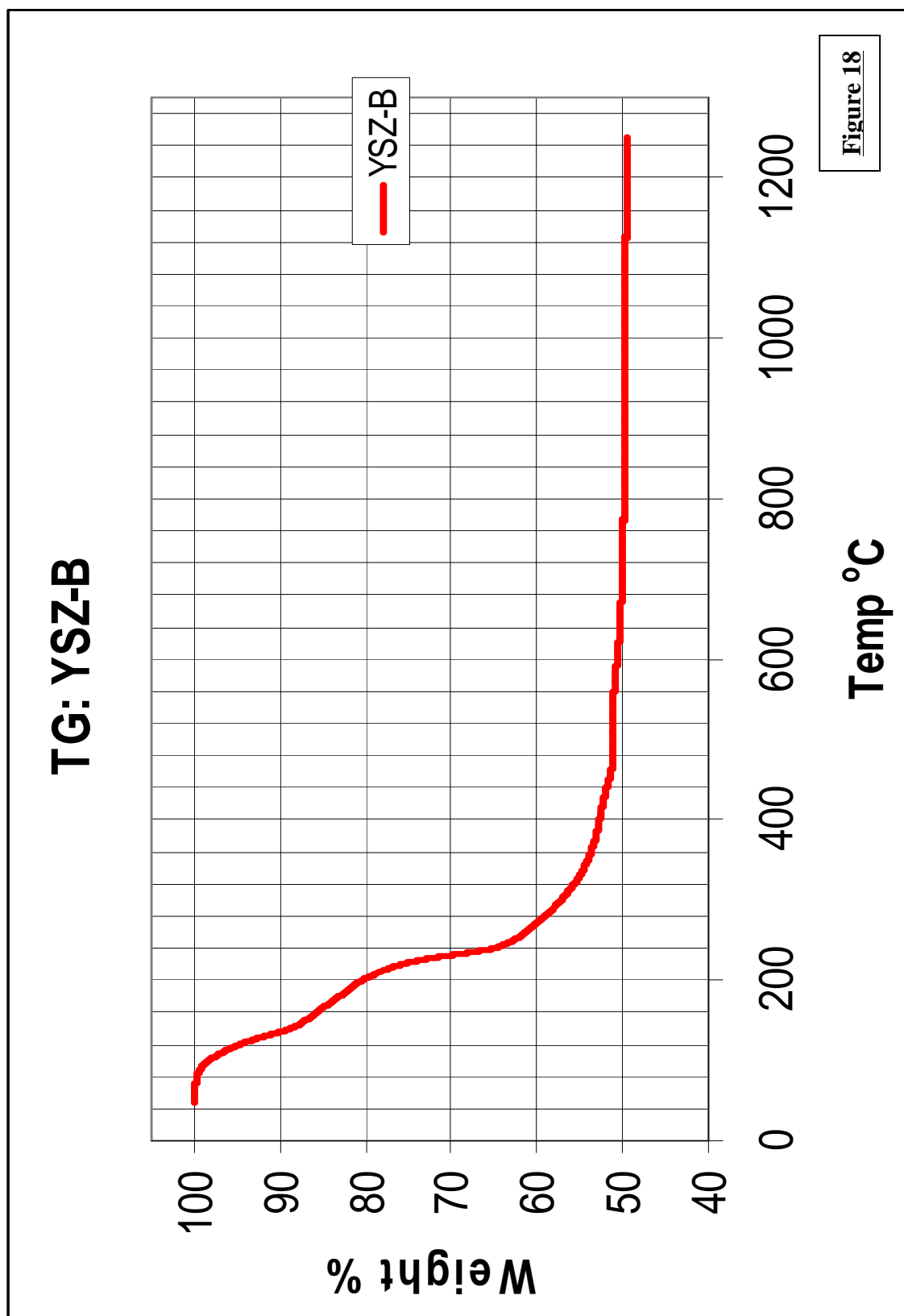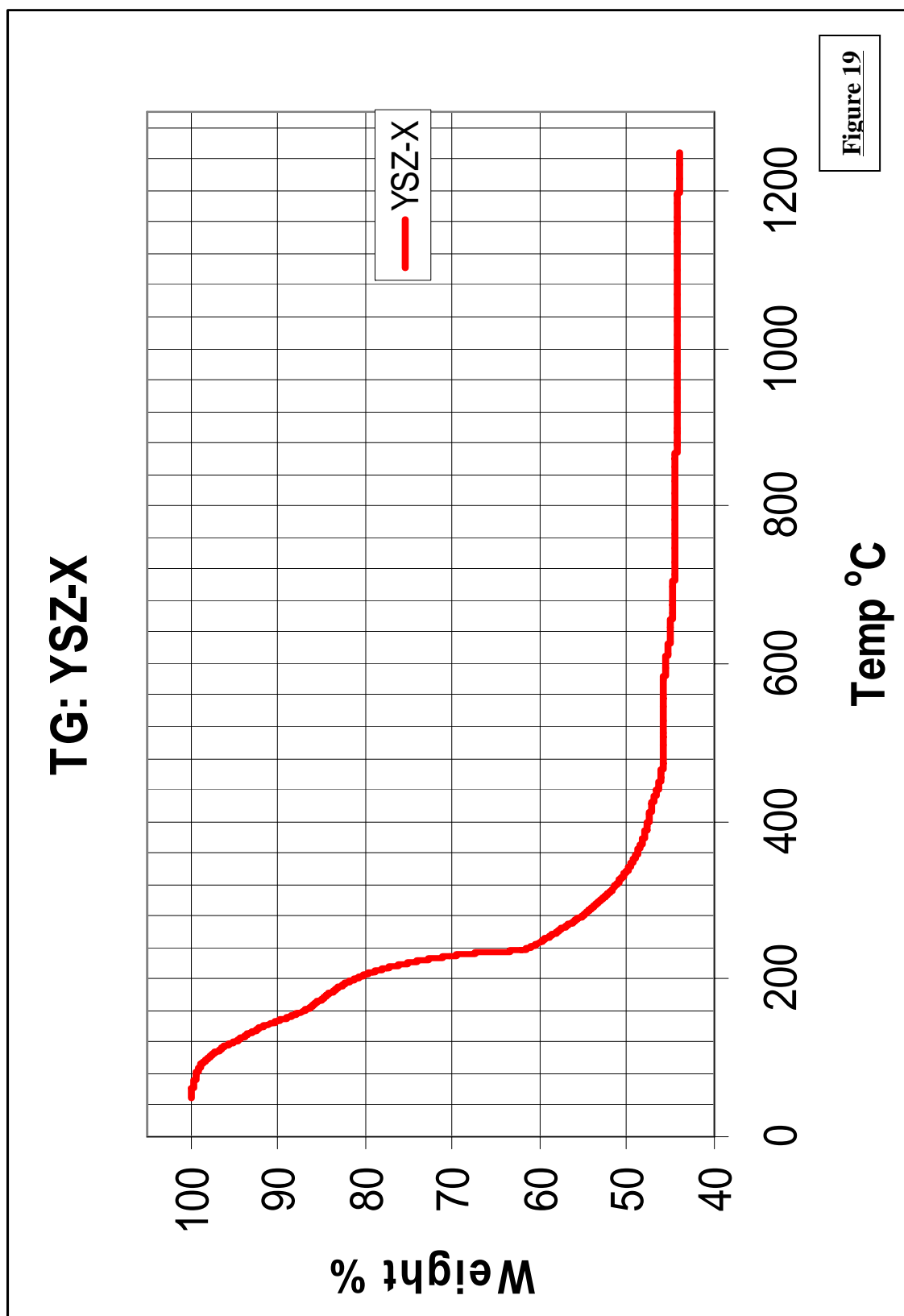
5.1.3 X-Ray Diffraction

X-ray diffraction was performed a number of times over the course of this investigation to ensure the crystal structure of the sintered powders was the same. It was assumed that firing the powders to 1200°C would result in a mixture of tetragonal and cubic phases, predominantly tetragonal. This was based on the phase diagram in Figure 20 [131]. This was confirmed with YSZ powders from different solutions prepared by the method described in Figure 11.

The XRD pattern of a powder prepared in 2004 and fired at 1100°C and 1200°C is shown in Figure 21. More recent solutions of YSZ-A and YSZ-X were analyzed at these temperatures in wide scans and narrow scans around the diffraction peak ~30° in 2θ and can be seen in Figures 22-26. There was little change between 1100°C (Figure 22) and 1200°C (Figure 24). Also, there was no difference between YSZ-A (Figure 22) and YSZ-X (Figure 25) at 1100°C. The presence of a cubic phase was not detected in any of the patterns.

5.1.4 Viscosity: EG vs. non-EG

The effect of ethylene glycol (EG) on the viscosity of fresh and aged solutions was determined. YSZ-EG solutions behaved similarly to non-EG solutions with respect to an increase in viscosity as the solution aged. The viscosities of the EG sols (Figure 27) began significantly higher than the viscosities of the non-EG YSZ (Figure 28) as expected, by approximately 30 centipoise (cP). Figure 26 shows the viscosities of EG sols beginning with the day the sol was made (day 1), to the end of its use (day 9). These sols had an initial viscosity of at least 89cP and the viscosity usually exceeded 100cP at
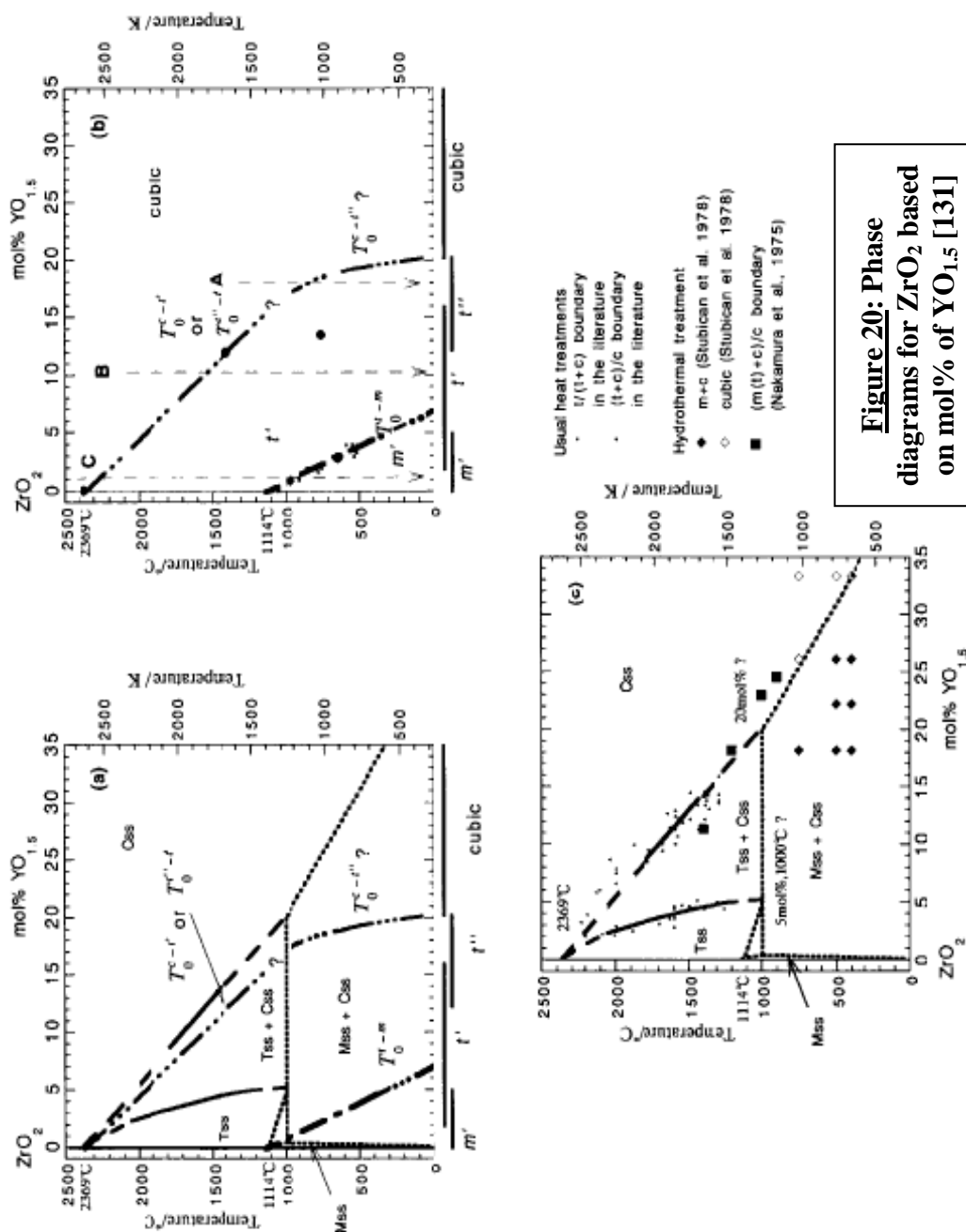
Figure 20: Phase diagrams for ZrO_2 based on mol% of $YO_{1.5}$ [131]
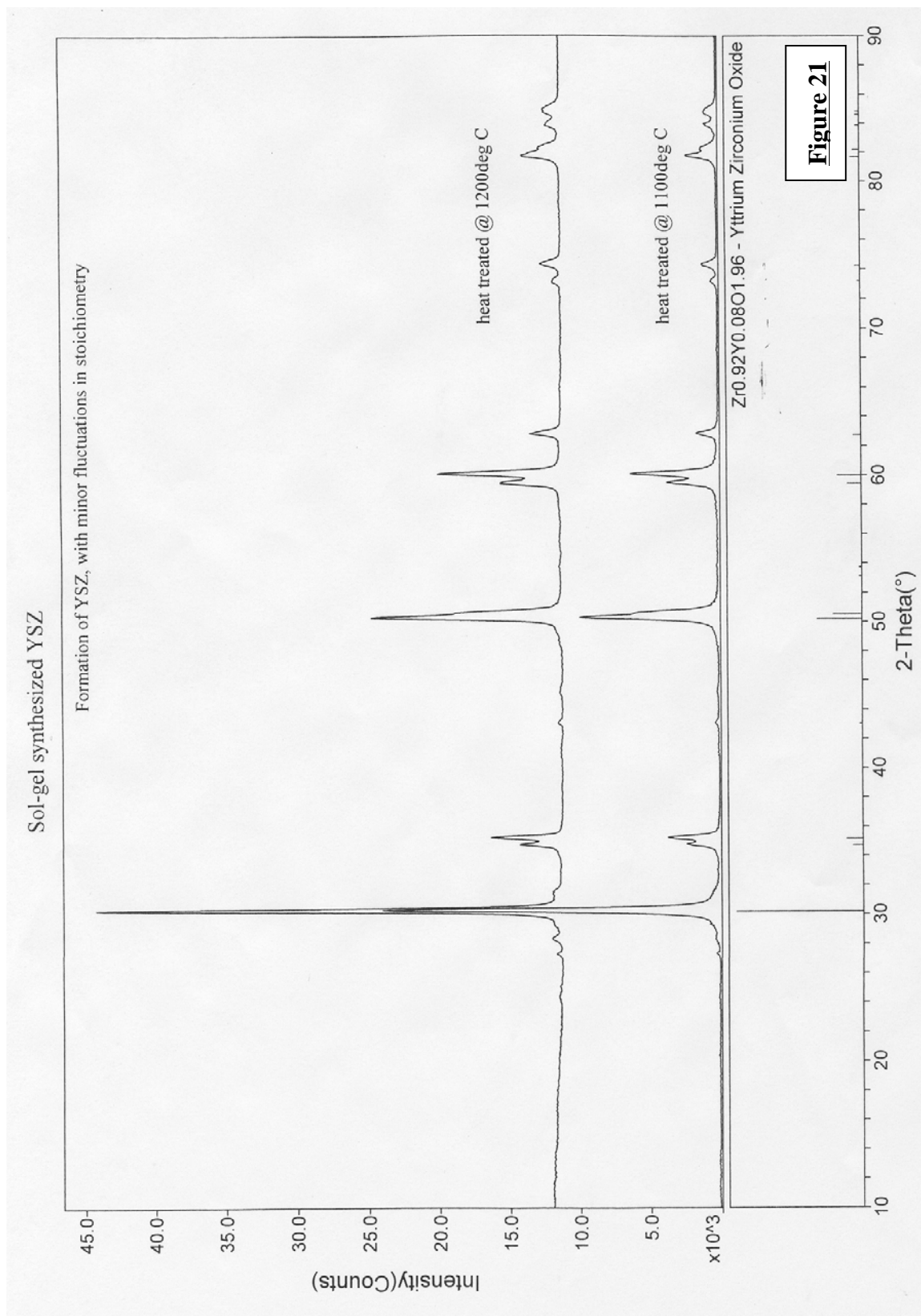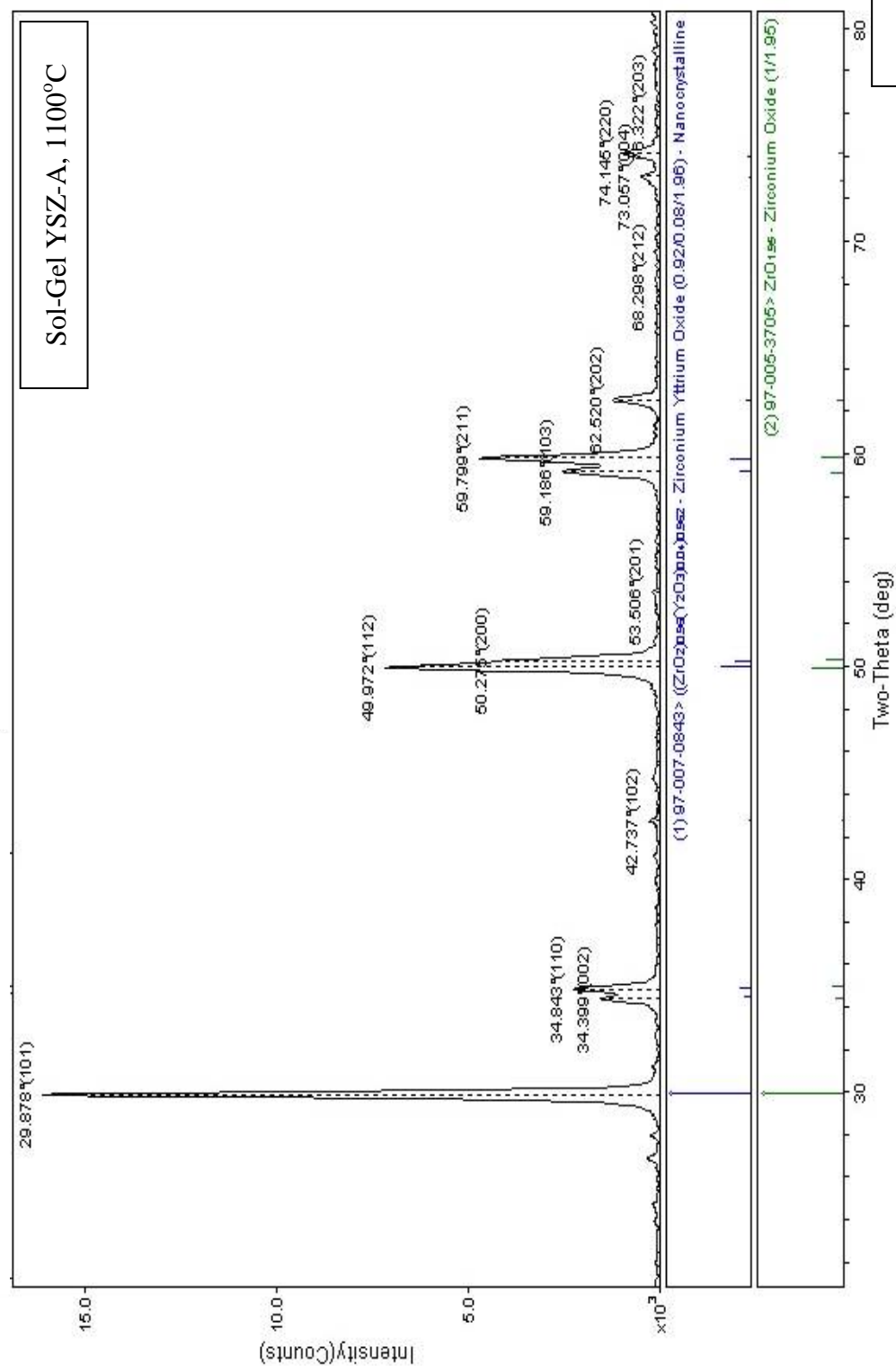
Figure 21

Figure 22

Figure 23

Figure 24

Sol-Gel YSZ-X, 1100°C

97-007-0842> ((ZrO2)0.97s(Y2O3)0.0296)0.97s - Zirconium Yttrium Oxide (0.95/0.06/1.97) - Nanocrystalline

Two-Theta (deg)

Intensity(Counts)

Figure 25

Sol-Gel YSZ-X, 1100°C

Figure 26

Figure 27

Viscosites for non-EG Sols

Legend:
- Sol-A(non-EG)
- Sol-B(non-EG)
- Sol-C(non-EG)
- Sol-D(non-EG)
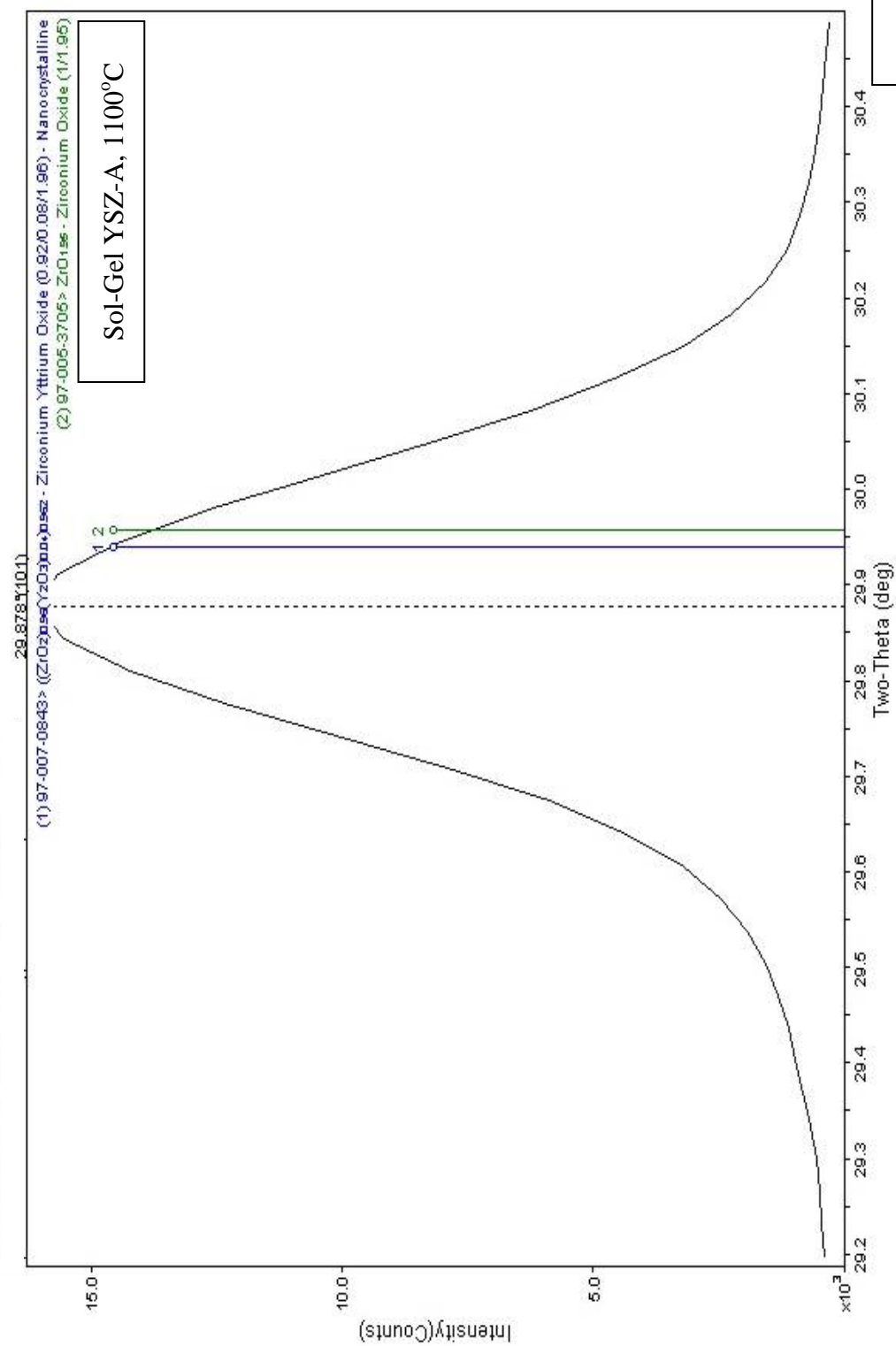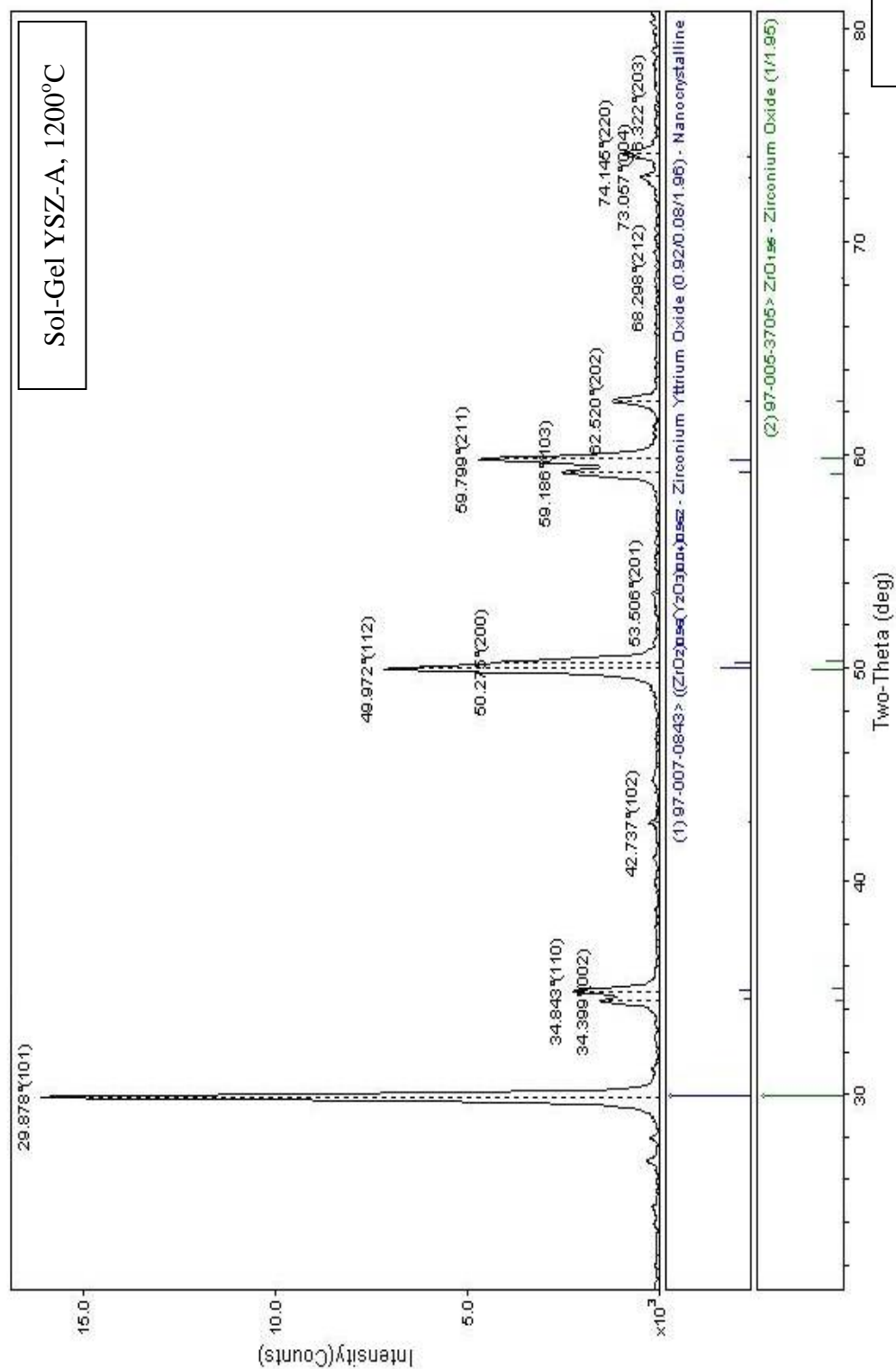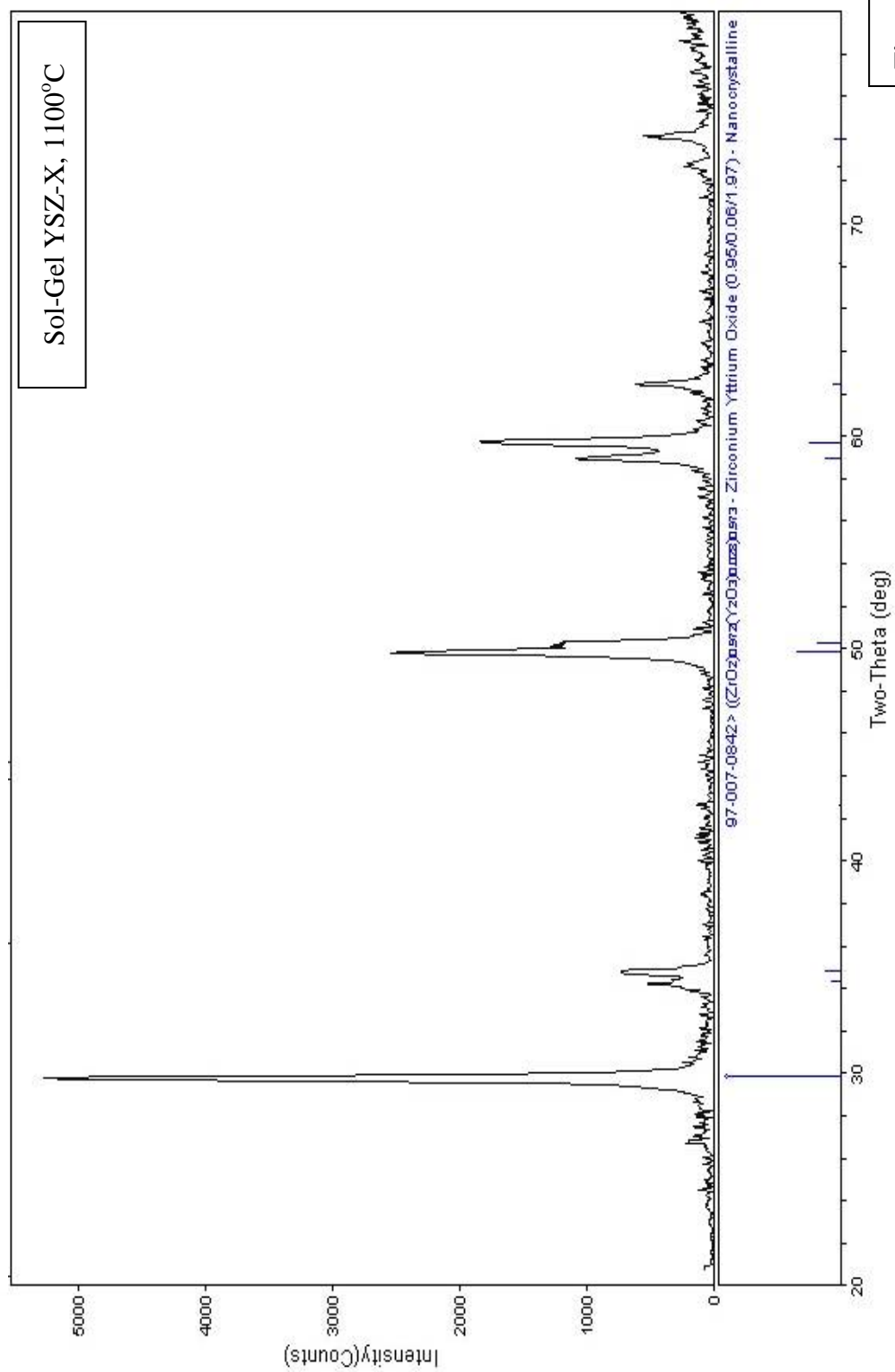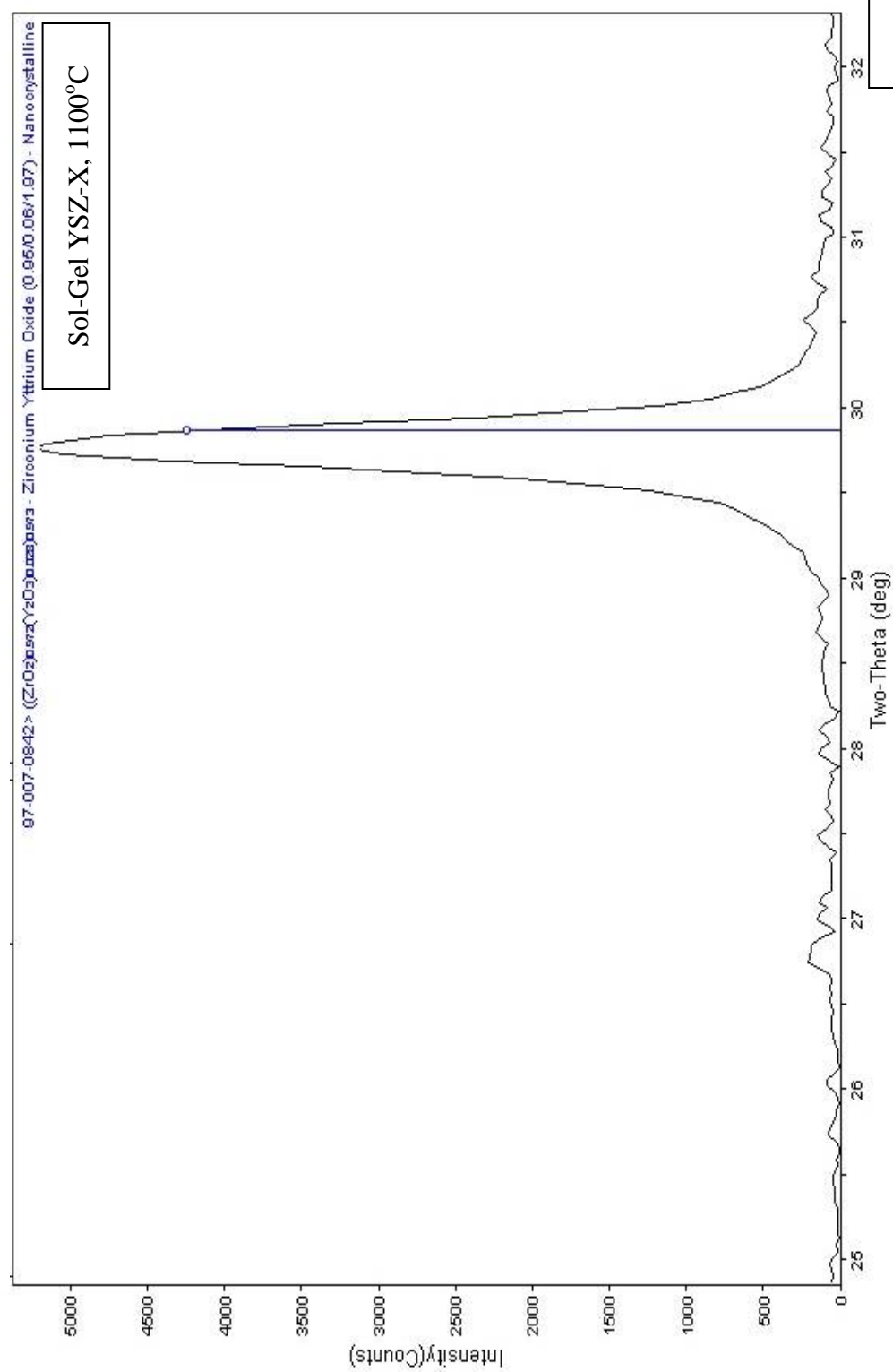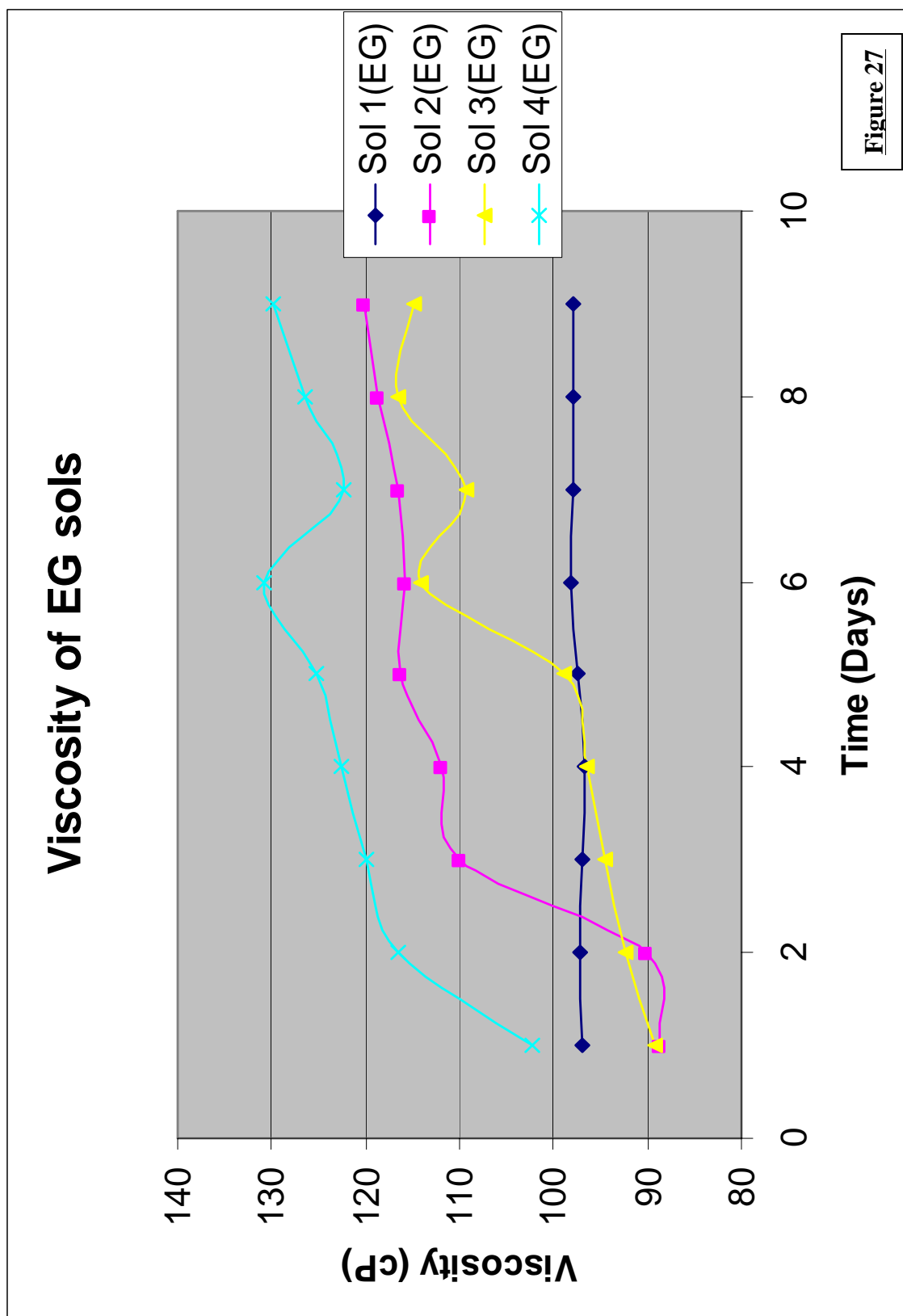
Viscosity (cP)

Time (Days)
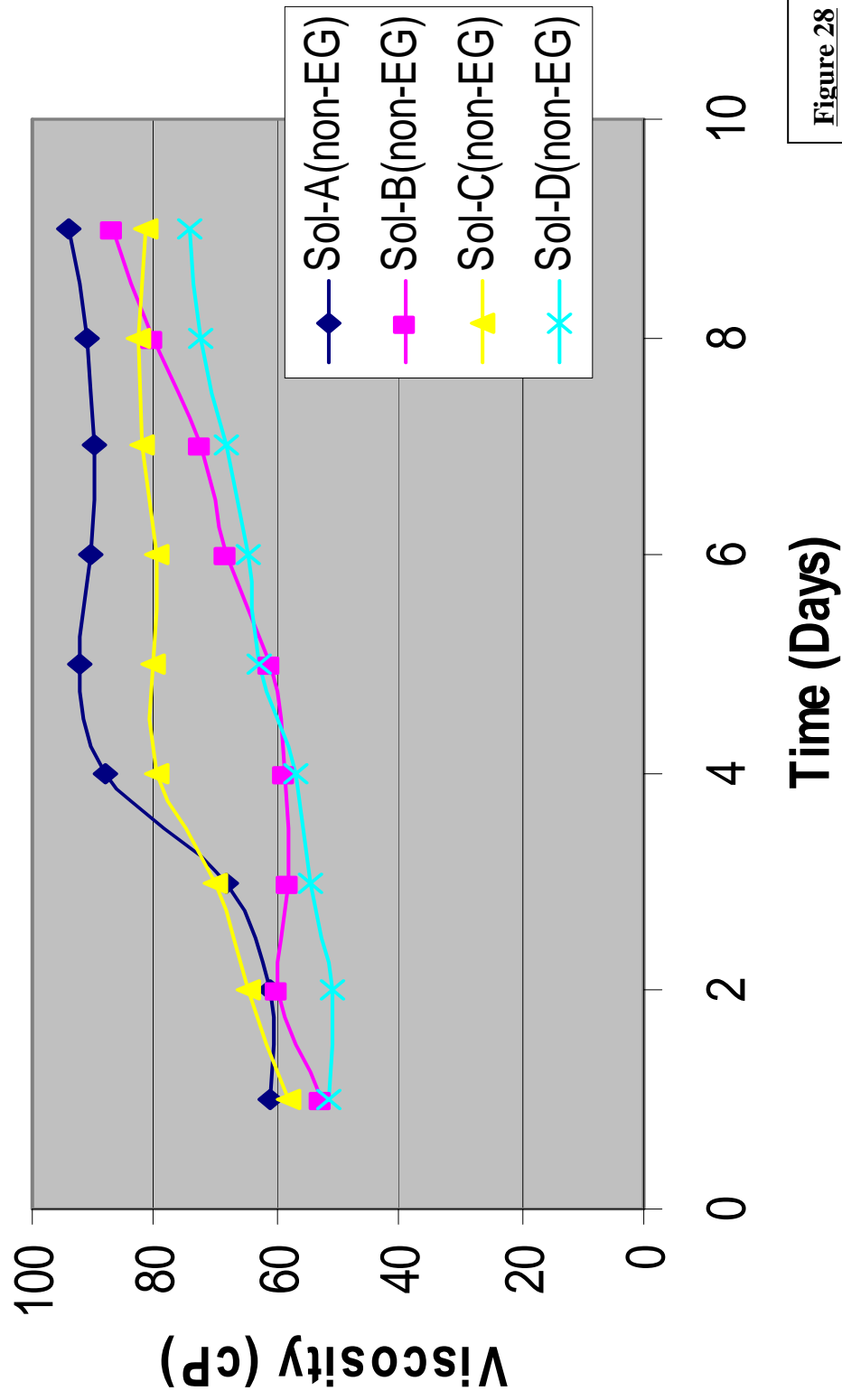
Figure 28

the end of the 9 days. In Figure 28, the non-EG sols had an initial viscosity between 50 and 60cP. Only one sample of the non-EG solution measured above 90cP during testing.

5.2 Properties of the Assembled Device

A total of eight full samples were assembled. In most cases, a small piece was prepared simultaneously with the full sample and was referred to as the "check piece". These are listed in Table 3. The larger samples and their processing characteristics are listed in Table 4.

5.2.1 Weight Gain

The weight gain for the layers was monitored for all samples except #13S(1), #13S(2), #13B, tube 6, and tube 7.

5.2.1.1 Weight Gain: EG vs. non-EG

All check pieces are full length samples cut in half, ~53cm^2 of active surface. Half sample pieces were layered using the brush coating method for all layers. Figure 29 shows the number of YSZ layers vs. the weight gain of four check pieces. There are two EG samples, chk-11 and chk-12, as well as two non-EG samples, chk-13 and chk-14. Not all samples received an equal number of layers. The sample chk-11 gained more weight with the EG solution then the other samples, by 0.5g. With each layer, the samples should have shown gradual increases, but the process resulted in flaking and chipping, leading to the recorded weight losses. Overall, there was a net weight gain.

Table 3: Check piece samples and preparation methods

Sample	Layers	Process	SEM	Electrochemically Tested	O$_2$/Electrical Production
Chk-3	LSM/YSZ(48)	Brush	No	No	No/No
Chk-4	LSM/YSZ(48)	Dip	No	No	No/No
Chk-7	LSM/YSZ(64)	Brush	No	No	No/No
Chk-8	LSM/YSZ(64)	Brush(EG)	No	No	No/No
Chk-9	LSM/YSZ(68)	Brush	No	No	No/No
Chk-10	LSM/YSZ(100)	Brush	No	No	No/No
Chk-11	LSM/YSZ(128)	Brush(EG)	No	No	No/No
Chk-12	LSM/YSZ(108)	Brush(EG)	No	No	No/No
Chk-13	LSM/YSZ(84)	Brush	No	No	No/No
Chk-14	LSM/YSZ(16)	Brush	No	No	No/No

Sample Name	#13-small(1)/(2)	#13big	Tube 6	Tube 7	10-31-00	11-01-00	06-30-00	09-19-00
Layers	LSM YSZ(40/50) LSM	LSM YSZ(50) LSM	LSM YSZ(50) LSM	LSM YSZ(50) LSM	LSM YSZ(58) LSM	LSM YSZ(58) LSM	LSM YSZ(50) LSM	LSM YSZ(96) LSM
Process	Brush	Brush	Brush	Brush	Brush	Dip	Brush	Brush
SEM	Yes	Yes	Yes	Yes	No	No	Yes	Yes
Electrochemical Test	Yes	Yes	Yes	Yes	No	No	Yes	Yes
O₂/Electrical Production	No/No	No/No	No/No	No/No	No/No	No/No	No/Yes (only one tested)	No/No

Table 4: Full Sample Labels and Processing Method
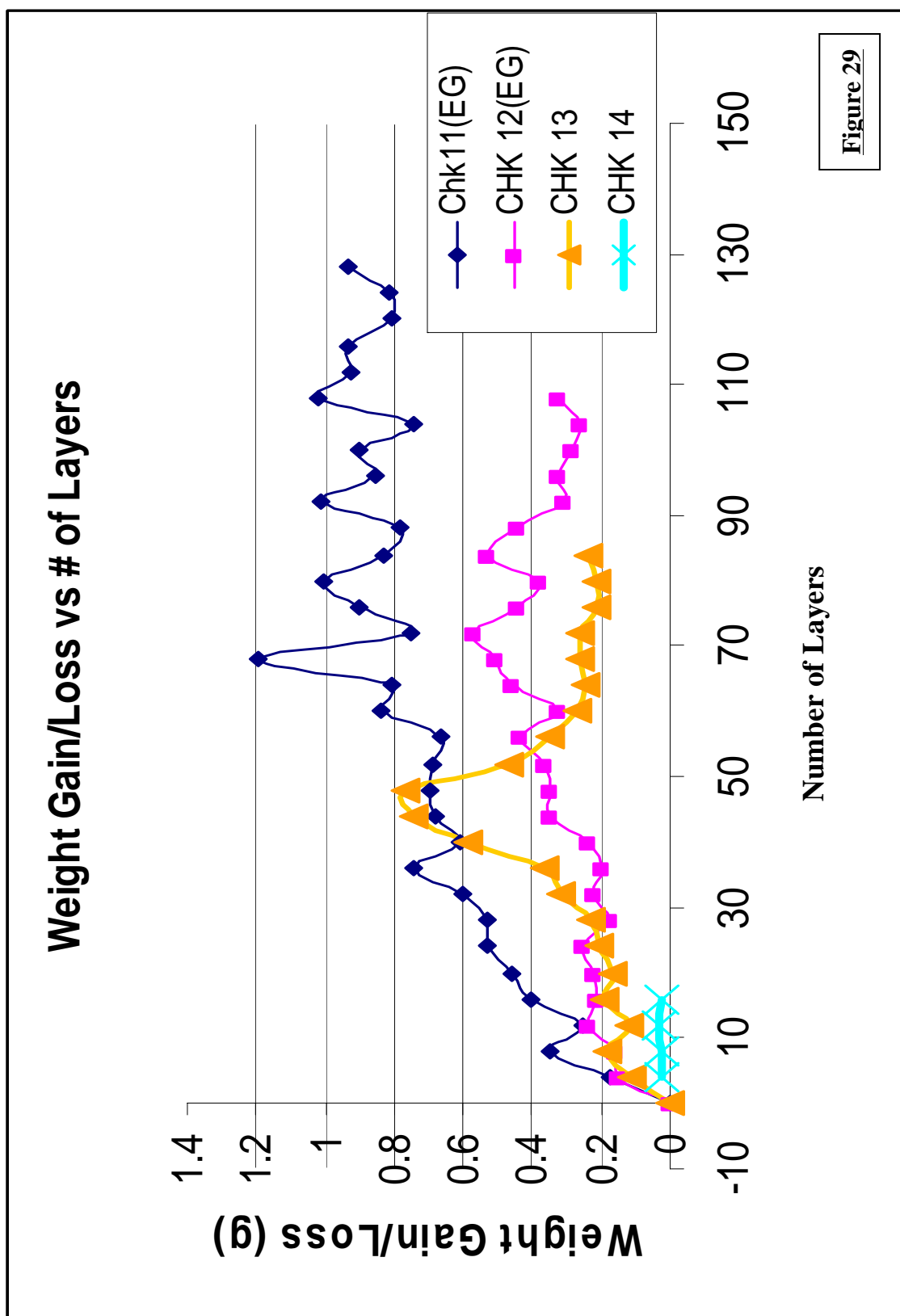
Figure 29

Chk-11 was then compared to the weight gain on four more samples, chk-7, 9, and 10 (non-EG) and chk-8 (EG) in Figure 30. Chk-11 gained approximately at the same rate as chk-8 but both showed substantially lower weight gain then the non-EG samples, chk-9 and chk-10. At times the two non-EG samples had gained 1.0g more than the EG samples.

5.2.1.2 Weight Gain: Brush vs. Dip Coating

Two full samples and two check pieces were compared to each other using different application techniques, brush and dip coating. 13-11-01-00 and chk-4 were the only samples dip coated in these experiments. They were compared with brush coated samples, 13-10-31-00 and chk-3.

The check pieces were compared up to 48 layers, and the full samples up to 58 layers. The total weight gain of the samples gained is shown in Figure 31. Chk-3 showed modest overall weight gain during layering through the brush technique with a small weight loss every 8-12 layers. The dipped sample, chk-4 had considerable changes both gains and losses. Aside from the initial 3 measurements in which chk-4 gained substantial weight, it never exceeded a total weight gain of ~0.37g that was reached in the first 12 layers. Although chk-3 gained much more slowly, reaching approximately 1/3 of the weight gain in 48 layers as chk-4, the sample exhibited a positive trend.

Sample 13-11-01-00 also yielded erratic weight gains and losses compared to that of 13-10-31-00. The resulting weights of each full sample after 58 layers were similar. The brushed sample rarely had a weight change as large as its dipped counterpart and again followed a much more consistent positive trend.
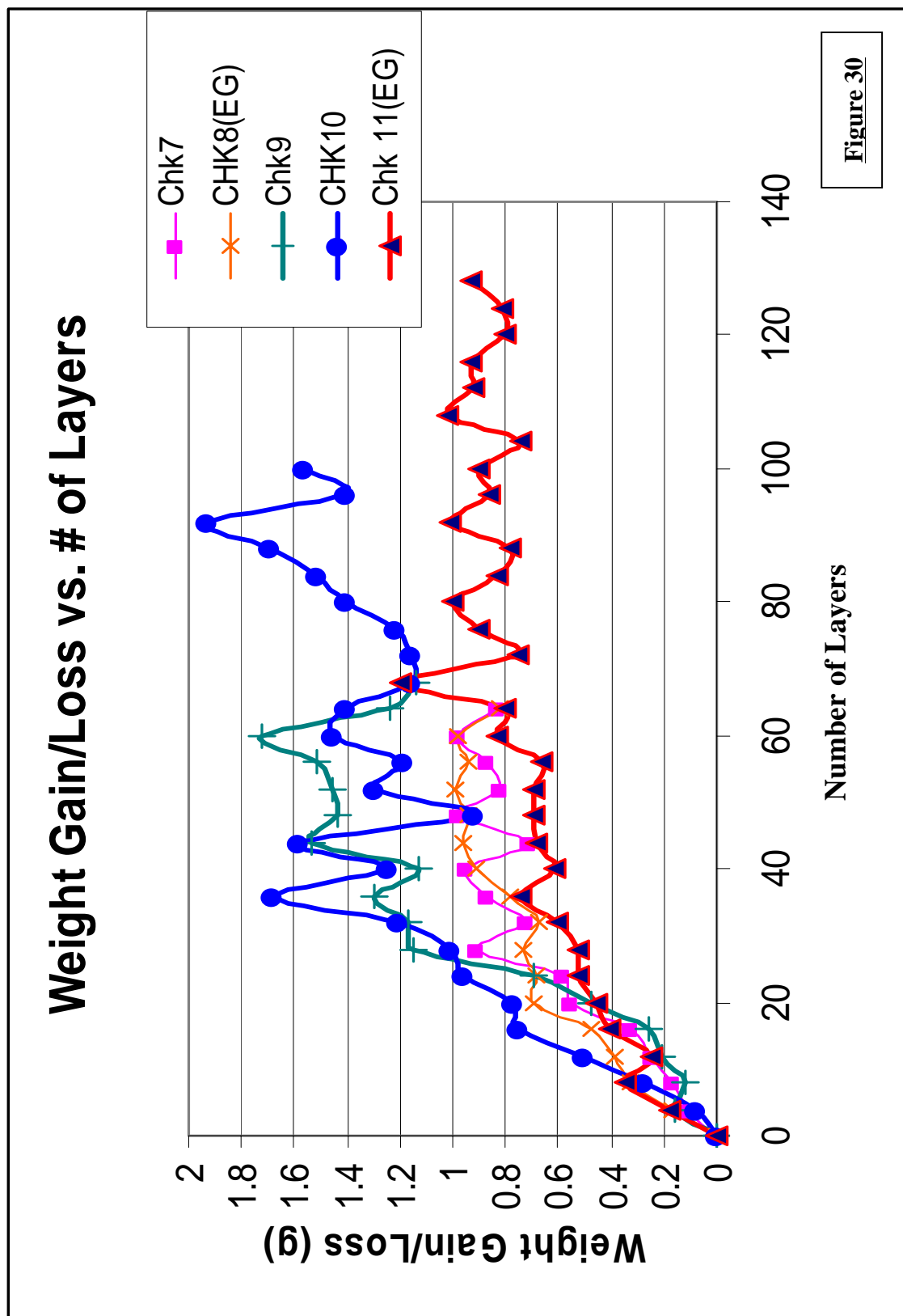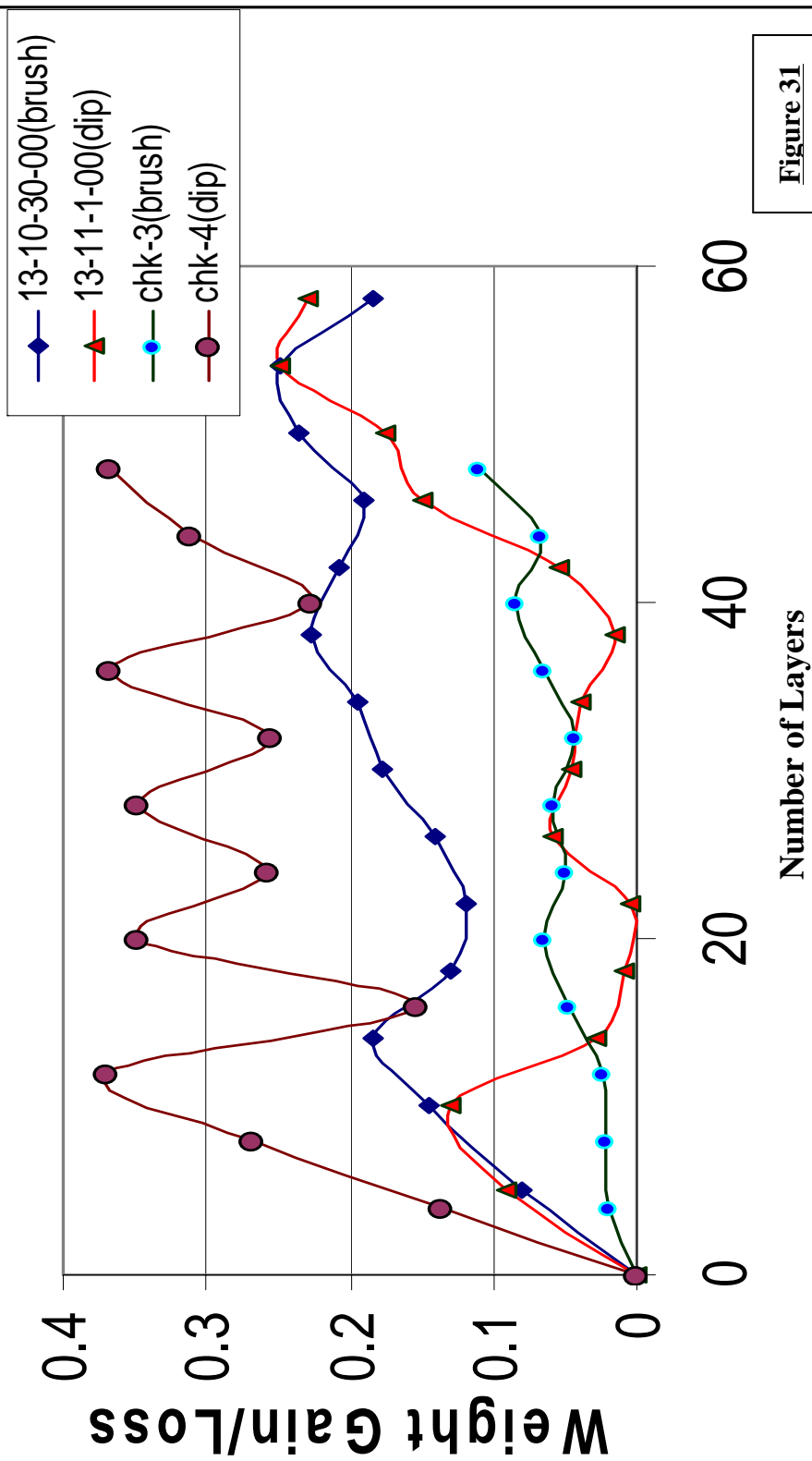
Figure 30

Figure 31

5.2.1.3 Weight Gain: Completed Samples

Samples 06-31-00 and 09-19-00 were layered using non-EG YSZ solution and brush coated. Sample 06-31-00 received 50 layers of YSZ solution and gained 0.15-0.25g at every measurement. After the final YSZ heat treatment, the sample had gained 1.70g yielding ~0.018g/cm^2.

To determine the effect of the electrolyte thickness on electrochemical data, sample 09-19-00 received almost twice the layers of 06-31-00 in an attempt to increase the layer thickness by ~1.0g. After 96 layers, the electrolyte membrane was stopped and the sample had gained 2.5637g, 0.84g more than 06-31-00. Over the entire surface approximately 0.027g/cm^2 was gained on the sample. There were a few significant weight losses between 0.1g and 0.2g, causing 09-19-00 to gain poorly within the first 50 layers only reaching a total weight gain of 0.3g. The sample then gained very well thereafter until the end of the layering process. The weight data of the two samples is compared in Figure 32.

5.2.2 Electrochemical Testing

Electrical data were collected on all samples with completed membranes (anode, electrolyte, cathode, platinum). Two partial samples were electrochemically tested. Sample #13-small(1), #13small(2), and #13-big can be seen in Figure 33(a). Four full samples were electrochemically analyzed. Samples 6, 7, 06-31-00, and 09-19-00 are pictured in Figure 33(b)-33(d). No oxygen flow was observed in any tests.

Weight Gain vs. # of Layers

Legend: 6/30/2000, 9/19/2000

X-axis: Number of Layers

Y-axis: Weight Gain(g)
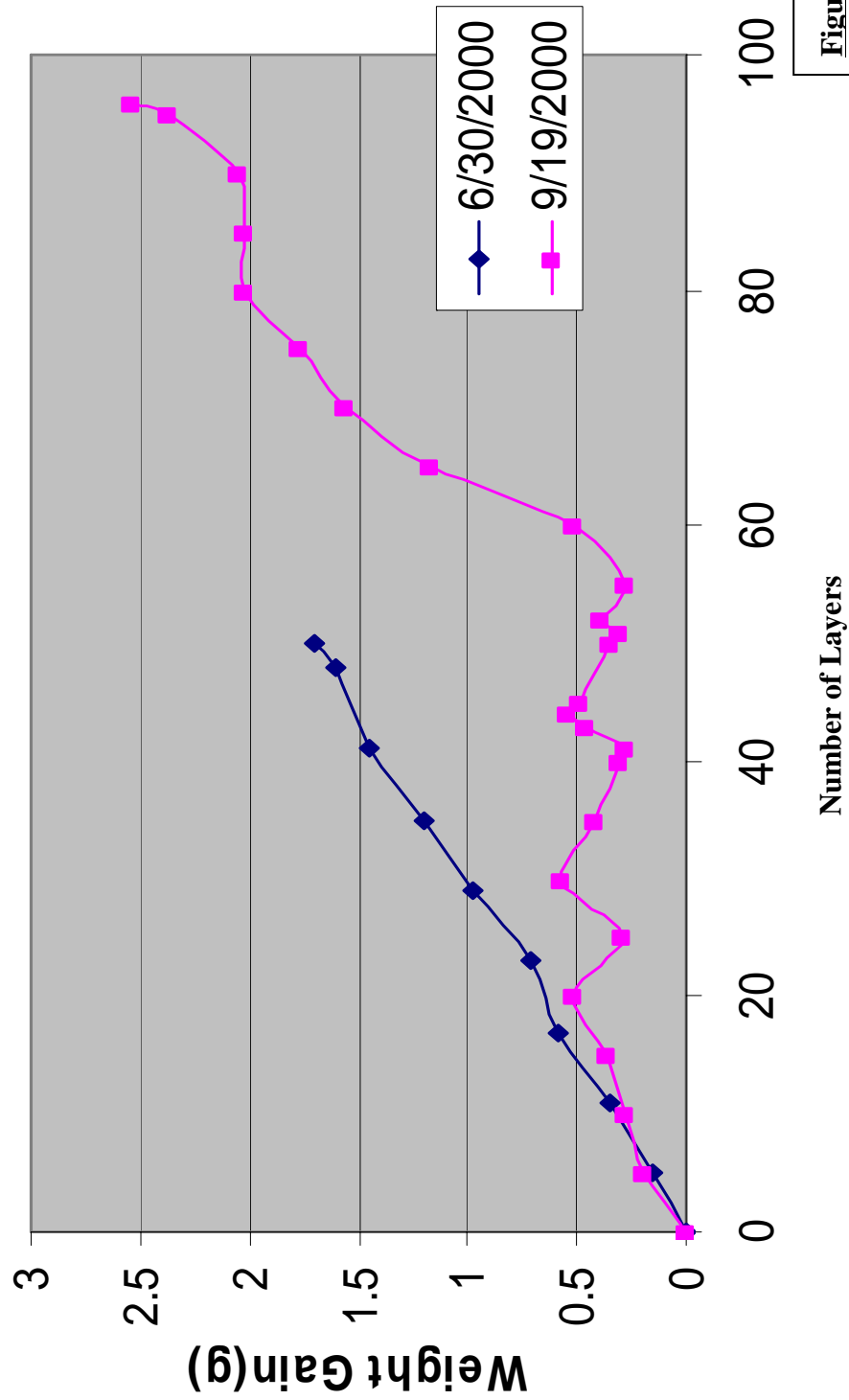
Figure 32

**Figure 33(a)**

Figure 33(b)

Figure 33(c)

Figure 33(d)

Figure 33: (a) Samples #13S(1), #13S(2), #13B (b) Tube 6 and 7(after dome removed) and chk-11 (c) 06-30-00(left) and 09-19-00(center) (d) closeup of 06-30-00 Pt patches

5.2.2.1 Samples #13small(1), #13small(2), #13big

Samples #13small(1) and #13small(2) were originally one large sample. At 40 layers of YSZ sample #13small fractured into two smaller pieces. One piece, #13small(1), was completed with LSM and Pt with only 40 layers of YSZ. The other piece, #13small(2), had 10 more layers of YSZ applied for a total of 50 and was then finished with LSM and Pt.

Sample #13small(1) required only 0.4V to maintain 300mA of current at room temperature. The voltage consistently decreased with increasing temperature and leveled off at 0.07V at $400^{\circ}C$. Sample #13small(2) with 10 more layers of YSZ required 0.66V initially. The voltage also decreased to 0.7V but was not achieved below $800^{\circ}C$ (Figure 33).

#13big was tested at three different Pt patches. All three patches required just over 1V (1.06-1.09V) to maintain 300mA of current at room temperature. The patches maintained a steady voltage up to $600^{\circ}C$ where patch 1 began to require less voltage. The voltages of patches 2 and 3 began to drop at $700^{\circ}C$ and $725^{\circ}C$, respectively. Both of these patches had shown their lowest required voltages at $860^{\circ}C$.

The degree of polarization is a measure of how the rates of the anodic and the cathodic reactions are retarded by various environmental and surface processes. The variation of potential as a function of current (a polarization curve) allows one to study the effect of concentration and activation processes on the rate at which anodic or cathodic reactions can give up or accept electrons. Hence, polarization measurements can thereby determine the rate of the reactions that are involved in the reduction process, the reduction rate. In these investigations, polarization data was obtained only to

determine the quality and consistency of the sample without associating a corrosion rate. All data was measured at 810^oC.

The polarization curves (Figure 35) for #13small(1) and #13small(2) match closely. The curves were linear and showed a relatively high current density at low voltage. For both samples 0.11V yielded $0.1A/cm^2$. Sample #13big also showed a linear relationship for each of the three patches tested. However, a current density of $0.1A/cm^2$ was not reached until 0.6V.

All electrochemical data (T vs. V, polarization curve) for both #13small samples and #13big are represented in Figure 34 and Figure 35.

5.2.2.2 Tube 6

Several platinum patches were tested on tube 6. All patches behaved similarly when heated. Each patch required 1V-1.1V to maintain a current of 300mA (Figure 36). Each patch performed consistently during different test runs. The voltage at each patch reduced drastically once 600^oC was reached and the voltage was reduced to approximately 0.02V at 850^oC in all tests.

The polarization data at 810^oC agrees with the voltage and temperature data obtained (Figure 37). The patches were consistent during separate tests and performed similarly to one another. By 0.25V the current density of each patch measured close to $0.08A/cm^2$.

Figure 34

Polarization Curve at 810°C for Samples #13small, #13big

Legend:
- #13-small(50YSZ, 0.5h)
- #13-big:patch2(50YSZ, 1h)
- #13-big:patch3(50YSZ,1h)
- #13-big:patch1(50YSZ,1h)
- #13: small(40YSZ,0.5)

Current Density (A/cm2)

Voltage (V)

Figure 35

Temperature vs. Voltage: Tube #6-Patches 1,2,4

Legend:
- Patch4.2:Run2
- Patch4.2:Run1
- Patch 4.1: Run 1
- Patch 2: Run 1
- Patch 1: Run 1
- Patch 1:Run 2
- Patch 2: Run 2

X-axis: Temp (°C)
Y-axis: Voltage (V)
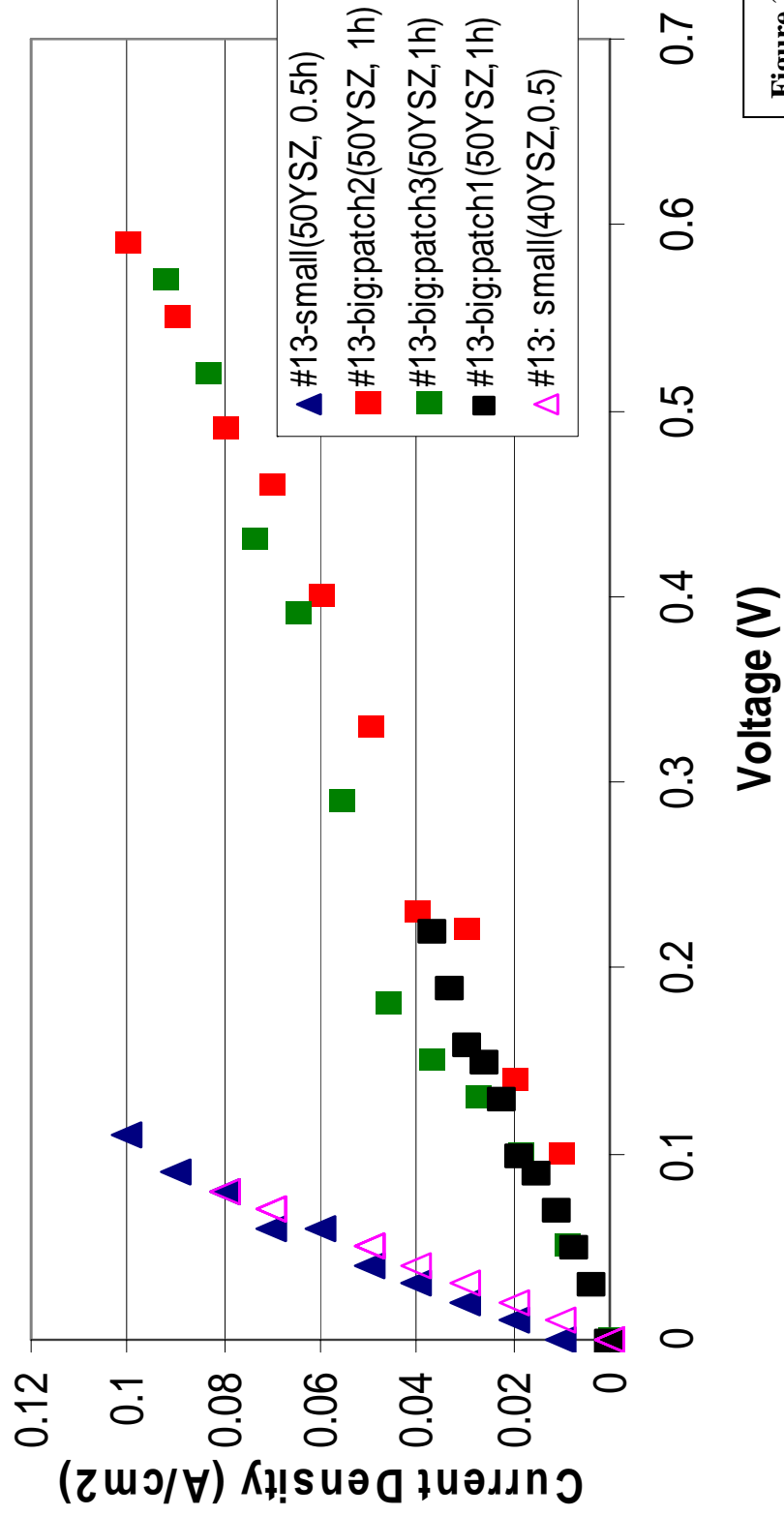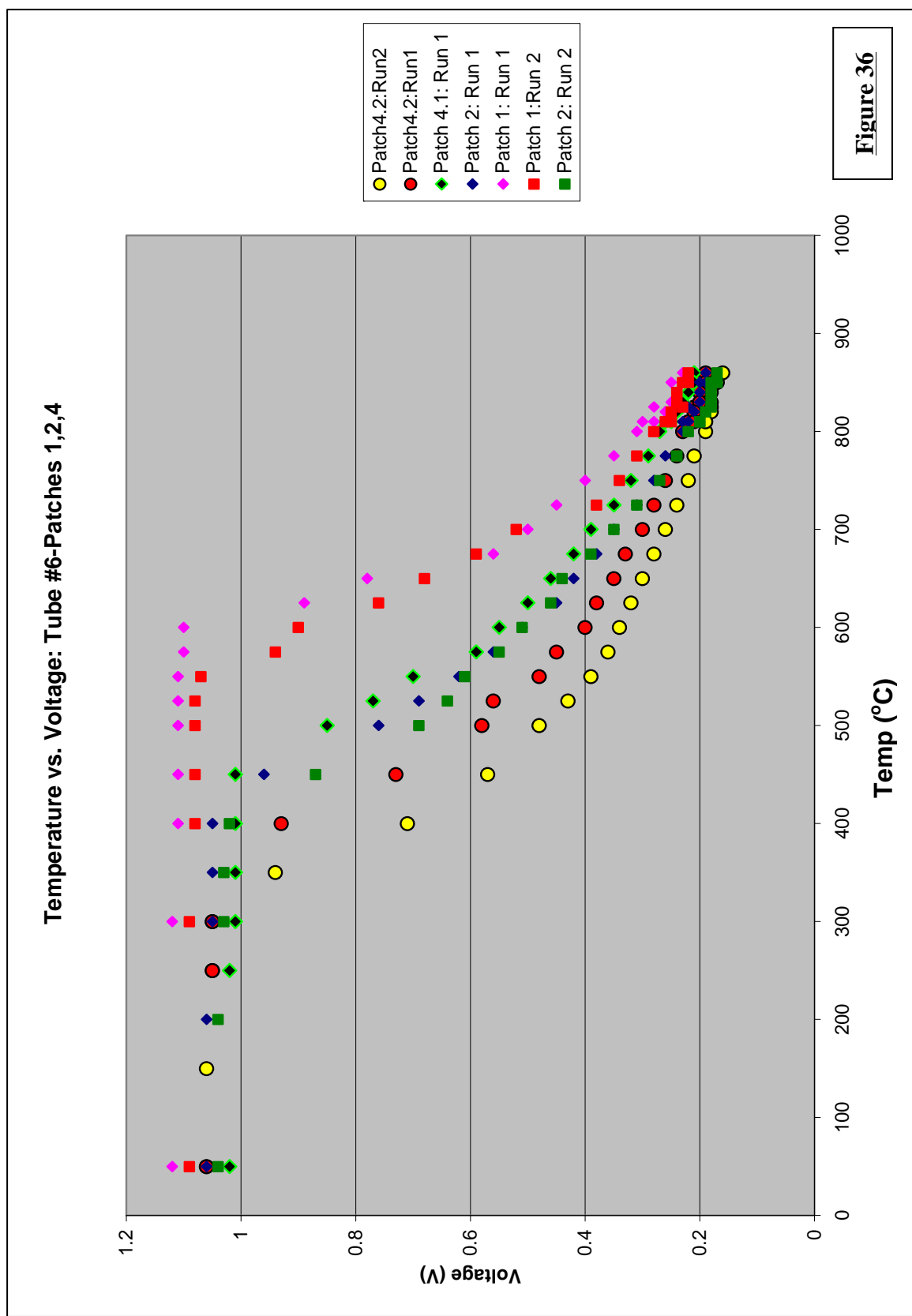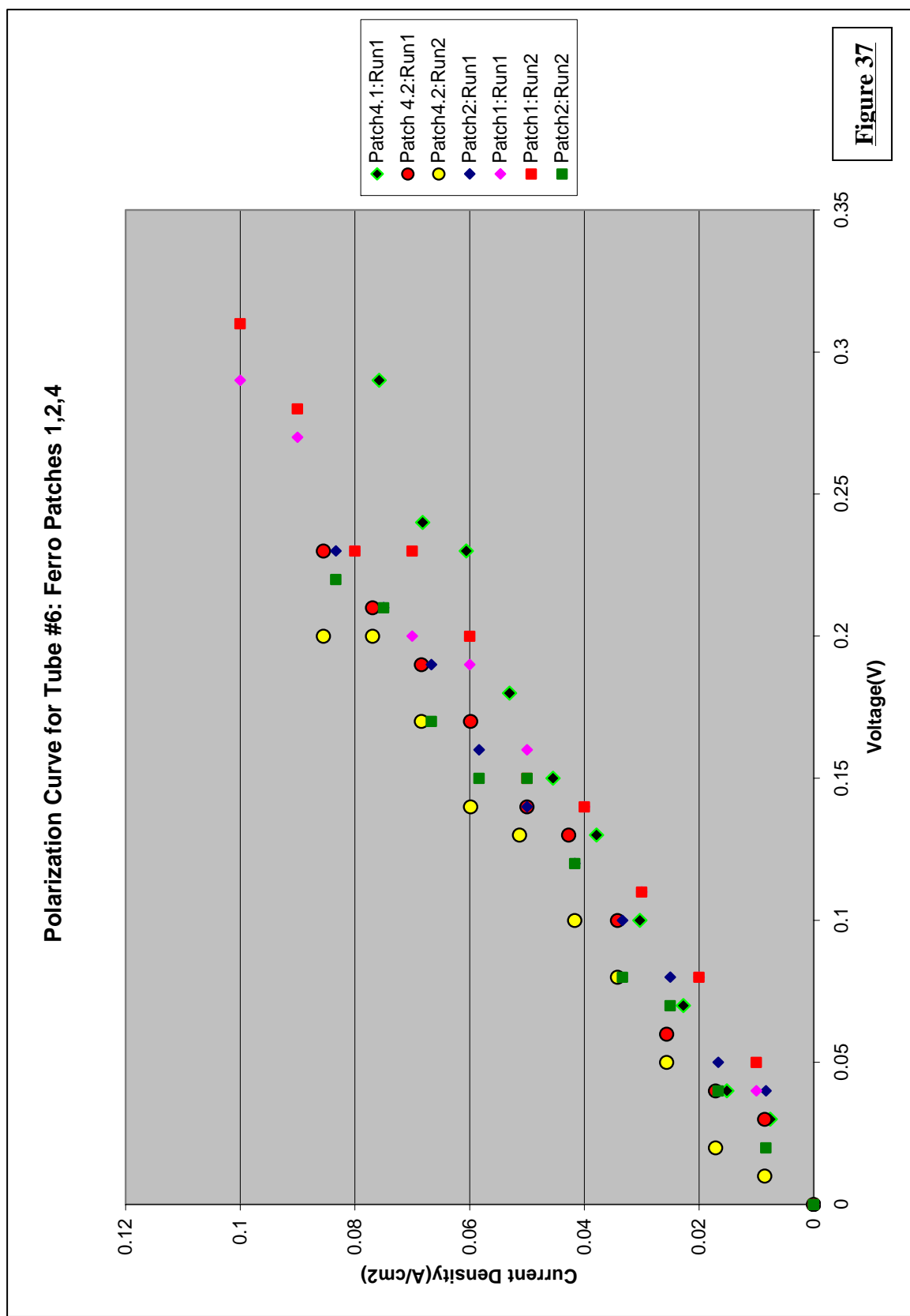
Figure 36

Figure 37

5.2.2.3 Tube 7

Two patches were tested on tube 7. Patch 1 was tested twice and patch 2 only once. Above 700°C patch 2 began to show a drop in voltage, while patch 1 remained at the same voltage until 800°C (Figure 38). At operating temperature, the required voltage of patch 1 was slightly less than 0.9V. Patch 2 performed better with 0.35V.

The polarization curve seen in Figure 39 also shows patch 2 outperforms patch 1. Above 0.2V, the current density in patch 2 increases dramatically over that of patch 1 reaching a plateau of almost 0.07A/cm^2. Patch 1 did not exceed 0.055A/cm^2.

5.2.2.4 Sample 06-30-00

Three patches on 06-30-00 were analyzed. Patches 2 and 3 exhibited similar performance with a required voltage of ~1.09V at low temperatures and 0.21V-0.26V above 850°C (Figure 40). However, patch 1 required only 0.5V at 100°C and rapidly decreased to 0.05V at temperatures higher than 700°C.

The current density reached 0.1A/cm^2 for each patch in sample 06-30-00 (Figure 41). Patch 2 reached this value at 0.23V and patch 3 at 0.33V. Patch 1 yielded 0.1A/cm^2 at a low voltage of 0.05V. This area of the sample exhibited the best performance out of all the sample tests.

5.2.2.5 Sample 09-19-00

There were two areas of interest on sample 09-19-00. One large solid patch of approximately 8cm^2 and one area of 9 interconnected patches of 1cm^2 each were analyzed. These areas yielded almost the same data in both the temperature vs. voltage
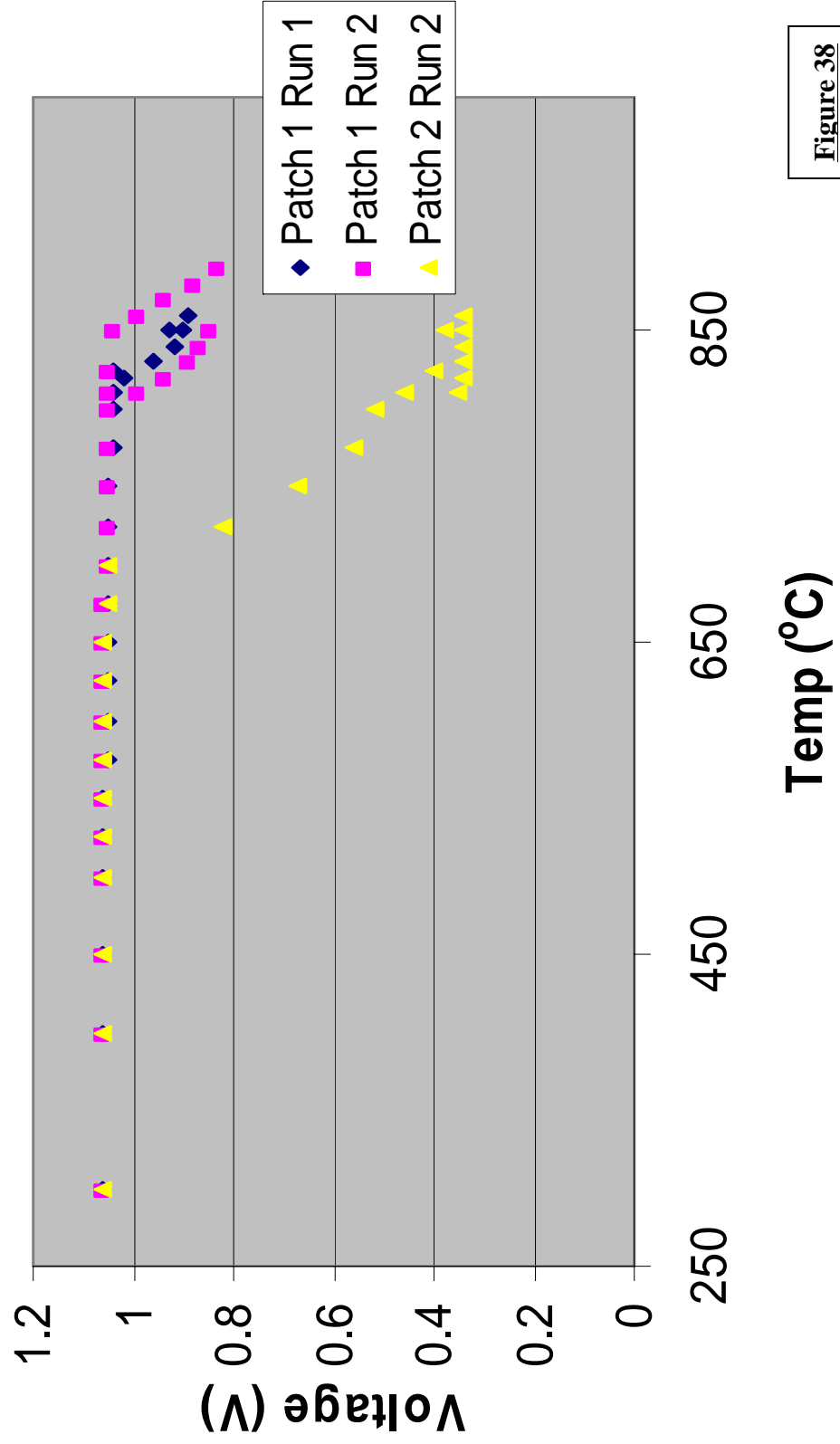
Figure 38

Polarization Curve at 810°C (Tube #7)
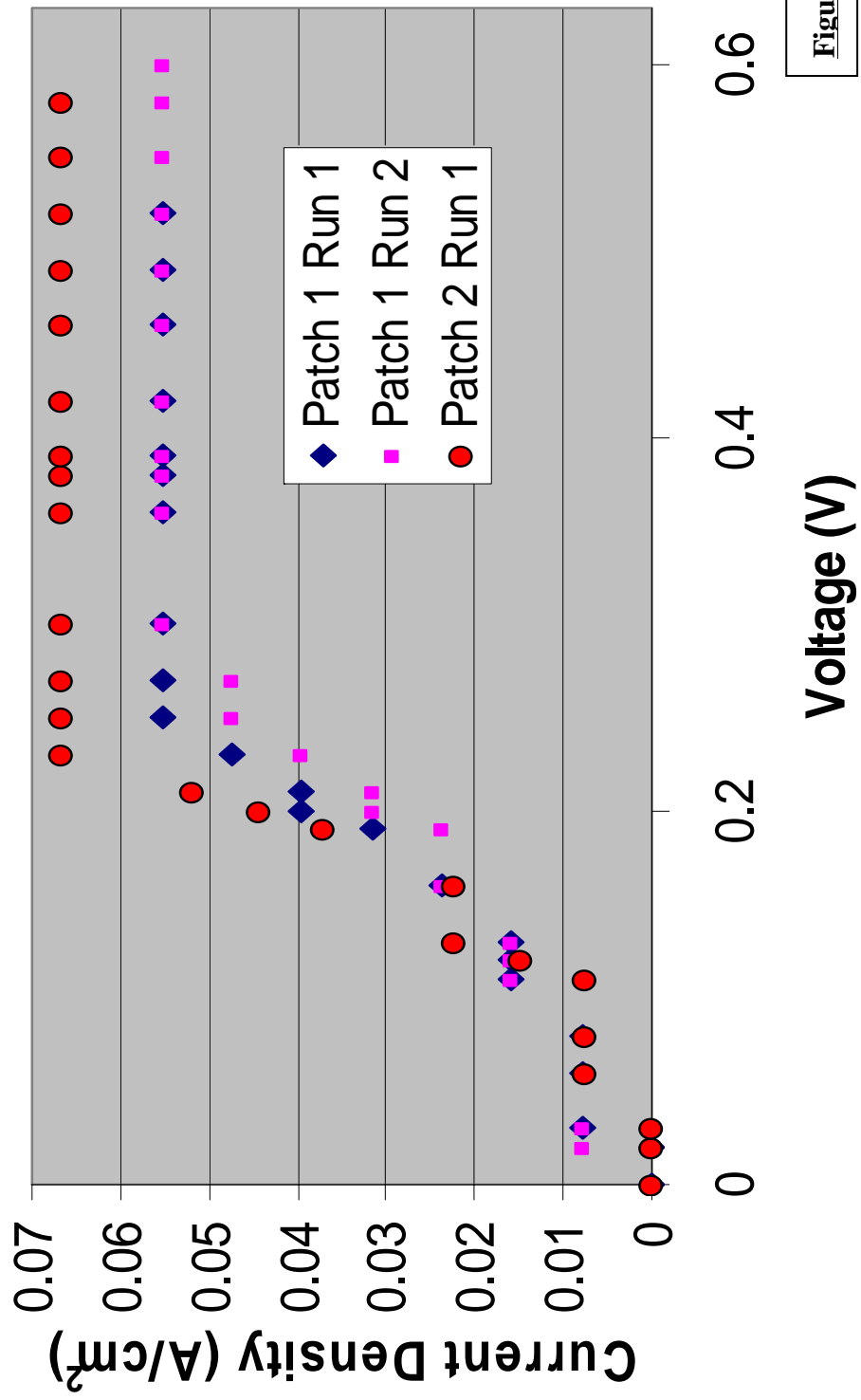
Figure 39
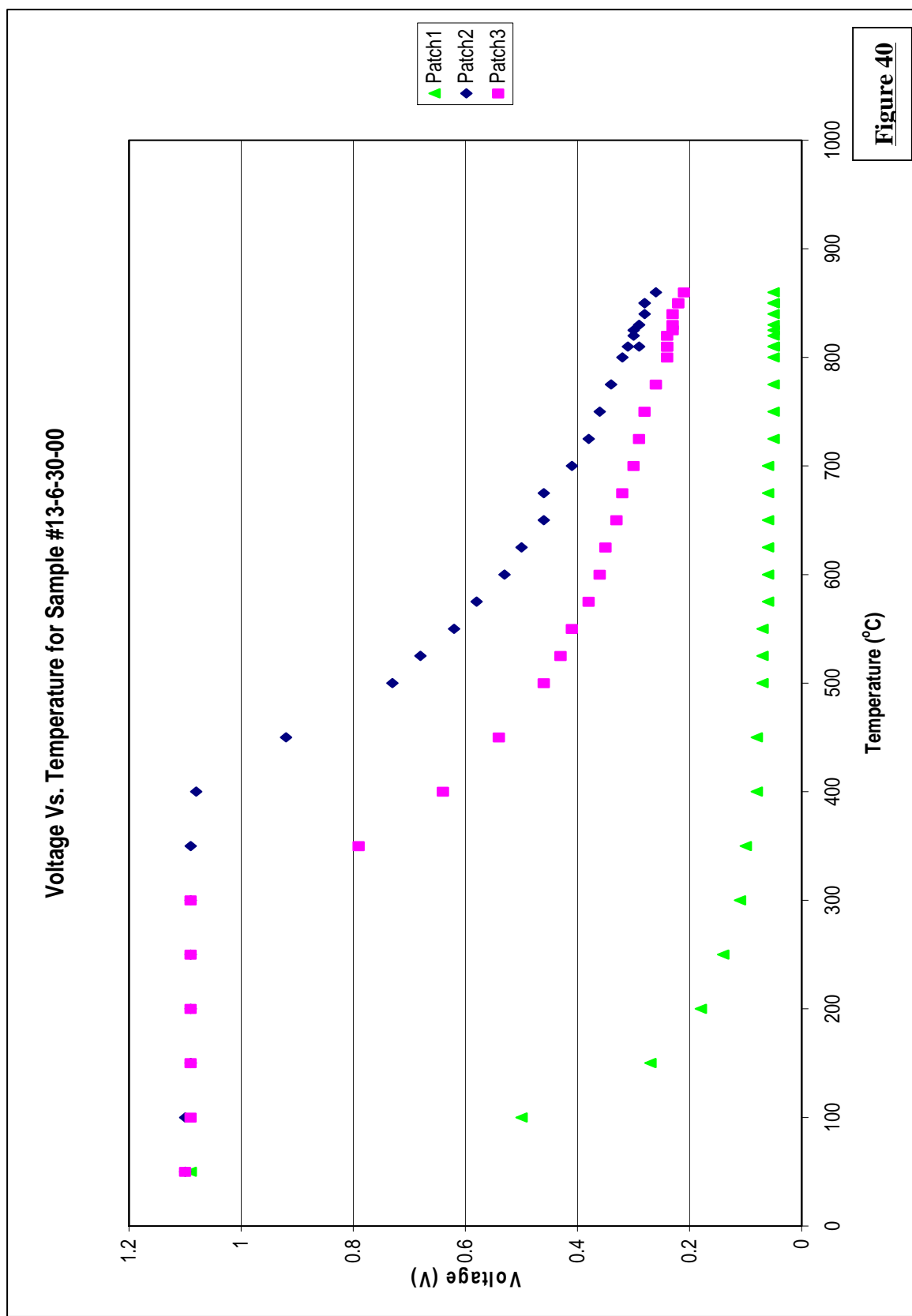
Figure 40

Figure 41
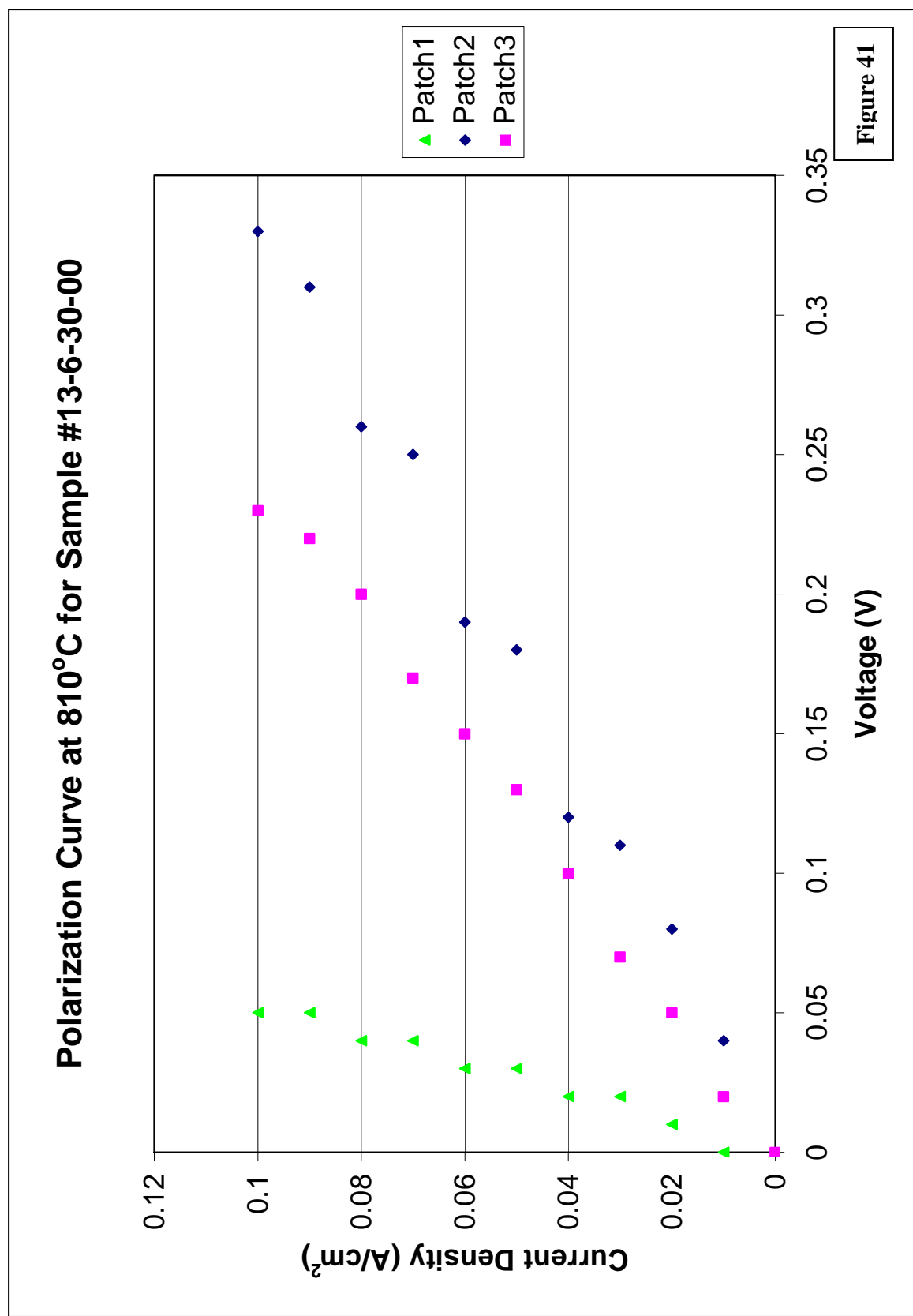
data and the polarization curve. This suggests the membranes of the sample are uniform in structure.

The required voltage of the sample was about 0.5V at operating temperature. This voltage began to decrease at 400°C from the initial measurement of 1.1V (Figure 42). The current density slightly exceeded 0.08A/cm^{2} between 0.4V and the limit of the test, 0.75V (Figure 43).

5.2.2.6 Testing as a Fuel Cell

Due to the timing and availability of H$_2$, only sample 06-30-00 could be tested for energy production. Tube 6 and tube 7 could not be recapped and the Pt leads connected to the anode layer on 09-19-00 had become detached from beneath the final sealant used to seal surface leaks near the end cap.

Two separate runs with the H$_2$ forming gas were done on 06-30-00. During the first test, at 800°C, with no forming gas, the measured voltage was at 0.012V. The gas was introduced into the system at 5PSI and no change in voltage was observed. The PSI was slowly increased and the voltage began to fluctuate at 15PSI but no stable measurement could be made. At 30PSI the voltage increased to 0.348V and remained stable.   The pressure was then increased to 40PSI and 0.353V was measured.   The pressure of the forming gas was not raised above 40PSI during testing.

The second test yielded similar results.   Without forming gas the sample measured 0.14V at 800°C. No stable voltage measurements could be observed until the pressure reached 30PSI. At 30 and 40PSI the voltage measured 0.342V and 0.351V, respectively.
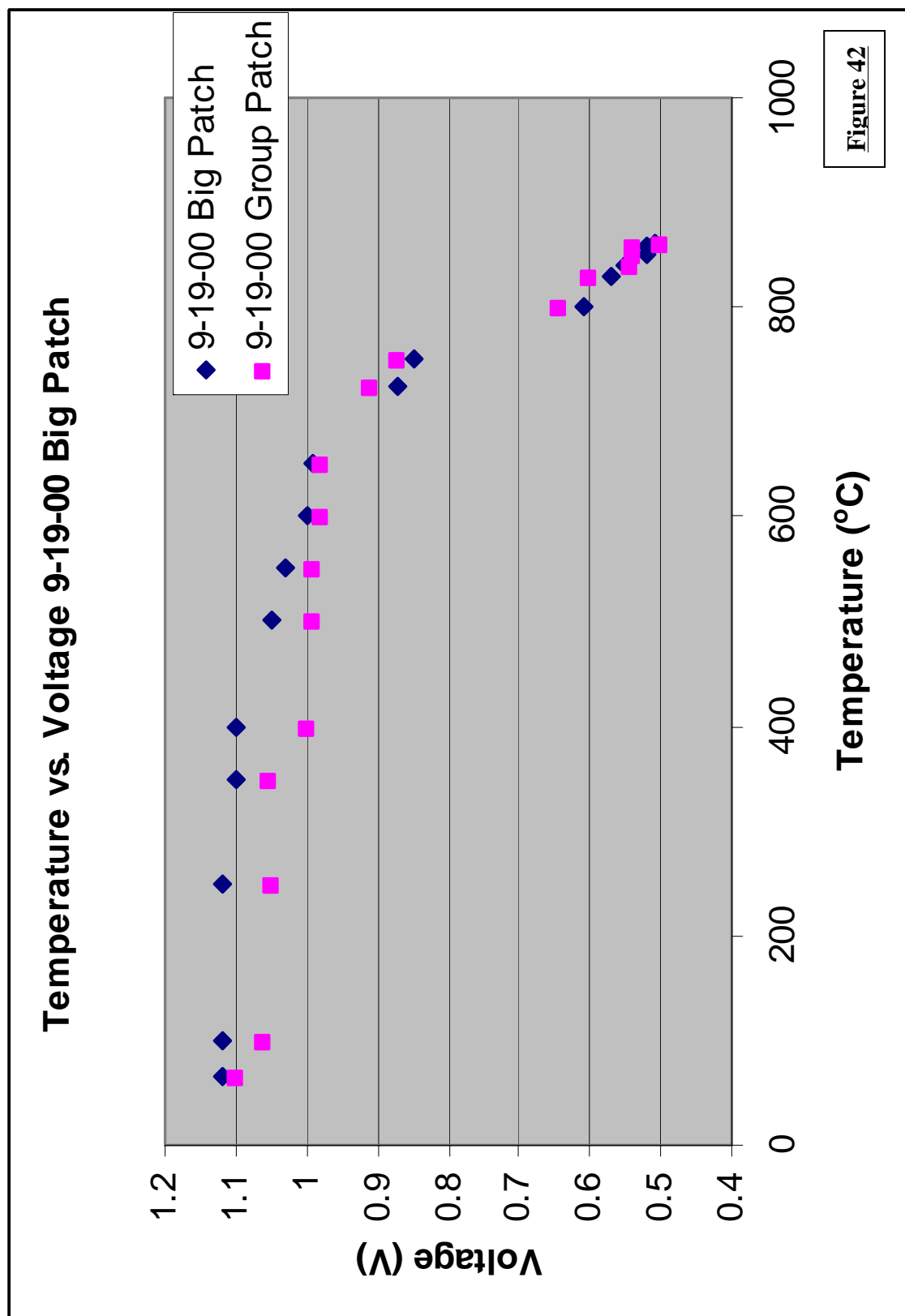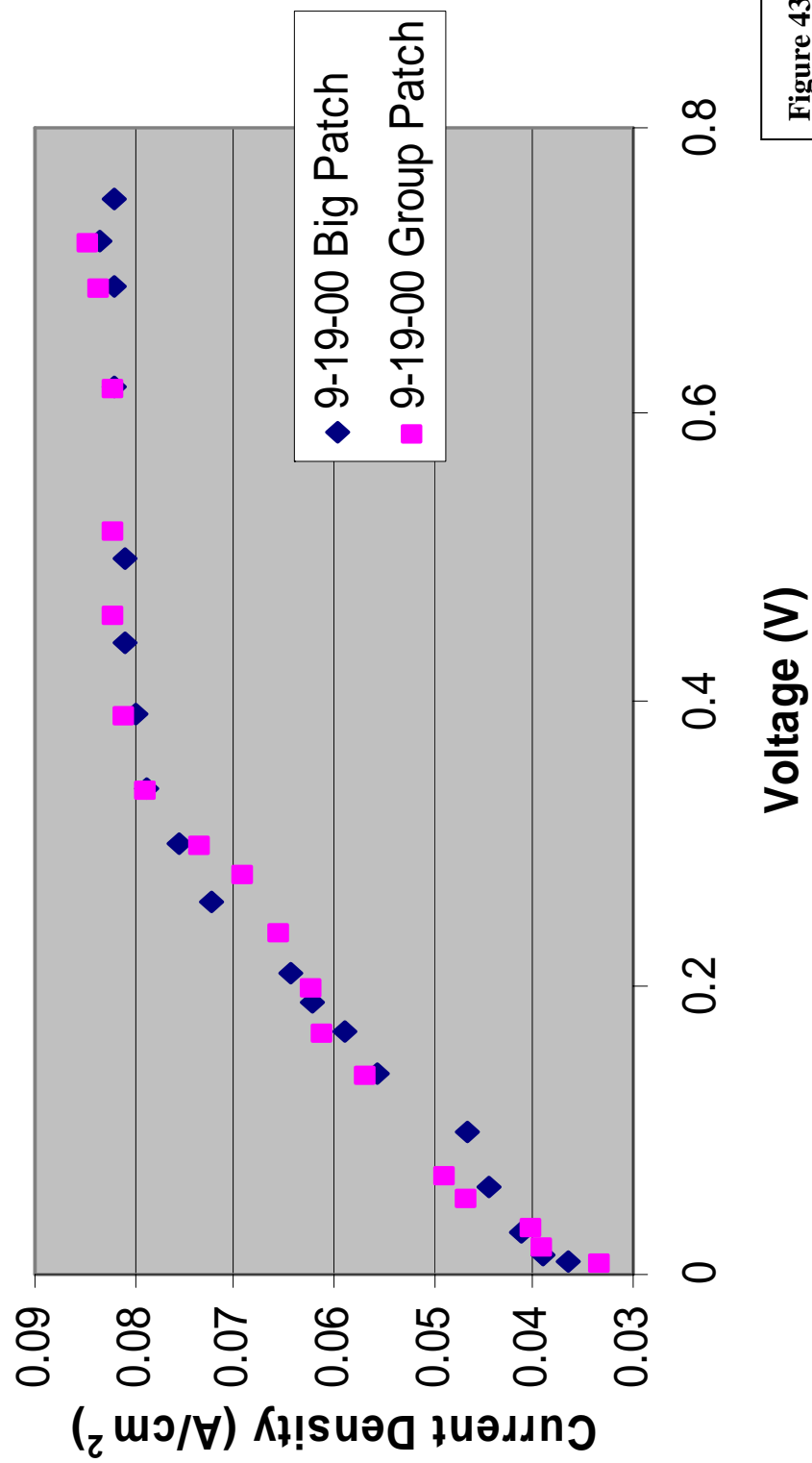
Figure 42

Figure 43

5.2.3 Mechanical Testing

Pressure data was monitored on nine of the samples previously analyzed. All check pieces withstood approximately 1PSI of pressure with the exception of chk-11. The membrane of chk-11 did not leak until 4PSI which was exceptionally high for all samples tested. The #13small samples performed similarly despite the 10 layer difference. #13big and 06-30-00 showed a higher tolerance to pressure than the smaller samples. In particular, the completed sample, 06-30-00, withstood 1.75PSI indicating the ability to hold accumulated gas provided flow is permitted through the extraction straw. Figure 44 refers to the pressure data collected. These are the average pressures measured over five locations on each sample except for 06-30-00. The completed sample had pressure applied through the extraction straw.

5.2.4 Field Emission Scanning Electron Microscopy

Once all electrochemical testing was completed, the samples were fractured, polished, and then dried at 70^oC for 24 hours. Samples were prepared for the FESEM. The working distance was varied to compensate for the wide range of magnifications used for imaging. The accelerating voltage was varied between 5kV and 10kV to either increase or decrease charging effects for better images.

5.2.4.1 #13 Partial Samples

The entire membrane cross sections of #13small(1) and #13big were imaged. The image of #13small(1) is seen in Figure 45. The entire membrane is approximately 250μm from the end of the substrate to the final Pt layer. The active electrolyte layer can

Pressure Data
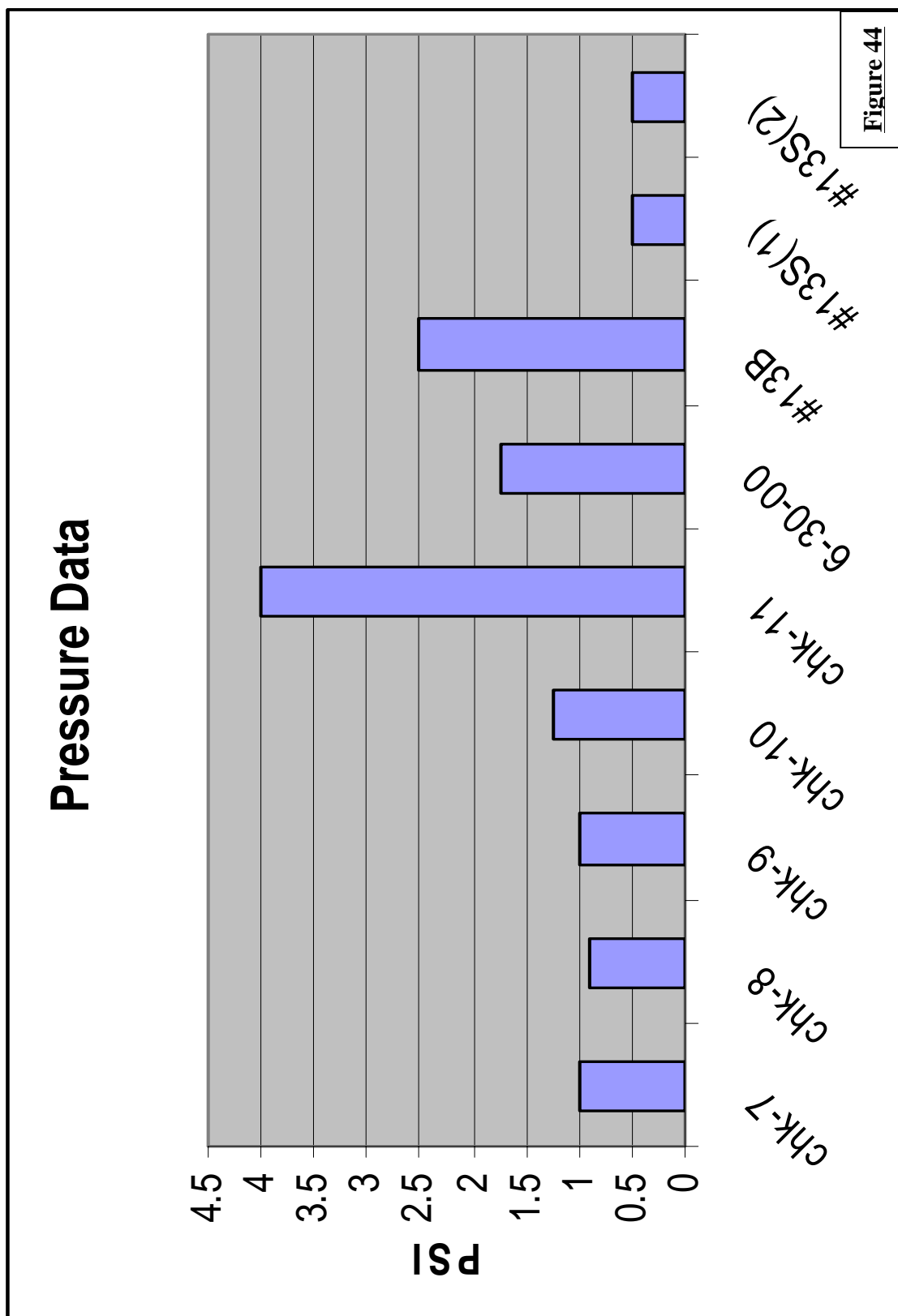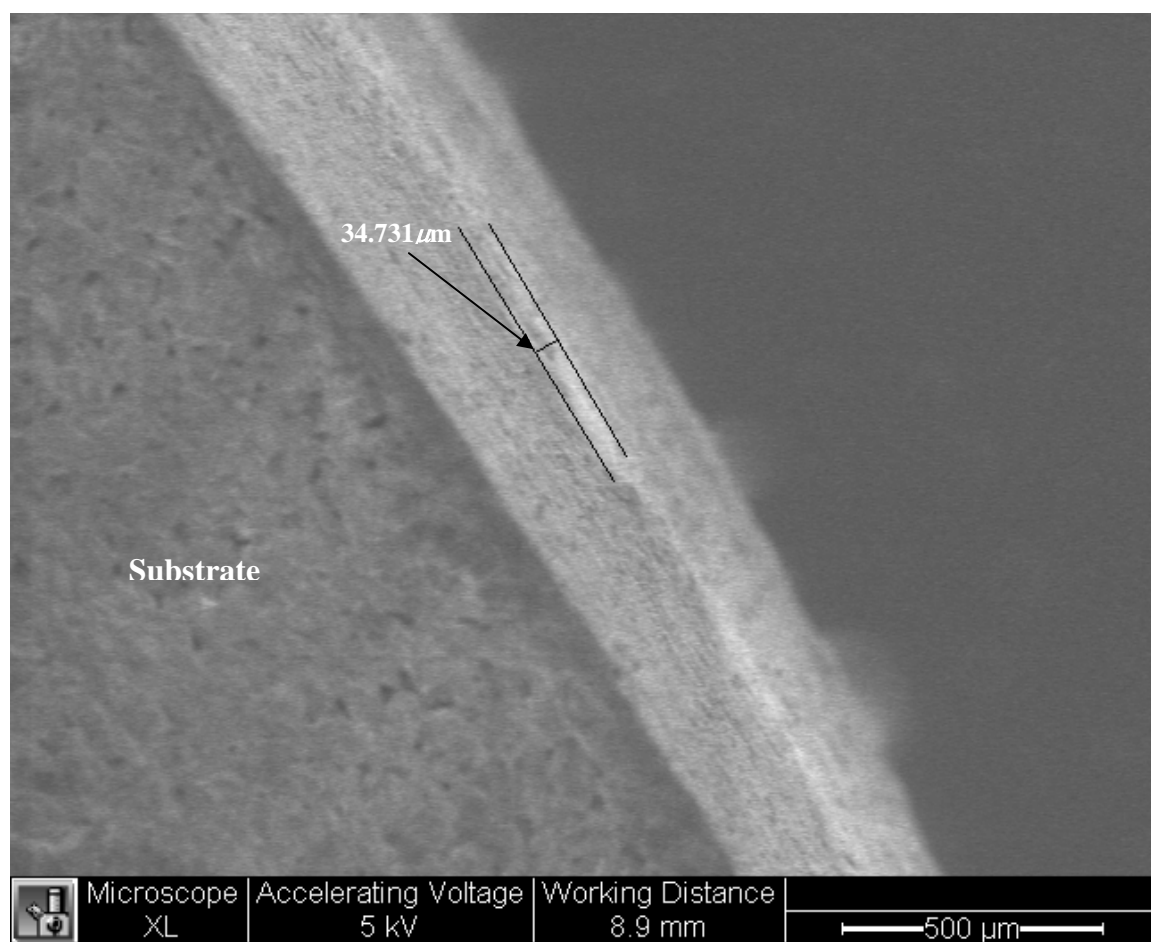
Figure 44

Figure 45: Full membrane of #13small(1). YSZ membrane is highlighted

be seen due to the charging effect. In this image, at the thickest part of the film, the YSZ measures 34.7μm. The YSZ towards the top of the image appears to be thinner and non-uniform. The LSM layers are much thicker than expected, which may be due to the mixing of the electrolyte at the interfaces.

There is no indication of a discreet electrolyte layer in the image obtained from #13big. The entire membrane is ~81μm. No charging was observed that would indicate the non-conductive YSZ layer. The electrodes and electrolyte appear to have mixed promoting an electrical short. The membrane can be seen in Figure 46.

5.2.4.2 Tube 6

Two sections of tube 6 were imaged for comparison (Figure 47 and 48). The entire membrane of tube 6 measured 86.6μm. The YSZ layer is visible but not uniform. The layer is approximately 35μm thick and the dark edges along it appear to indicate where either the electrode has mixed or where polishing has damaged the cross section. It can also be seen in the lower edge of Figure 47 that there is no membrane separation and the LSM has penetrated the entire YSZ layer.

The Pt/LSM/YSZ interface near the substrate of tube 6 is visible in Figure 48 at higher magnification. Each membrane appears to have a sharp boundary and the LSM clearly separates the YSZ from the Pt by ~6.3μm. This boundary thickness fluctuates slightly by ~0.5μm where the sample was imaged. The large grains in the middle are the LSM particles. The material on the left of the image is the base Pt layer on the substrate. The YSZ is visible on the right and has a high brightness due to electronic charging.
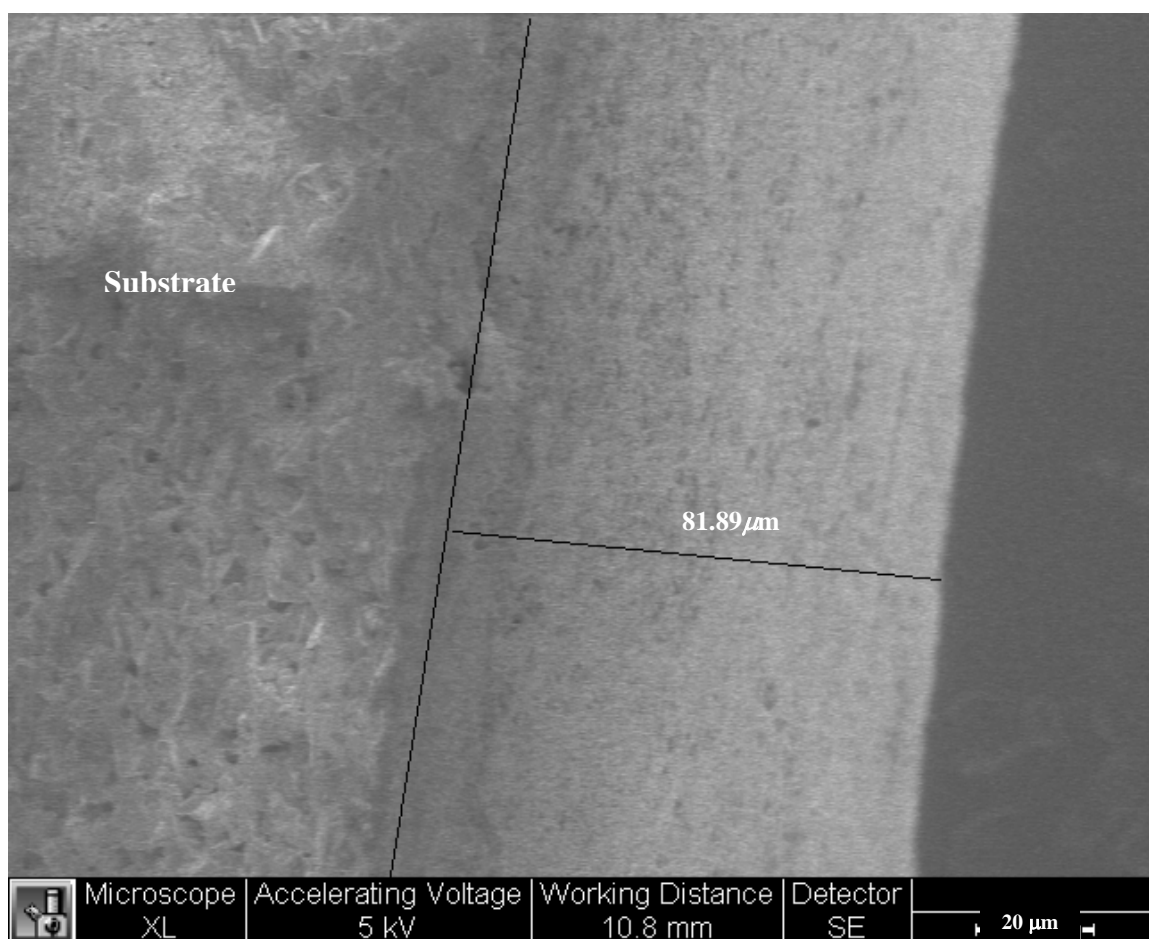
**Figure 46[*]: Substrate and membrane cross section of #13big.
Separate layers are indiscernible**

[*] Scale was miscalculated when imaged. Proper scale is pasted over original image.
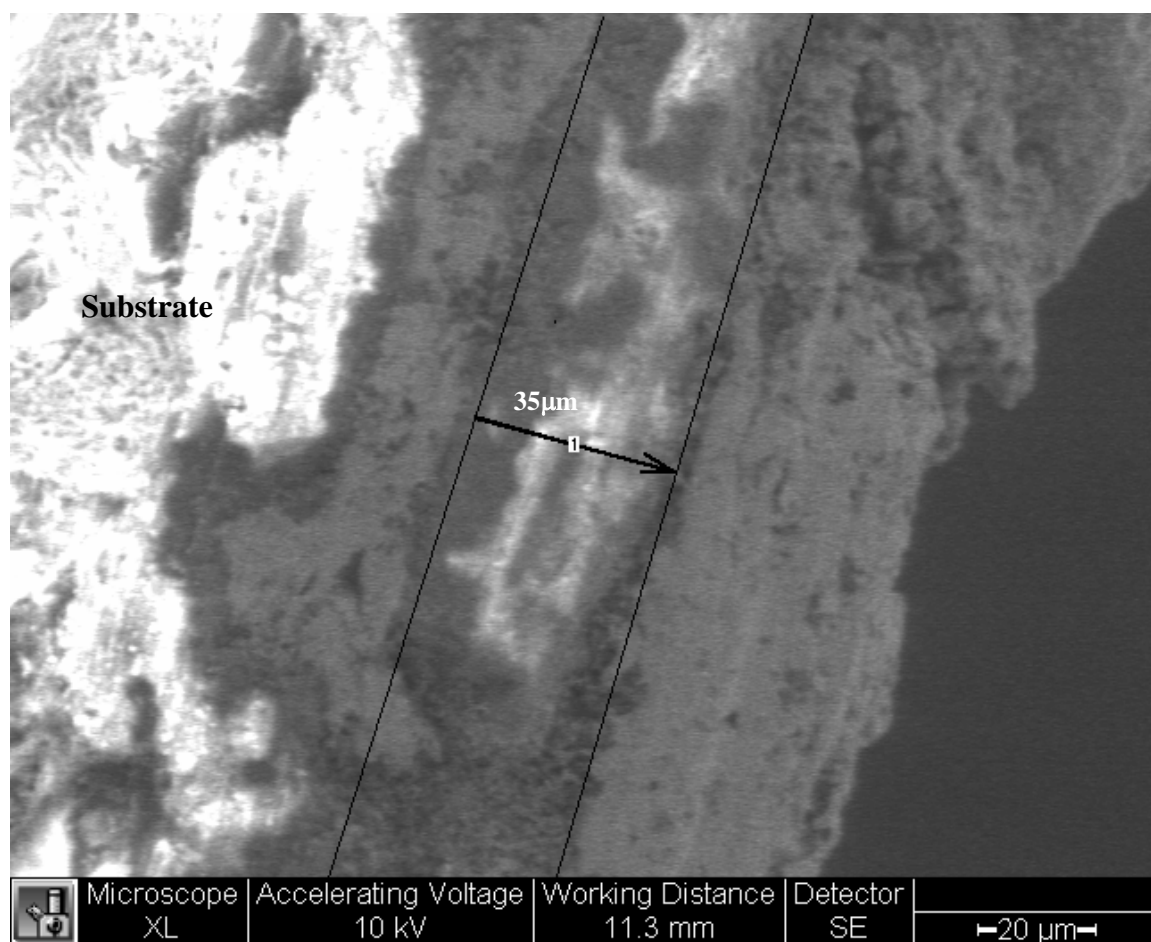
Figure 47: Entire membrane of tube 6. The electrolyte layer is measured at approximately 35μm
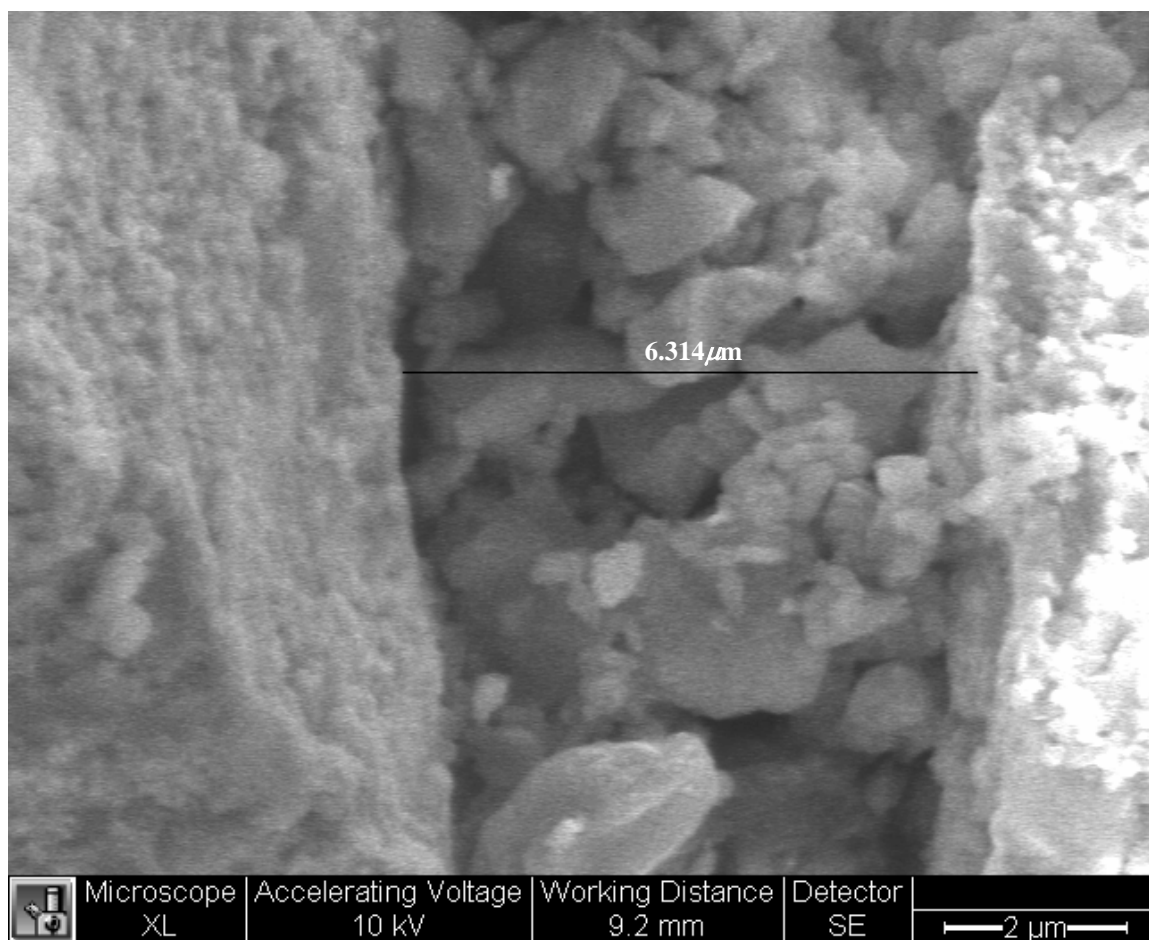
**Figure 48: The LSM membrane separates the Pt(left) and
YSZ(right) on tube 6**

There was evidence of a triple phase boundary found on tube 6. This boundary is continuous throughout the areas were the electrolyte sufficiently separates the electrodes. Figure 49, at higher magnification, shows charging on the left side, which is mostly YSZ, decreasing towards the conductive LSM layer on the right side of the image. The thickness of the layer was between 2.6 and 3.5μm.

5.2.4.3 Tube 7

The electrolyte layer of tube 7 was more variable than tube 6. The thickness varied and the interfaces between the electrodes varied. Figure 50 shows a full cross section. The thickness ranged between 30μm and 50μm, as indicated by the extent of charging in the image. Polishing striations can be seen along the electrolyte layer where the grain size is smaller and the membrane is denser as compared to the electrode layers.

Figure 51 clearly shows Pt and the more porous LSM electrode on the YSZ layer. It was along this area of the sample where both a triple phase boundary and a sharp interface were observed. The image in Figure 52 at higher magnification shows an area where no TPB is present. For comparison, Figure 53 shows the absence of the TPB in the lower half of the image and a TPB that is ~3.5μm thick at the top of the image. Where there is a TPB, the image shows an area of charging next to the electrode layer. While the triple phase boundary is not uniform, it exists throughout this cross section of the sample.
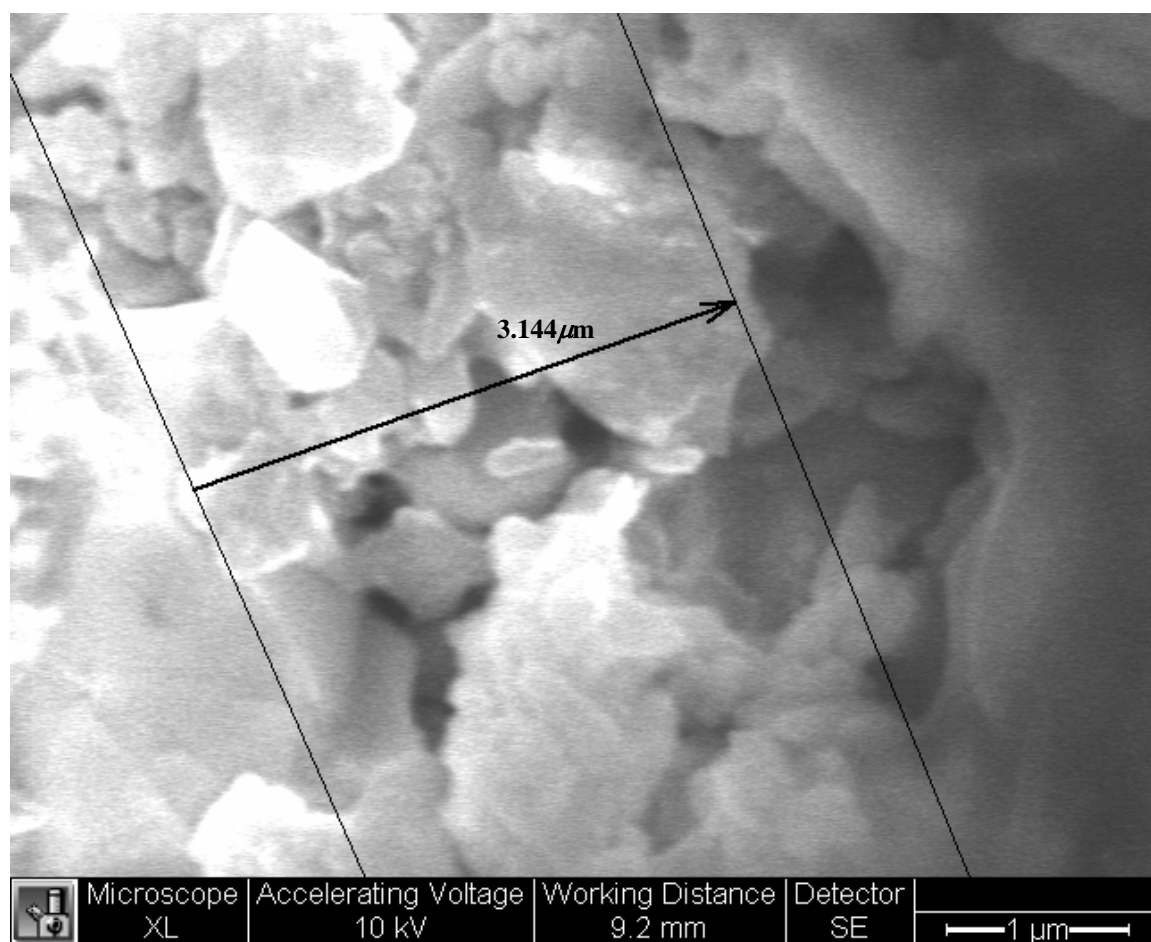
Figure 49: Triple phase boundary present in tube 6
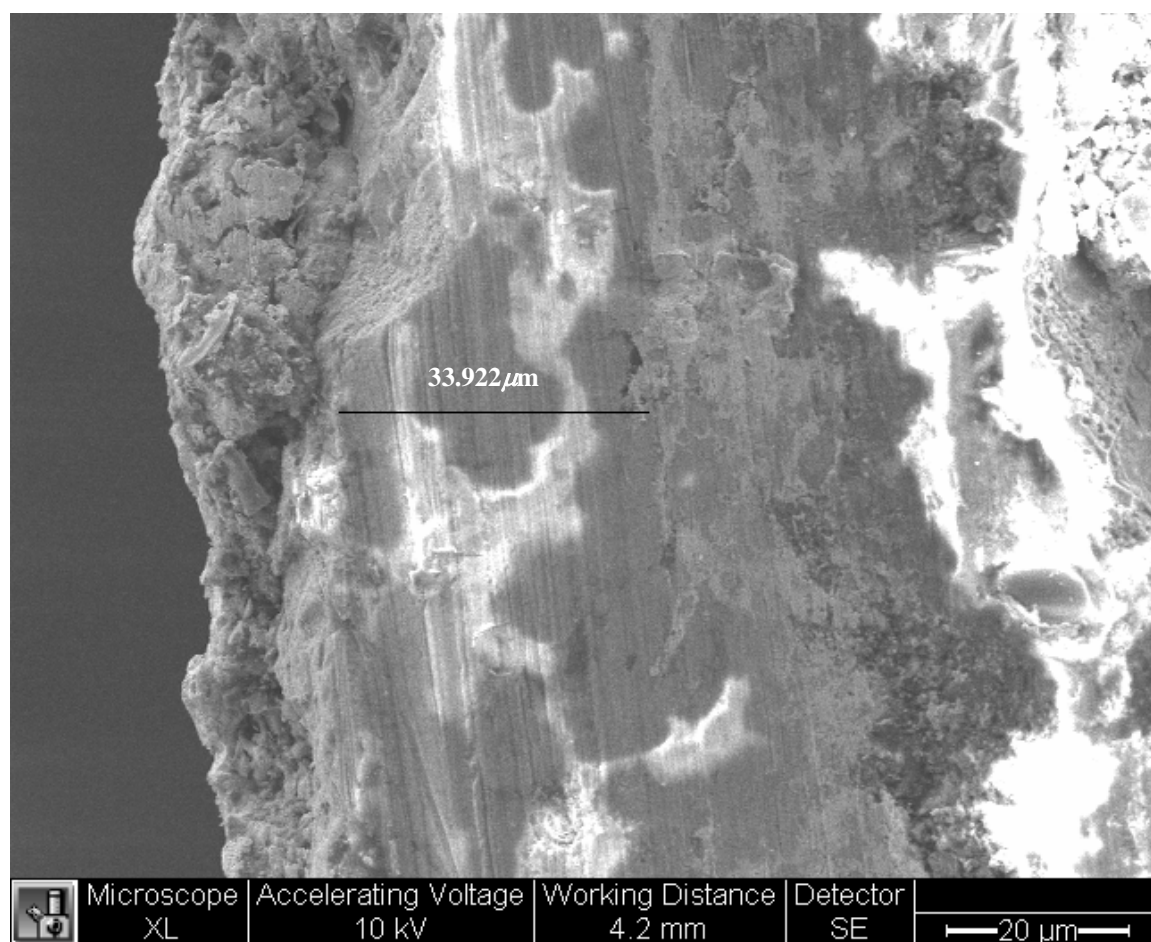
Figure 50: Cross section of tube 7

Pt-8.85μm

LSM-15.57μm

Microscope	Accelerating Voltage	Working Distance	Detector	
XL	10 kV	5.5 mm	SE	20 μm
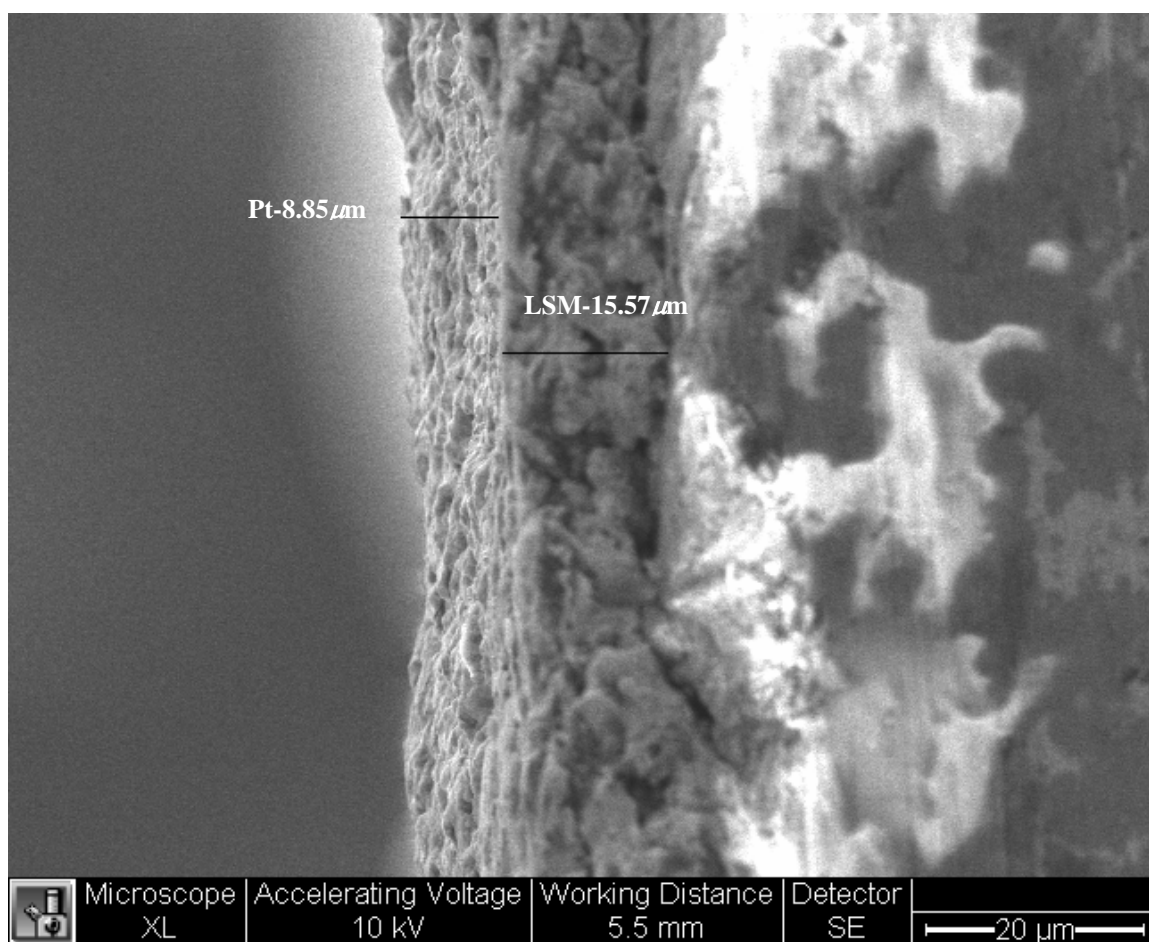
Figure 51: Cross section of tube 7 highlighting the Pt and porous LSM layer. YSZ is charging (right)

	Microscope	Accelerating Voltage	Working Distance	Detector	
	XL	10 kV	5.3 mm	SE	2 µm
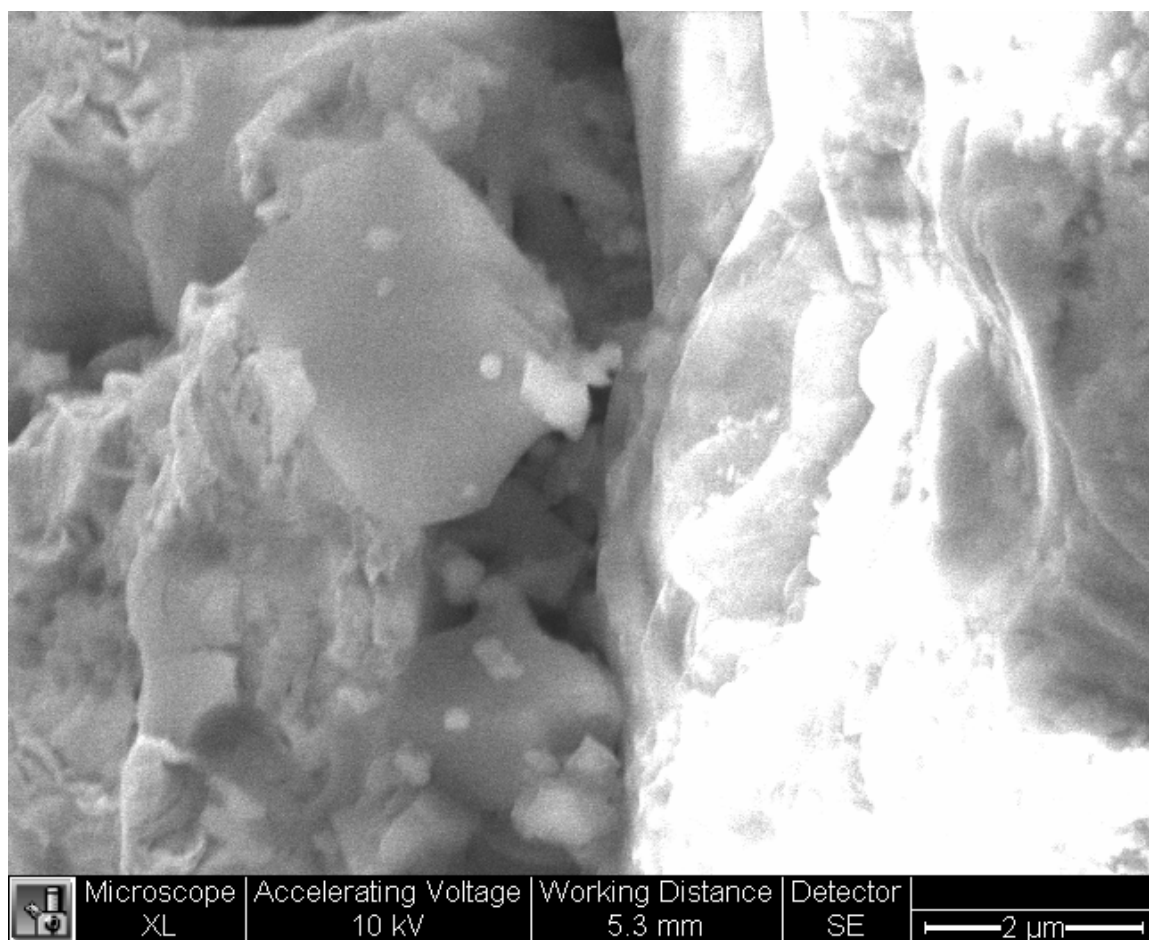
Figure 52: Abrupt YSZ/LSM interface of tube 7. No triple phase boundary

Microscope	Accelerating Voltage	Working Distance	Detector	
XL	10 kV	4.2 mm	SE	⊢━2 μm━⊣
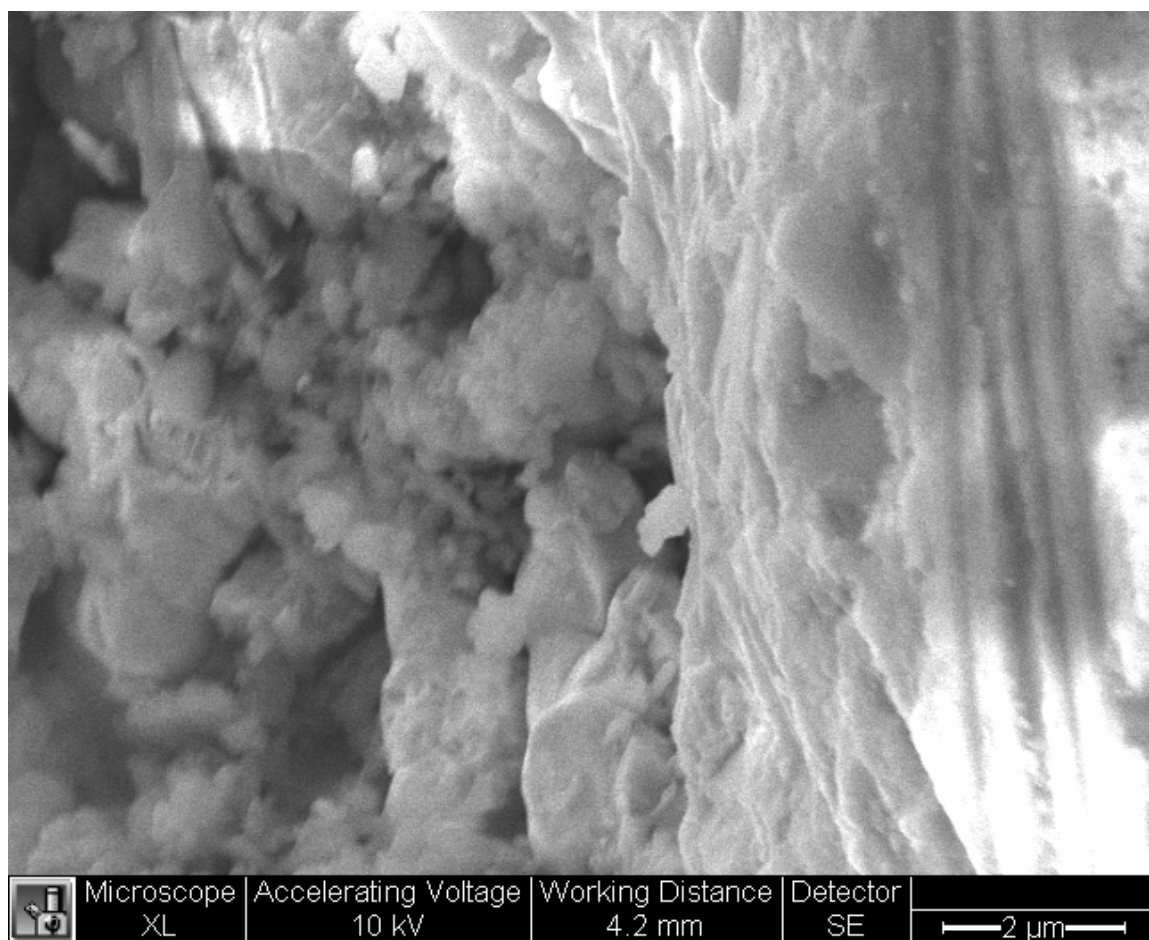
**Figure 53: TPB of tube 7 seen along the top of the image
and the abrupt interface below**

5.2.4.4 Sample 06-30-00

The imaged areas of 06-30-00 are similar to those in tube 7. It is difficult to identify the electrolyte layer. No area of charging is observed in the membrane that would correspond to YSZ. Figure 54 shows the approximate region of the LSM anode layer that is 45μm thick. The alumina substrate is the only surface charging in the image. Below the LSM area the structure changes and looks to be a mixture of LSM/YSZ. Damage during polishing makes it difficult to say.

5.2.4.5 Sample 09-19-00

At low magnification Figure 55 shows the Pt layer, anode layer, and triple phase boundary of the sample. The electrolyte layer does not exhibit a charging effect in this area. Once again, the YSZ can be identified by the difference in the membrane structure. The LSM anode measures between 50-70μm and there is a small amount of charging that helps identify the TPB which is ~45μm.

In Figure 56, a triple phase boundary can be seen but it is difficult to measure. Poor polishing in some areas of the sample left the surface uneven when mounted. The measured TPB is approximately 11μm but this may be an underestimate because surface is sloping down towards the electrolyte. This is indicated by the change in focus.

Overall, 09-19-00 has a fairly well structured YSZ membrane throughout the sample areas that were imaged. The layer varied from 60μm up to 140μm due to the extra layers applied. The electrolyte layer did not charge in areas where there was mixing with LSM. At low magnification, a small strip of the YSZ area can be seen clearly due to charging (Figure 57).

LSM-45μm

Microscope	Accelerating Voltage	Working Distance	Detector	
XL	10 kV	3.4 mm	SE	⊢50 μm⊣

Figure 54: LSM anode of 06-30-00
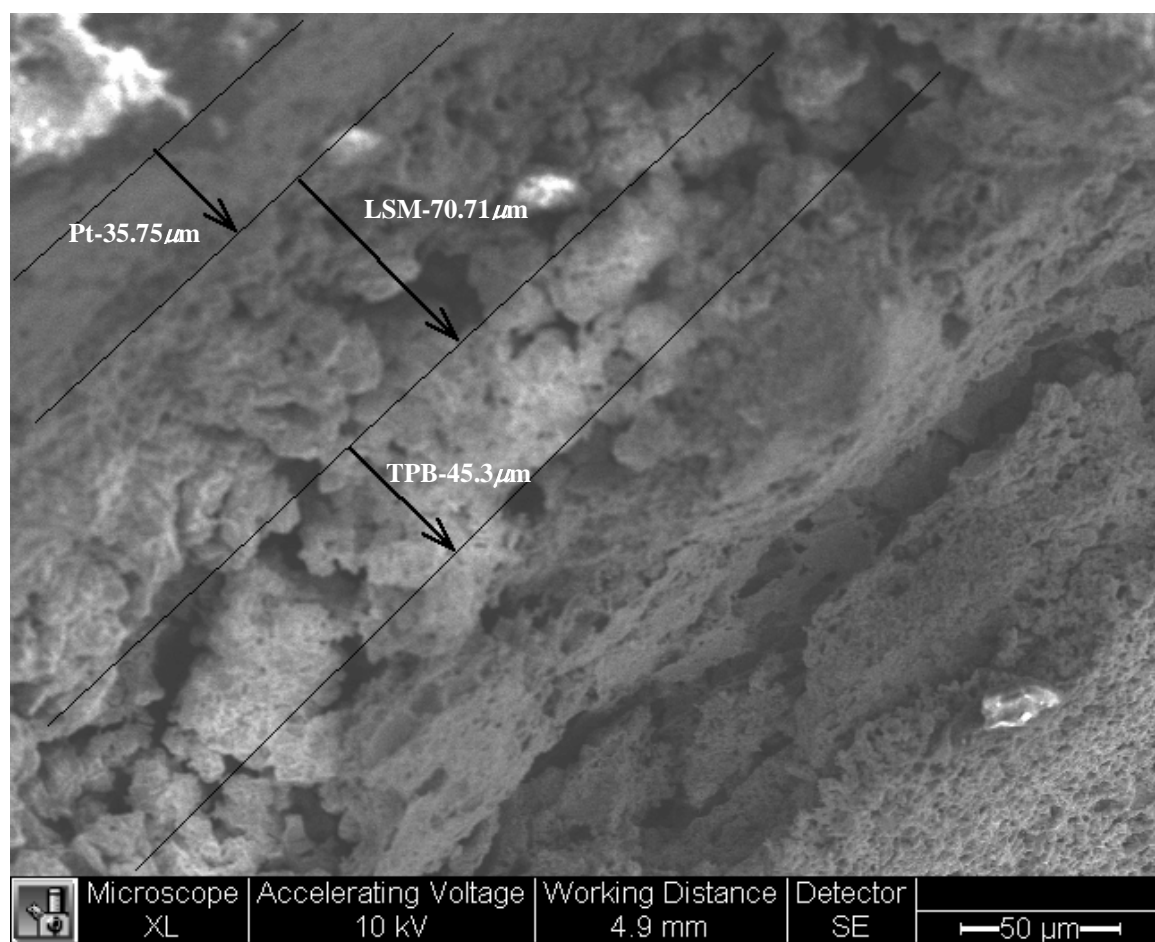
**Figure 55: The Pt, LSM anode, and TPB measurements
of sample 09-19-00**
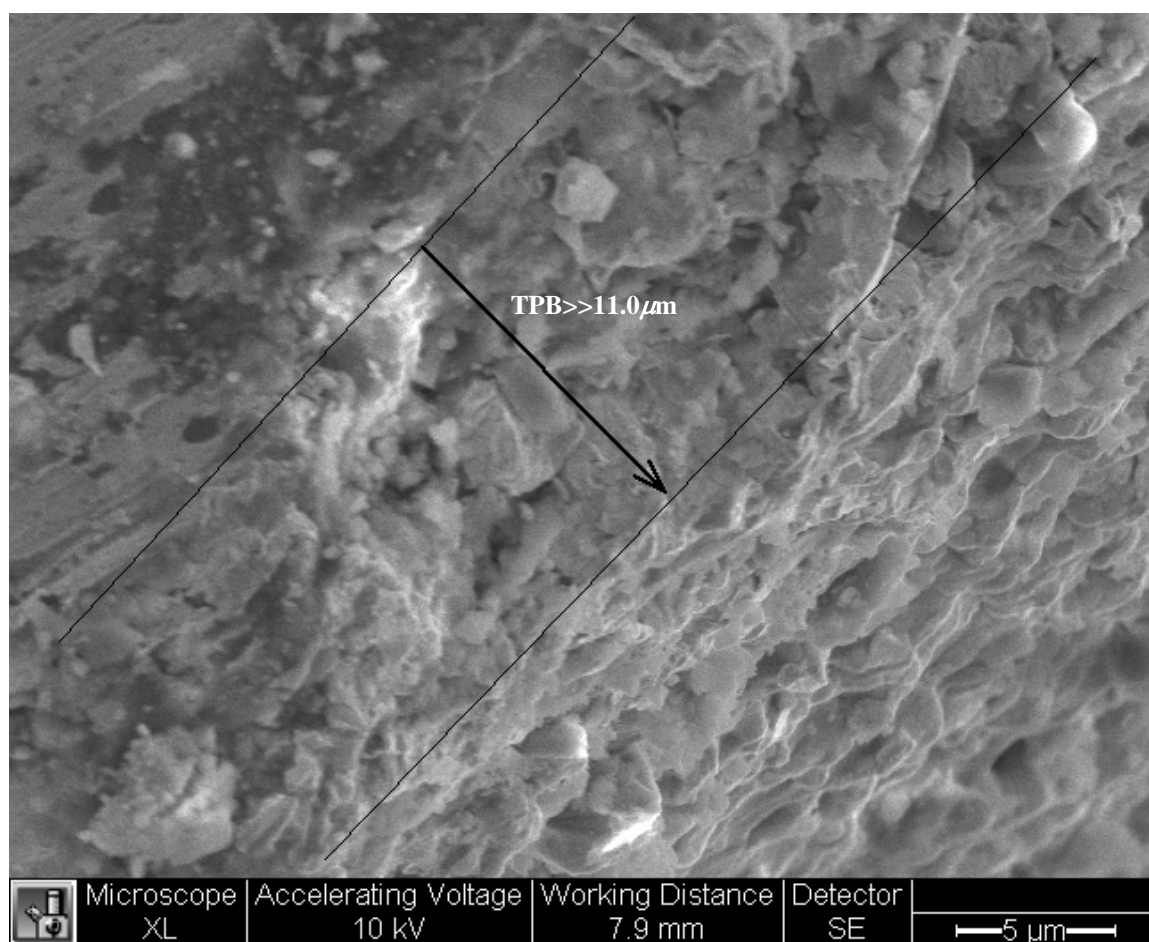
Figure 56: Triple phase boundary of sample 09-19-00

Microscope	Accelerating Voltage	Working Distance	Detector	
XL	10 kV	8 mm	SE	⊢—50 μm—⊣
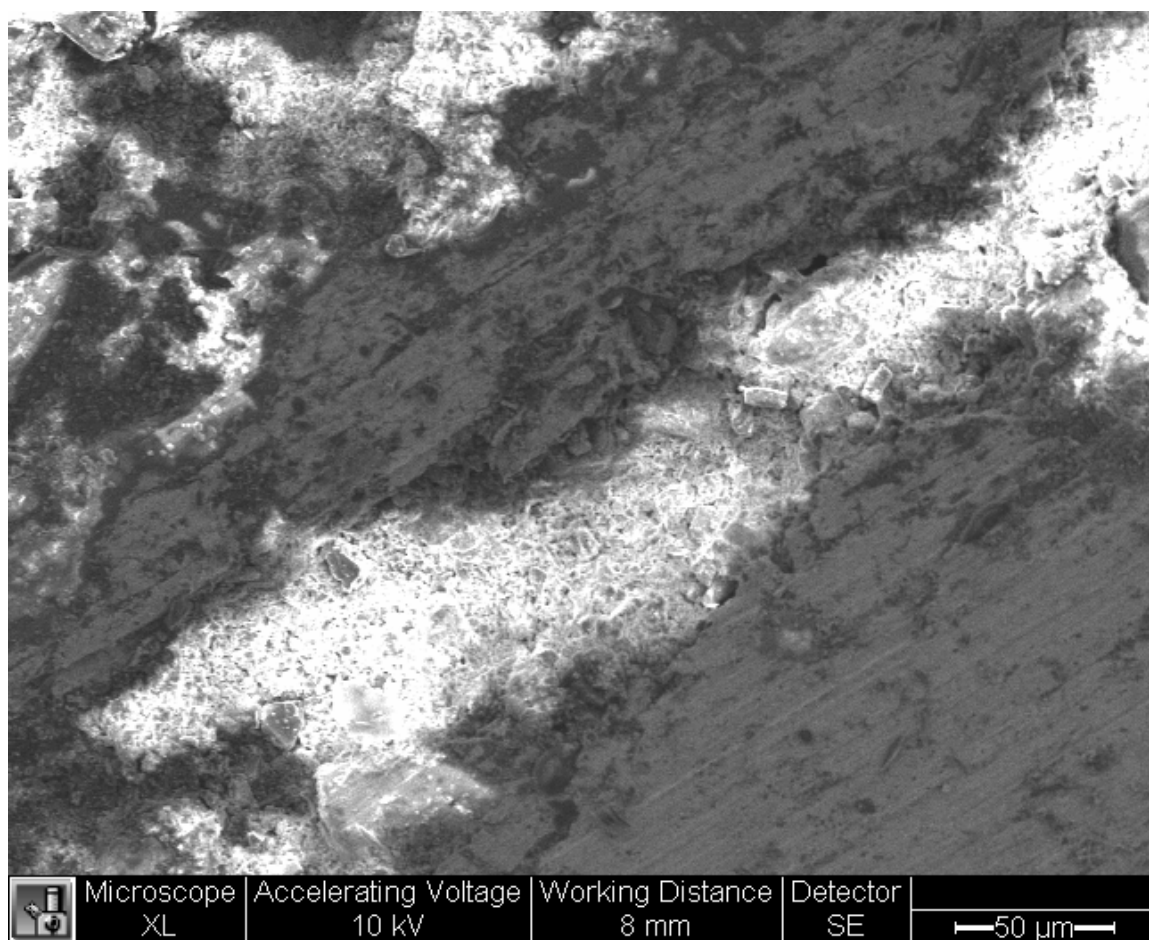
Figure 57: YSZ electrolyte of sample 09-19-00

6.0 DISCUSSION

Based on the results, it was found that weight gain was the best indication that the components of the device were in place. Using weight gain as the basis for comparison, the electrochemical data could be interpreted to show that the YSZ layer was indeed acting as an oxygen electrolyte. The microscopic analysis showed the importance of the triple phase boundary in achieving proper electrochemical performance.

6.1 Weight Gain

Full samples with an active surface area of ~94.2cm^2 showed less weight gain per cm^2 than the half samples or fragments. Sample 09-19-00 gained less weight in the first 50 layers than most of the check pieces that had only half of the surface area. Sample 06-30-00 gained approximately the same weight as most of the check pieces within 50 layers. This result is attributed to sample positioning during sintering. Check pieces are half samples with the cross section side as the support. The membrane is facing up during firing. The full samples stand on the open end with the dome pointing up. Orientation in the furnace appears to influence the weight gain per layer in most cases. After sintering, a ring of YSZ dust surrounds the base of the sample when a whole tube is fired. This is not seen when firing check pieces and any excess YSZ that has not adhered to the surface is minimal.

6.1.1 Effect of Viscosity on Weight Gain

The addition of ethylene glycol significantly raised the viscosity (η) of the YSZ solution. However, a higher viscosity solution produced little effect on weight gain. Chk-11(EG) and chk-8(EG) both gained weight and at approximately the same rate as many of the non-EG samples within the first 50 layers as seen in section 5.1.4. There were some instances of large gains followed by large losses in all samples. This cyclic trend was not unique to the EG samples. While some samples received as many as 130 layers chk-7, 8, and 9 only have 64 YSZ layers. The total weight gain of all check pieces is compared up to 64 layers in Figure 58. It is apparent that the rate at which a sample gains weight is not dependent on the viscosity of the solution. Although the non-EG samples, chk-9 and chk-10 gained weight rapidly, both chk-12(EG) and chk-13(non-EG) did not show the same behavior. These two extremes indicate that the rate of weight gain under with the same solutions is not well controlled. Other factors, such as humidity in the laboratory or the brushing technique of the person applying the layers may be important.

This is seen for the full samples as well, when comparing 06-30-00 and 09-19-00, both of which were non-EG. Sample 06-30-00 gained more than three times the amount of weight as sample 09-19-00 in its 50 layers, similar to the weight gained in chk-9 and chk-10. This leads to the conclusion that performance should be related to the measure of weight gain and not the number of layers.

Total Weight Gain after 64 Layers (g)
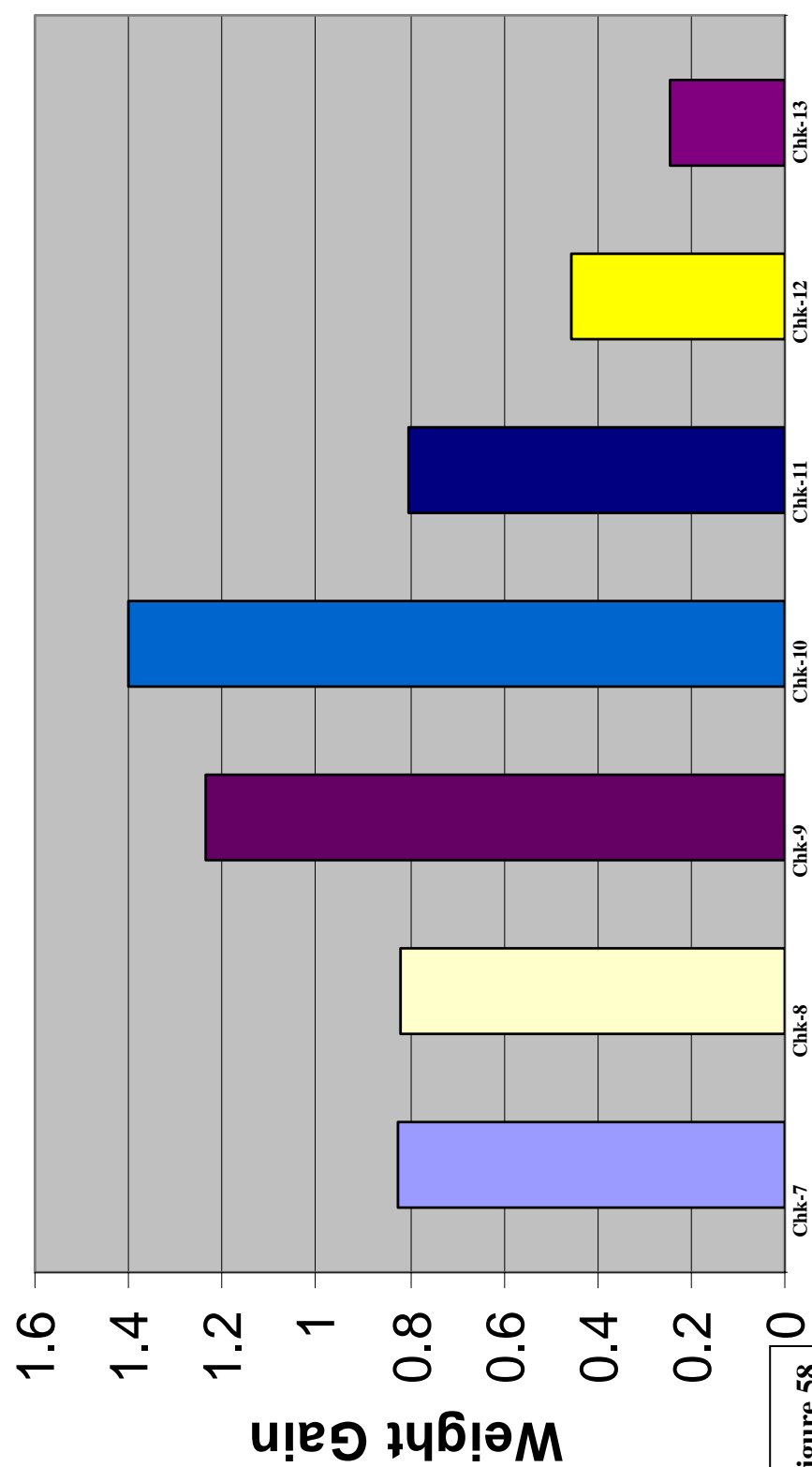
Figure 58

6.1.2 Effect of Application Method

Figure 31 in section 5.2.1.2 compares the weight gain of two check pieces and two full samples dip coated and brush coated. Chk-4(dip) had large weight changes at every measurement. Only one weight change was less than 0.1g. The first 12 layers showed the most weight gained on the sample and that the weight consistently increased up to layer 12 and then became erratic. While the total on chk-4 reached 0.36g, chk-3(brush) gained just over 0.1g in the same number of layers, but chk-3 had some small weight losses and showed an overall increasing trend.

The same behavior can be seen in the full samples although the weight changes are less drastic on 11-01-00(dip) than the dipped check piece. Again, this is attributed to the sample positioning during sintering. Sample 10-30-00(brush) consistently gained weight as chk-3 did.

It should also be noted that when coating two samples from the same solution using the brush and dip method the solution must be replenished twice as often as when using two samples with only the brush method. Dip coating applies an even but much thicker layer of solution to the surface of the sample. This also accounts for the large weight gains on the dipped samples. However, the large weight losses suggest that the layers are not developing properly when sintered. The densification process may only occur where the YSZ particles of the unfired coating are contacting a previously fired YSZ layer. Therefore, with a thicker coating, the layer is less dense and structurally unstable. There is a lot of YSZ waste when implementing the dip coating method.

6.1.3 Other Weight Phenomenon

It is apparent in most of the data collected that the average sample weight gain after approximately 40 layers of electrolyte decreases dramatically. In many cases the gains were smaller and the losses increased. The average weight gain of the check pieces are analyzed in Figure 59. The left reference for each sample represents the average weight gain every 4 layers for the first half of the YSZ layering process. The reference bar on the right is for the second half of layering. Full samples are not represented in Figure 59. Full samples did behave similarly except for 09-19-00 and 11-01-00. Both of these samples showed poor weight gain during the first 40 layers and then gained exceptionally well thereafter. Because of the orientation of the sample in the furnace, it appears that establishing the YSZ layer is more difficult in the vertical orientation than it is on the horizontal half tubes or fragments.

6.2 Electrochemical Stability

The electrochemical tests showed that the electrode and electrolyte layers exhibited the desired performance. Most of the V vs. T data collected for samples with 50 layers of the electrolyte produced the required voltage of approximately 0.2V to maintain a current of 300mA at operating temperature.

Tube 7 is the only sample with 50 layers that did not reach 0.2V. Two patches were tested. Patch 2 had the lower voltage at 0.34V and patch 1 averaged ~0.85V in order to reach 300mA. This indicates that the electrolyte membrane may be too thick in these areas, or there is a poor LSM/YSZ interface. A voltage of 0.34V indicates a thicker

Weight Gain during First and Second Half of Layering Process (g)

Figure 59
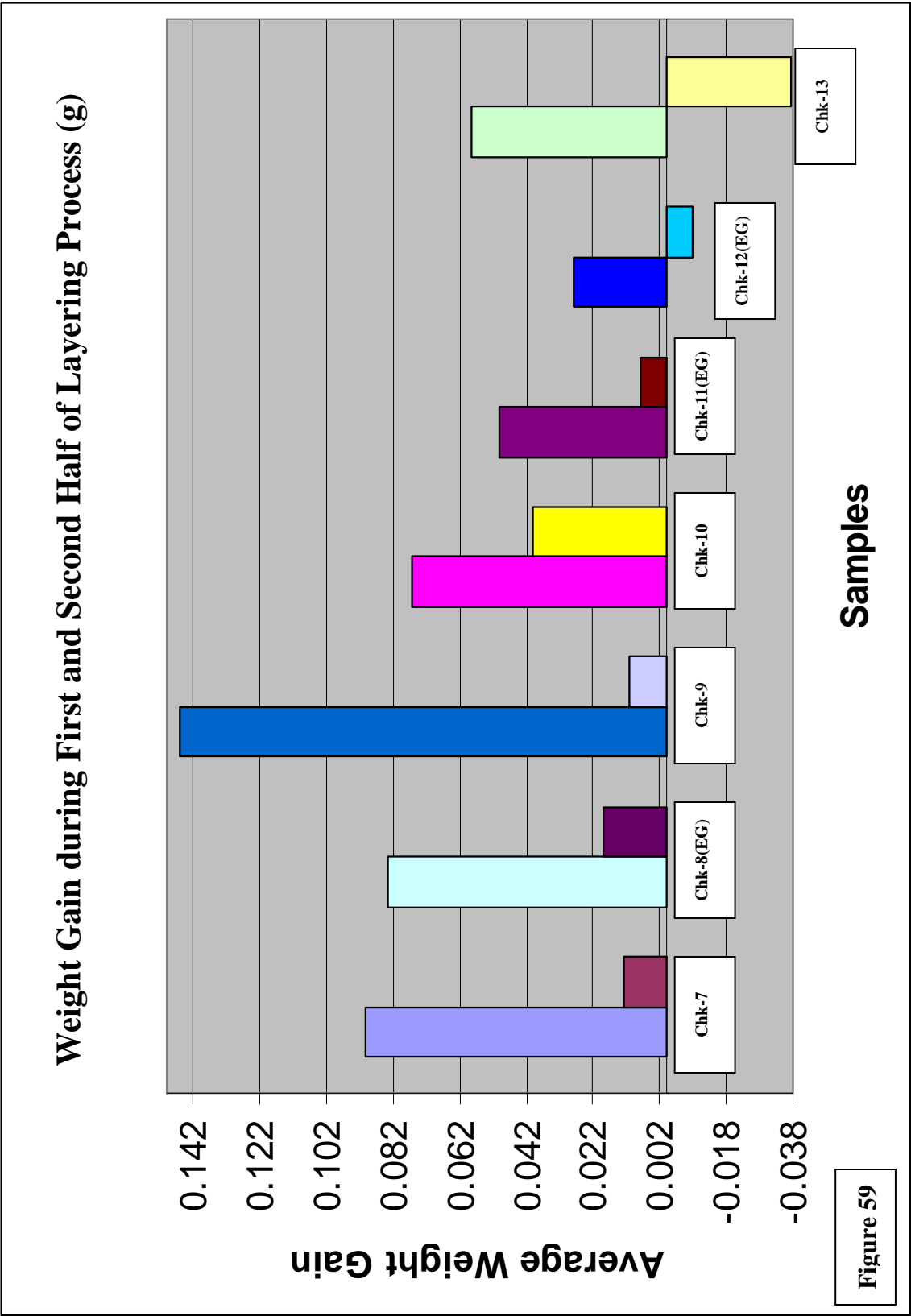
membrane. This is seen in 09-19-00 which required 0.5V after 96 YSZ layers to reach 300mA. The high voltage 0.85V observed at patch 1 suggests either poor membrane/interface development or possibly impurities causing resistance in that area. The voltage is too high for the amount of YSZ applied.

The polarization data confirm the behavior observed in the voltage-temperature curves except for the data for #13big. This sample differed slightly from the performance observed in the other samples. All samples reached a current density of approximately $0.1A/cm^2$ by 0.3V, except for sample 09-19-00 (as expected) and tube 7. However, #13big did not reach $0.1A/cm^2$ until 0.6V.

The data for 09-19-00 confirms that the resistance increases as the width of the membrane increases as seen in other investigations [135]. Figure 60 displays the loss of power density vs. membrane thickness. From the weight and electrochemical data, 1.5-2.0g can often be obtained within 50 layers and is a sufficient weight gain on full samples. This will provide a YSZ layer suitable for membrane separation. A thicker membrane increases resistance in the system.

Previous investigations have yielded comparable results [136]. An investigation based on a supported NiO/YSZ anode, YSZ electrolyte, and an LSM cathode was done using atmospheric plasma spraying (APS). The 8mol% YSZ electrolyte was applied to a thickness of 25μm in one sample and 35μm in all other samples. The cathode layer was the only membrane formed without APS. Table 5 lists the variations in processing and materials used in the investigation. Table 6 contains the voltage and current density data obtained during electrochemical testing. All samples were tested between 790°C and 840°C and had a required voltage of ~0.9V-1V to maintain a current of 500mA. The sol-
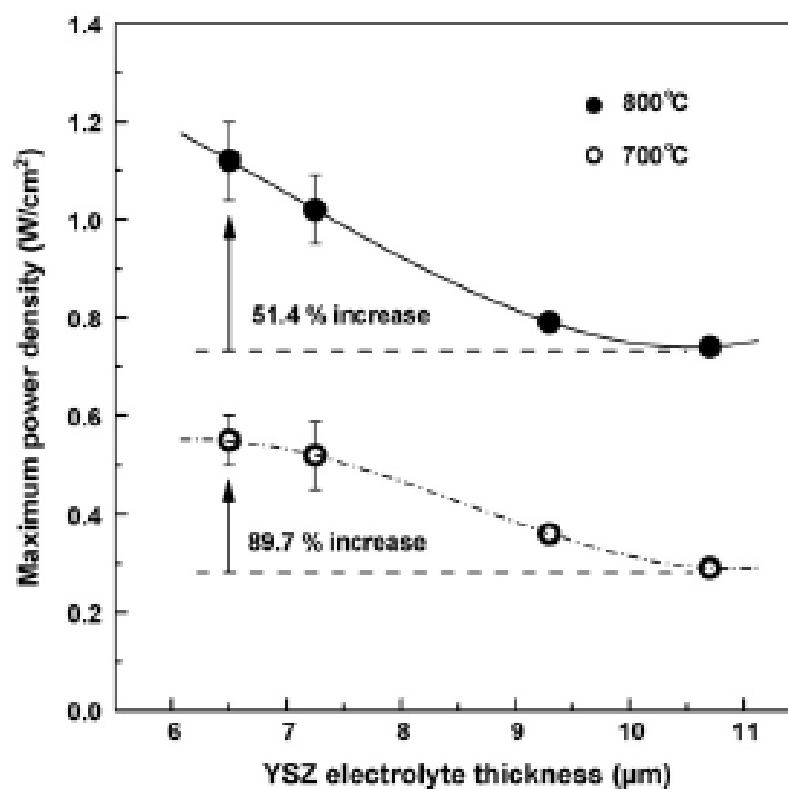
Figure 60: Power density vs. electrolyte thickness in previous investigation [135].

**Table 5: Various membrane processing techniques used in vestigations
by Vassen, et al [136].**

Sample #	Anode	Electrolyte	Cathode(All LSM)
1	Spray Dried NiO/YSZ	Spray Dried YSZ	Brush Coating
2	Spray Dried NiO/YSZ (10μm thinner)	Spray Dried YSZ (reduced APS spraying distance)	Screen Printing(SP)
3	Fused and Crushed NiO/YSZ	Same as 2	SP
4	Same as 3	Same as 2	SP
5	Same as 3	Same as 2	SP
6	Same as 3	Same as 2	SP
7	Same as 3	Fused and Crushed ScSZ	SP
8	Same as 3	Same as 2	SP

Table 6: Electrochemical results from Vassen, et al [136].

Sample #	T(^{o}C)	Voltage @ 500mA (mV)	Current Density @0.7V (A/cm^2)
1	809-817	911	0.42-0.32
2	789	970-980	0.33-0.38
3	803-807	950-987	0.58-0.67
4	802-803	1044-1053	0.23-0.38
5	815-819	981	0.84-0.91
6	808-814	1025-1048	0.43-0.86
7	792-800	1031-1035	0.60-0.65
8	843	1011-1016	0.52

*Electrolyte thickness $< 40\mu$m

gel process can produce samples with similar electrochemical properties requiring ~0.2V-0.85V to maintain 300mA.

The measured current densities are similar as well. These data were obtained at 0.7V. The only sample in this investigation to approach that value was #13big and 09-19-00 at 0.6V. The current densities for these samples are much lower and are attributed to the higher thickness of the membrane.

6.3 Presence of a Triple Phase Boundary

The formation of a triple phase boundary was examined in sample #13small, tube 6, tube 7, and 09-19-00. The areas selected for imaging of #13big and 06-30-00 did not show any evidence of a TPB. Figure 46 shows a membrane that seems uniform in structure and conductivity indicating the YSZ and LSM membranes mixed eliminating the separate membrane structure. However, electrochemical tests suggest that #13big has some membrane separation and it behaves similarly to samples where a TPB was observed. Areas imaged on other samples (Figure 47, 50, 51, 54, and 57) suggest areas of membrane mixing as well. Inconsistencies in the charging effect but similarities in the apparent density and structure where the electrolyte is expected to be suggest damage to the cross section. Polishing may not only have caused damage to parts of the membranes but may have introduced conductive contaminants that embedded or adhered to the surface.

Using the sol-gel process to assemble the device, the entire membrane structure varied between 80 and 250μm. For all samples with 50 electrolyte layers, the YSZ

membrane was between 35-45μm. Sample 09-19-00, which had 96 layers, had an electrolyte layer measuring approximately 60μm up to 140μm in some areas. Except for #13small, the layering process yielded similar electrolyte thicknesses on all samples. The electrodes, however, were more variable ranging from 6-70μm for the LSM anode. This variability leads to the range of thicknesses of the triple phase boundaries on different samples. The anode layer of LSM on tube 6 was ~6.3μm and the TPB ranged between 2.5-3.5μm. Sample 06-30-00 has an LSM anode measuring approximately 45μm and the TPB in this area is ~15μm. The LSM anode of sample 09-19-00 has a thickness of 70μm and the TPB ranged from ~20-45μm. These TPBs were not limited to the cathode side of the samples and were also observed at the electrolyte/anode interface.

The triple phase boundary is non-uniform in all of the areas imaged. The width varies within these ranges and in some areas there is no indication of a TPB as seen in Figures 48, 51, and 52. It is apparent from the electrochemical data that the isolated areas where the TPB is present allow for oxygen reduction. Areas that lack a triple phase boundary may limit the overall rate at which ions are introduced to the electrolyte, the conductivity and the current density. Despite the non-uniformity of the TPB, at an operating temperature greater than ~800°C, the fuel cell is still operable.

6.4 Fuel Cell Operation

6.4.1 Electrical Generation

The electrochemical data indicates that the electrolyte is capable of transporting oxygen ions. A current density of 0.1A/cm^2 between 0.05V and 0.3V was observed for

sample 06-30-00. Without an applied voltage, the hydrogen forming gas was introduced to the system. This produced a voltage ranging between 0.342-0.353V and a current of ~250mA. The active surface area of the platinum patches on the sample is ~10cm^2. The area of the triple phase boundary where oxygen reduction and transport occurs cannot be measured because it is internal to the device but is assumed to be much smaller. An investigation by Lee et al. [137] using the same materials referenced in section 6.2 (NiO-YSZ/YSZ/LSM) through tape-casting (screen printed cathode) yielded higher voltages at operating temperature with a smaller determined surface area [137]. Their SOFCs had a surface area of ~3.14cm^2 with a matching TPB. This cell produced 1.10V at 800°C with an electrolyte thickness of 150μm. The membrane structures developed by tape-casting are uniform and have good adhesion providing a better interface for ion transport. Table 7 lists the conditions these cells were tested under. Although the performance of sample 06-30-00 is poor by comparison to other investigations, processing optimization can greatly enhance the cell performance.

6.4.1 Oxygen Generation

While the goal remains to use this device to produce pure oxygen, no quantitative measurement of oxygen production was possible. Nevertheless, in all electrochemical tests and when operated as a fuel cell oxygen transport is the only mechanism that can produce the data recorded. No impurities or short circuits were observed in the SEM images that suggest an unexpected anodic reaction consuming O_2.

Table 7: H$_2$ testing results of SOFC developed by tapecasting [137].

	800°C	**900°C**
H$_2$-air fuel cell	1.10V	1.08V
H$_2$-O$_2$ fuel cell	1.13V	1.12V

The pressure applied by the forming gas H_2 flow during electrical generation suggests the membrane can hold the oxygen collected at the anode without failing. Slow gas leaks in the membrane could account for the loss of oxygen before it can be measured. These leaks would not be evident during H_2 testing. The forming gas may leak but a reaction can still be seen as the gas reacts with oxygen ions at the anode producing electricity.

7.0 CONCLUSIONS

The conclusion section of the dissertation applies to the synthesis, processing, and characterization of YSZ solutions and supported LSM/YSZ/LSM fuel cells. The objectives achieved in this study were:

(a) Assembling an all sol-gel solid oxide fuel cell.

(b) Producing a voltage when it was operated at $800^{o}C$ with forming gas and air.

7.1 Solution Reproducibilty

The sol-gel process has been used successfully to produce a YSZ electrolyte solution with a consistent viscosity, particle size, and thermal behavior confirmed using TGA, XRD, and dynamic light scattering. The solutions had a particle size between 250-300nm. A weight loss of approximately 55% occurred in the analyzed samples when heated to $1200^{o}C$. The expected crystal structure was a mixture of tetragonal and cubic with an emphasis on tetragonal. A cubic crystal phase was not observed using XRD and all samples were tetragonal.

An electrolyte solution with the addition of ethylene glycol (EG) used to raise viscosity was tested to improve weight gain during membrane development. The EG solution yielded higher weight gains along with higher weight losses. Processing membranes with this solution can yield similar results but requires a higher volume so there is significant advantage to an EG sol.

7.2 Membrane Processing

Anode, electrolyte, and cathode layers were assembled using a brush coating technique that produced better results than the dip coating method. The LSM/YSZ/LSM membrane structure typically had a thickness of 80μm. The electrochemical performance of the membranes was not as good when the thickness increased over 100μm. Approximately 50 layers of YSZ solution produced 1.5-2.0g of weight gain on the sample forming an electrolyte $\sim35\mu$m thick. The sintering methods for the proper membrane structure were determined, requiring heat treatments at 1100°C and 1200°C.

A triple phase boundary formed between the electrodes and electrolyte promoting oxygen reduction. This boundary was not uniform. All layers showed variations in thickness.

7.3 Sol-Gel Processed Fuel Cell

An operational fuel cell developed solely through sol-gel processing was produced. The fuel cell produced ~250mA of current and a voltage of 0.35V at 800°C when tested in a forming gas (93% N_2 and 7% H_2)--Air environment. This preliminary test does not meet the power output expected for solid oxide fuel cells. Nonetheless, the power output confirms the proper electrochemical response. The results show that oxygen ion transport occurs in the YSZ electrolyte.

SUGGESTIONS FOR FUTURE WORK

Zirconia has shown its highest ionic conductivity when in the form of the fluorite cubic crystal structure [91, 93-95]. Only a tetragonal structure was developed in this study. Adjusting sintering temperatures and times to produce a solely cubic structure may increase cell performance. Abandoning 1100^oC for 1200^oC at every layer with a final heat treatment of 1300^oC is suggested.

More studies on the optimization of the membrane structures through sintering methods should be performed. Focusing on producing uniform layers and a consistent triple phase boundary is crucial to improving the performance of the fuel cell.

Finding a quantitative relation between the TPB and performance would be useful. This would give a better understanding of the interaction of the LSM and YSZ layers during the sol-gel coating process. Also, the extent of electrode/electrolyte mixing in the TPB, its porosity and its surface area are features that need further study.

New samples should also be developed and tested electrochemically for oxygen production. The factors that increase oxygen production need to be studied to evaluate the feasibility of using this device as an oxygen generator.

REFERENCES*

1. Naval Facilities Engineering Service Center. "Impacts of the Energy Policy Act of 2005 on Federal Facility Operations". Emerging Environmental Issues. October 2005. <http://p2library.nfesc.navy.mil/issues/emergeoct2005/index.html>

2. Spokane County Conservation District. "Summary of Biofuels and Alternative Fuel Provisions". Energy Policy Act of 2005. January 2006. <www.federalsustainability.org/initiatives/biodiesel/Summary%20of%202005%20Energy%20Policy%20Act.pdf>

3. State and the Office of the Houses of the Oireachtas. "Environmental Protection Agency Act 1992". Acts of the Oireachtas. April 1992. <http://acts.oireachtas.ie/zza7y1992.1.html>

4. American Council for an Energy-Efficient Economy. "Energy Efficiency Program for Certain Commercial and Industrial Equipment: Test Procedures, Labeling, and the Certification Requirements for Electric Motors". Motor Provisions in the Energy Policy Act of 1992. January 2004. <http://www.aceee.org/Motors/epact.htm>

5. Karim Nice, Jonathan Strickland. *"How Fuel Cells Work"*. September 18, 2000 <http://auto.howstuffworks.com/fuel-cell.htm> (December 15, 2007)

6. "Energy Policy Act of 2005". (PL 109-58, Aug. 8, 2005). United States Statutes at Large 119 (2005) 594-1143.

7. SEO, Emília Satoshi Miyamaru, YOSHITO, Walter Kenji, USSUI, Valter et al. "Influence of the starting materials on performance of high temperature oxide fuel cells devices". Materials Research. 2004, vol. 7, no. 1 [cited 2007-12-15], pp. 215-220. Available from: <http://www.scielo.br/scielo.php?script=sci_arttext&pid=S1516-14392004000100029&lng=en&nrm=iso>. ISSN 1516-1439. doi: 10.1590/S1516-14392004000100029electrolytic web>

8. P. Preuss. "A Better Way to Produce Oxygen: On Site Without a Delivery Truck". Science Beat at Berkeley Lab. December 2000. <http://www.lbl.gov/Science-Articles/Archive/oxygen-onsite.html>

9. D. Xiaming, L. Qingfeng, T. Yuying. "Study of Phase Formation in Spray Pyrolysis of ZrO2 and ZrO2-Y2O3 Powders". Journal of the American Ceramic Society. 76, 3 (1992) 760-762.

---

* All websites cited on December 15, 2007 except those from electronic journal databases.

10. A. Boulle, O. Masson, R. Guinebretiere, A. Dauger. "X-Ray Diffraction from Epitaxial Oxide Layers Grown from Sol-Gel". <u>Thin Solid Films</u>. 434 (2003) 1-6.

11. J. Adair, R. Denkewicz, F. Arnagada, K. Osseo-Asare. "Precipitation and In-Situ Transformation in the Hydrothermal Synthesis of Crystalline Zirconium Dioxide". <u>Ceramic Transactions Vol I, Ceramic Powder Science Vol IIA</u>. Ed. E.R. Fuller, H. Hausner. Westerville, Ohio: The American Ceramic Society, 1988. 135-145.

12. J. Woodhead, K. Cole, J. Dalton, J. Evans, E. Paige. "The Preparation of Crystalline Ceramic Compounds by Sol-Gel Processes". <u>Science of Ceramics 12-Ceramurgica</u>. Faenza: Italy, 1984. 179-185.

13. M. Albano, L. Genova, L. Garrido, K. Plucknett. In Press: "Processing of Porous Yttria-Stabilized Zirconia by Tape Casting". <u>Ceram. Int</u>. (2007). doi:10.1016/j.ceramint.2007.07.028. <http://www.sciencedirect.com>

14. M. Albano, L. Garrido. "Aqueous Tape Casting of Yttris Stabilized Zirconia". <u>Materials Science and Engineering</u>. A420 (2006) 171-178. <http://www.sciencedirect.com>

15. U.S. Department of Energy. "Hydrogen, Fuel Cells and Infrastructure Technologies Program". <u>Energy Efficient and Renewable Energy</u>. March 2007. <http://www1.eere.energy.gov/hydrogenandfuelcells/fuelcells/fc_types.html>

16. C. Bezerra, et al. "A Review of Heat Treatment Effects on Activity and Stability of PEM Fuel Cell Catalysts for Oxygen Reduction Reaction". <u>Journal of Power Sources</u>. 173 (2007) 891-908. <http://www.sciencedirect.com>

17. A. Kulikovsky. "Heat Transport in the Membrane Electrode Assembly of a Direct Methanol Fuel Cell: Exact Solutions". <u>Electrochimica Acta</u>. 53 (2007) 1353-1359. <http://www.sciencedirect.com>

18. J. Varcoe, et al. "Investigations into the Ex-Situ Methanol, Ethanol, and Ethylene Glycol Permeabilities of Alkaline Polymer Electrolyte Membranes". <u>Journal of Power Sources</u>. 173 (2007) 194-199. <http://www.sciencedirect.com>

19. W.Z. Zhu, S.C. Deevi. "A Review on the Status of Anode Materials for Solid Oxide Fuel Cells". <u>Materials Science and Engineering</u>. A362 (2003) 228-239. <http://www.sciencedirect.com>

20. E. Garrison. "Solid Oxide Fuel Cells". <u>Illinois Institute of Technology</u>. August 2006. <http://www.iit.edu/~smart/garrear/fuelcells.htm>

21. E. DeGuire. "Solid Oxide Fuel Cells". <u>Pro Quest</u>. April 2003. <http://www.csa.com/discoveryguides/fuecel/overview.php>

22. F.T. Ciacchu, S. Badwal, V. Zelizko. "Tubular Zirconia-Yttria Electrolyte Membrane Technology for Oxygen Separation". Solid State Ionics. 152-153 (2002) 763-768. <http://www.sciencedirect.com>

23. A. Virkar. "A Model for Solid Oxide Fuel Cell (SOFC) Stack Degradation". Journal of Power Sources. 172 (2007) 713-724. <http://www.sciencedirect.com>

24. M. Ni, M. Leung, D. Leung. "A Modeling Study on Concentration Overpotentials of a Reversible Solid Oxide Fuel Cell". Journal of Power Sources. 163 (2006) 460-466. <http://www.sciencedirect.com>

25. M.W. Barsoum. Fundamentals of Ceramics. Ed. B.J. Clark, J.M. Morris. New York: McGraw Hill Company, 1997.

26. J.S. Thokchom, et al. "Heterogeneous Electrolyte (YSZ-Al2O3) Based Direct Oxidation Solid Oxide Fuel Cell". Journal of Power Sources. (2007). doi:10.1016/j.jpowsour.2007.12.009. <http://www.sciencedirect.com>

27. C. Wang, et al. "Fabrication and Performance of Thin Film YSZ Solid Oxide Fuel Cells". Journal of the Electrochemical Society. 148, 8 (2001) A864-A868.

28. W.D. Kingery, H.K. Bowen, D.R. Uhlmann. Introduction to Ceramics 2nd Edition. New York: John Wiley & Sons, Inc., 1960.

29. P. Salvador. "Materials for SOFCs: Lecture 1 and 2". Carnegie Mellon University. Power Point. 2003. 15 December 2007. <http://neon.materials.cmu.edu/salvador/specialtopics/SOFClecture2Final.ppt#329,35,Why don't we use Ceria?>

30. M.E. Glicksman. Diffusion in Solids: Field Theory, Solid-State Principles, and Applications. New York: John Wiley & Sons, Inc., 2000.

31. J. Goodenough, Y. Huang. "Alternative Anode Materials for Solid Oxide Fuel Cells". Journal of Power Sources. 173 (2007) 1-10. <http://www.sciencedirect.com>

32. R. Hui, et al. "Fabrication of Ceramic Films for Solid Oxide Fuel Cells via Slurry Spin Coating Technique". Journal of Power Sources. 172 (2007) 840-844. <http://www.sciencedirect.com>

33. R. Hui, et al. "A Brief Review of the Ionic Conductivity Enhancement for Selected Oxide Electrolytes". Journal of Power Sources. 172 (2007) 493-502. <http://www.sciencedirect.com>

34. T. Omata, Y. Goto, S. Matsuo. "Nanocrystals of Zirconia and Ceria Based Electrolytes: Syntheses and Properties". Science and Technology of Advanced Materials. 8, 6 (2007) 524-530. <http://www.sciencedirect.com>

35. W. Zajac, K. Swierczek, J. Molenda. "Thermochemical Compatability Between Selected (LaSr)(CoFeNi)O3 Cathodes and Rare Earth Doped Ceria Electrolytes". <u>Journal of Power Sources</u>. 173 (2007) 675-680. <http://www.sciencedirect.com>

36. L. Baldrianova, I. Svancara, S. Sotiropoulos. "Anodic Stripping Voltammetry at a New Type of Disposable Bismuth-Plated Carbon Paste Mini-Electrodes". <u>Analytica Chimica Acta</u>. 599 (2007) 249-255. <http://www.sciencedirect.com>

37. B. Bai, N.M. Sammes, A.L. Smirnova. In Press: "Physical and Electrochemical Characterization of Bi2O3 Doped Scandia Stabilized Zirconia". <u>Journal of Power Sources</u>. (2007). doi:10.1016/j.jpowsour.2007.10.074. <http://www.sciencedirect.com>

38. R. Murugan, et al. "Structure and Lithium Ion Conductivity of Bismuth Containing Lithium Garnets Li5La3Bi2O12 and Li6SrLa2Bi2O12". <u>Materials Science and Engineering: B</u>. 143 (2007) 14-20. <http://www.sciencedirect.com>

39. Z. Liu, M. Min-Fang, W. Miao. "Preparation and Characterization of Graded Cathode La0.6Sr0.4Co0.2Fe0.8O3-X". <u>Journal of Power Sources</u>. 173 (2007) 837-841. <http://www.sciencedirect.com>

40. Y. Xing, et al. In Press:"Influence of Through-Lamella Grain Growth on Ionic Conductivity of Plasma-Sprayed Yttria Stabilized Zirconia as an Electrolyte in Solid Oxide Fuel Cells". <u>Journal of Power Sources</u>. (2007). doi:10.1016/j.jpowsour.2007.10.031. <http://www.sciencedirect.com>

41. X. Yu, S. Licht. "Zirconia Coating Stabilized Super-Iron Alkaline Cathodes". <u>Journal of Power Sources</u>. 173 (2007) 1012-1016. <http://www.sciencedirect.com>

42. H. Hong, U. Chae, S. Choo. "The Effect of Ball Milling Parameters and Ni Concentration on a YSZ-Coated Ni Composite for a High Temperature Electrolysis Cathode". <u>Journal of Alloys and Compounds</u>. 449 (2008) 331-334. <http://www.sciencedirect.com>

43. B. Borglum, N. Bessette. "Electrode Electrolyte Interlayers Containgin Cerium Oxide for Electrochemical Fuel Cells". U.S. Patent 6139985. October 31, 2000. <http://www.patentstorm.us/patents/6139985-description.html>

44. M. Han, et al. "Fabrication, Microstructure and Properties of a YSZ Electrolyte for SOFCs". <u>Journal of Power Sources</u>. 165 (2007) 757-763. <http://www.sciencedirect.com>

45. V. Lughi, D. Clarke. "Low Temperature Transformation Kinetics of Electron Beam Deposited 5 Wt% Yttria Stabilized Zirconia". <u>Acta Materialia</u>. 55 (2007) 2049-2055. <http://www.sciencedirect.com>

46. J. Liu, et al. "Study on the Properties of YSZ Electrolyte Made by Plaster Casting Method and the Applications in Solid Oxide Fuel Cells". Solid State Ionics. 118 (1999) 67-72.

47. T. Etsell, S. Flengas. "The Electrical Properties of Solid Oxide Electrolytes". Chemical Reviews. 70, 3 (1970) 339-376.

48. S. Badwal, "Stability of Solid Oxide Fuel Cell Components". Solid State Ionics. 143 (2001) 39-46.

49. A.R. Rojas, et al. "In Situ X-Ray Rietveld Analysis of Ni-YSZ Solid Oxide Fuel Cell Anodes During NiO Reduction in H2". Journal of Physics D: Applied Physics. 38 (2005) 2276-2282. <http://www.iop.org>

50. J. Goodenough, et al. "Porous Carbon Anodes for the Direct Methanol Fuel Cell—1. The Role of the Reduction Method for Carbon Supported Platinum Electrodes". Electrochimica Acta. 35, 1 (1990) 199-207. <http://www.sciencedirect.com>

51. P. Hernandez-Fernandez, et al. "An Opening Route to the Design of Cathode Materials for Fuel Cells Based on PtCo Nanoparticles". Applied Catalysis B: Environmental. 77, 1-2 (2007) 19-28. <http://www.sciencedirect.com>

52. J. Piao, et al. "Preparation and Characterization of Pr1-XSrXFeO3 Cathode Material for Immediate Temperature Solid Oxide Fuel Cells". Journal of Power Sources. 172 (2007) 633-640. <http://www.sciencedirect.com>

53. E. Brosha, et al. "Techniques for the Thin Film Growth of La1-XSrXCrO3 for Solid State Ionic Devices". Solid State Ionics. 166, 3-4 (2004) 425-440. <http://www.sciencedirect.com>

54. A. Hammouche, E. Siebert, A. Hammou, M. Kleitz. "Electrocatalytic Properties and Nonstoichiometry of the High Temperature Air Electrode La1-XsrXMnO3". Journal of the Electrochemical Society. 138, 5 (1991) 1212-1216.

55. M.J. Jorgensen, et al. "Effect of Sintering Temperature on Microstructure and Performance of LSM-YSZ Composite Cathodes". Solid State Ionics. 139 (2001) 1-11.

56. S. Badwal. "Grain Boundary Resistivity in Zirconia-Based Materials: Effect of Sintering Temperatures and Impurities". Solid State Ionics. 76 (1995) 67-80.

57. C. Brugnoni, U. Ducati, M. Scagliotti. "SOFC Cathode/Electrode Interface. Part 1: Reactivity Between La0.85Sr0.15MnO3 and ZrO2-Y2O3". Solid State Ionics. 76, 3-4 (1995) 177-182. <http://www.sciencedirect.com>

58. M.C. Brant, L. Dessemond. "Electrical Degradation of LSM-YSZ Interfaces". <u>Solid State Ionics</u>. 138 (2000) 1-17. <http://www.sciencedirect.com>

59. J. Hertz, H. Tuller. "Measurement and Finite Element Modeling of Triple Phase Boundary Related Current Constriction in YSZ". <u>Solid State Ionics</u>. 178 (2007) 915-923. <http://www.sciencedirect.com>

60. U. Balachandran, T.H. Lee, S.E. Dorris. "Hydrogen Production by Water Dissociation Using Mixed Conducting Dense Ceramic Membranes". <u>International Journal of Hydrogen Energy</u>. 32 (2007) 451-456. <http://www.sciencedirect.com>

61. J. Wang, M. Liu, M.C. Lin. "Oxygen Reduction Reactions in the SOFC Cathode of Ag/CeO2". <u>Solid State Ionics</u>. 177 (2006) 939-947. <http://www.sciencedirect.com>

62. X. Deng, A. Petric. "Geometrical Modeling of the Triple Phase Boundary in Solid Oxide Fuel Cells". <u>Journal of Power Sources</u>. 140 (2005) 297-303. <http://www.sciencedirect.com>

63. R. Kant, K. Singh, O. Pandey. In Press:"Synthesis and Characterization of Bismuth Vanadate Electrolyte Material with Aluminum Doping for SOFC Application". <u>International Journal of Hydrogen Energy</u>. (2007). doi:10.1016/j.ijhydene.2007.07.025. <http://www.sciencedirect.com>

64. S. Sarat, N. Sammes, A. Smirnova. "Bismuth Doped Scandia Stabilized Zirconia Electrolyte for the Intermediate Temperature Solid Oxide Fuel Cells". <u>Journal of Power Sources</u>. 160 (2006) 892-896. <http://www.sciencedirect.com>

65. N.M. Sammes, et al. "Bismuth Based Oxide Electrolytes-Structure and Ionic Conductivity". <u>Journal of the European Ceramic Society</u>. 19 (1999) 1801-1826. <http://www.sciencedirect.com>

66. A. Atkinson. "Chemically Induced Stresses in Gadolinium Doped Ceria Solid Oxide Fuel Cell Electrolytes". <u>Solid State Ionics</u>. 95, 3-4 (1997) 249-258. <http://www.sciencedirect.com>

67. V. Thangadurai, P. Kopp. "Chemical Synthesis of Ca Doped CeO2-Intermediate Temperature Oxide Ion Electrolytes". <u>Journal of Power Sources</u>. 168 (2007) 178-183. <http://www.sciencedirect.com>

68. N. Sakai, et al. "Transport Properties of Ceria-Zirconia-Yttria Solid Solutions {(CeO2)X(ZrO2)1-X}1-Y(YO1.5)Y(X=0-1,Y=0.2,0.35)". <u>Journal of Alloys and Compounds</u>. 408-412 (2006) 503-506. <http://www.sciencedirect.com>

69. W. Zhou, et al. "High Performance Electrode for Electrochemical Oxygen Generator Cell Based on Solid Electrolyte Ion Transport Membrane". <u>Electrochimica Acta</u>. 52 (2007) 6297-6303. <http://www.sciencedirect.com>

70. H.R. Webb. "Chemistry: Foundations and Applications. Scandium". <u>BNET Research Center</u>. August 2004.
    <http://findarticles.com/p/articles/mi_gx5216/is_2004/ai_n19132954>

71. R. Stevens. "An Introduction to Zirconia: Zirconia and Zirconia Ceramics". <u>Magnesium Elektron Ltd 2nd Ed</u>. 113 (1986) 13.

72. H.P. Beck, C. Kaliba. "High Pressure Investigation on Zirconia Doped with Cr, Fe, and Nb". <u>Materials Research Bulletin</u>. 26 (1991) 145.

73. R.S. Pavlik. "Zirconia Membranes by the Sol-Gel Method". <u>PhD Thesis</u>. (1994). Rutgers, The State University of New Jersey.

74. W.R. Cannon. "Transformation Toughened Ceramics for Structural Applications". <u>Treatise on Materials Science and Technology</u>. 29 (1989) 195.

75. R. Ruh, T.J. Rockett. "Proposed Phase Diagram for the System ZrO2". <u>Journal of the American Ceramic Society</u>. 53 (1970) 360.

76. R.C. Garvie. "The Occurrence of Metastable Tetragonal Zirconia as a Crystallite Size Effect". <u>Journal of Physical Chemistry</u>. 69 (1965) 1238.

77. Y. Murase, E. Kato. "Role of Water Vapor in Crystallite Growth and Tetragonal-Monoclinic Phase Transformation of Zirconia". <u>Journal of the American Ceramic Society</u>. 66 (1983) 196.

78. I.A. El-Shanshoury, V.A. Rudenko, I.A. Ibrahim. "Polymorphic Behavior of Thin Evaporated Films of Zirconium and Hafnium Oxides". <u>Journal of the American Ceramic Society</u>. 53 (1970) 264.

79. E.D. Whitney, "Kinetics and Mechanism of the Transition of Metastable Tetragonal to Monoclinic Zirconia". <u>Transactions of the Faraday Society</u>. 61 (1965) 1991.

80. T. Mitshuashi, M. Ichiara, V. Tatsuke. "Characterization and Stabilization of Metastable Tetragonal Zirconia". <u>Journal of the American Ceramic Society</u>. 57 (1974) 97.

81. R.C. Garvie. "Stabilization of the Tetragonal Structure in Zirconia Microcrystals". <u>Journal of Physical Chemistry</u>. 82 (1978) 218.

82. M.J. Torralvo, J. Soria, M.A. Alario. "Non-Stoichiometry and the Glow Phenomenon in Zirconia Gels". <u>Proceedings of the 9th International Symposium on the Reactivity of Solids</u>. Cracow (1980) 306.

83. M.J. Torralvo, M.A. Alario, J. Soria. "Metastability of Tetragonal Zirconia Powders". <u>Journal of Catalysis</u>. 86 (1984) 473.

84. M.I. Osendi, et al. "Metastability of Tetragonal Zirconia Powders". <u>Journal of the American Ceramic Society</u>. 68 (1985) 135.

85. R.P. Denkewicz, K.S. TenHuisen, J.H. Adair. "Hydrothermal Crystallization Kinetics of m-ZrO2 and t-ZrO2". <u>Journal of Materials Research</u>. 5 (1990) 2698.

86. A. Ayral, et al. "Zirconia by the Gel Route". <u>Journal of Material Science</u>. 25 (1990) 1268.

87. M.M. Rashad, H.M. Baioumy. "Effect of Thermal Treatment on the Crystal Structure and Morphology of Zirconia Nanopowders Produced by Three Different Routes". <u>Journal of Materials Processing Technology</u>. 195, 1-3 (2008) 178-185. <http://www.sciencedirect.com>

88. M. Kusunoki, et al. "In Situ Observation of Zirconia Particles at 1200°C by High Resolution Electron Microscopy". <u>Journal of the American Ceramics Society</u>. 76, 3 (1993) 763-765.

89. M. Yashima, N. Ishizawa, M. Yoshimura. "High Temperature X-Ray Study of the Cubic-Tetragonal Diffusionless Phase Transition in the ZrO2-ErO2 System: I, Phase Change Between Two Forms of a Tetragonal Phase, t'-ZrO2 and t''-ZrO2, in the Compositionally Homogeneous 14 mol% ErO1.5-ZrO2". <u>Journal of the American Ceramics Society</u>. 76, 3 (1993) 641-648.

90. R.C. Garvie. "The Occurrence of Metastable Tetragonal Zirconia as a Crystallite Size Effect". <u>Journal of Physical Chemistry</u>. 69, 4 (1965) 1236-1243.

91. International Society of Electrochemistry. "Systems with Fast Ionic Transport: Proceedings of the Third International Symposium on Systems with Fast Ionic Transport, Holzhau Germany". <u>Materials Science Forum</u>. Vol 76. Zurich: Trans Tech Publications. 1991.

92. S.F. Watkins. "Crystal Lattice Structures: Calcium Fluoride". <u>Department of Chemistry, Louisiana State University</u>. 17 October 2000. <http://wb.chem.lsu.edu/htdocs/people/sfwatkins/MERLOT/lattice/19fluor.html>

93. M.R. McClure. "The Crystal Lattice Gallery: Visualizations of Crystal Lattice Structures: Fluorite Structure". <u>University of North Carolina at </u>Pembroke. 19 October 2007. <http://www.uncp.edu/home/mcclurem/lattice/fluorite.htm>

94. C.Chen. "Solid Oxide Fuel Electrolyte Membrane Fabrication". <u>Master's Thesis</u>. May 2003. University of Virginia. <http://people.virginia.edu/~jfg6e/groves/Masters/Chen_2003/>

95. G. Dell'Agi, G. Mascolo. "Hydrothermal Synthesis of ZrO2-Y2O3 Solid Solutions at Low Temperature". <u>Journal of the European Ceramic Society</u>. 20, 2 (2000) 139-145. <http://www.sciencedirect.com>

96. C. Sakurai, et al. "Preparation of Zirconia Coatings by Hydrolysis of Zirconium Alkoxide with Hydrogen Peroxide". <u>Journal of the American Ceramic Society</u>. 76, 4 (1993) 1061-1064. <http://ammtiac.alionscience.com/>

97. S. Kim, et al. "Fabrication and Characterization of a YSZ/YDC Composite Electrolyte by a Sol-Gel Coating Method". <u>Journal of Power Sources</u>. 110 (2002) 222-228. <http://www.sciencedirect.com>

98. Y. Shiratori, et al. "YSZ-MgO Composite Electrolyte with Adjusted Thermal Expansion Coefficient to Other SOFC Components". <u>Solid State Ionics</u>. 164, 1-2 (2003) 27-33. <http://www.sciencedirect.com>

99. R. Mukundan, E.L. Brosha, F.H. Garzon. "Mixed Potential Hydrocarbon Sensors based on a YSZ Electrolyte and Oxide Electrodes". <u>Journal of the Electrochemical Society</u>". 150, 12 (2003) 279-284.

100. E. Brosha, et al. "Mixed Potential Sensors using Lanthanum Manganate and Terbium Yttrium Zirconium Oxide Electrodes". <u>Sensors and Actuators B: Chemical</u>. 87, 1 (2002) 47-57. <http://www.sciencedirect.com>

101. E. Brosha, et al. "Development of Ceramic Mixed Potential Sensors for Automotive Applications". <u>Solid State Ionics</u>. 148, 1-2 (2002) 61-69. <http://www.sciencedirect.com>

102. R. Srinivasan. "Identification of Tetragonal and Cubic Structures of Zirconia using Synchrotron X-Radiation Source". <u>Journal of Material Research</u>. 6, 6 (1991) 1287-1292.

103. R.C. Garvie, M.V. Swain. "Thermodynamics of the Tetragonal to Monoclinic Phase Transformation in Constrained Zirconia Microcrystals". <u>Journal of Material Science</u>. 20 (1985) 1193-1200.

104. G. Gongyi, C. Yuli. "Effect of Preparation Methods and Condition of Precursors on the Phase Composition of Yttria Stabilized Zirconia Powders". <u>Journal of the American Ceramic Society</u>. 75, 5 (1992) 1294-1296.

105. K. Chen, et al. "Development of LSM-Based Cathodes for Solid Oxide Fuel Cells Based on YSZ Films". <u>Journal of Power Sources</u>. 172 (2007) 742-748. <http://www.sciencedirect.com>

106. M. Berrisford. "Solid Oxide Fuel Cells". <u>Ceram Research</u>. 12 September 2001. <http://www.azom.com/details.asp?ArticleID=919#>

107. J.H. Kuo, H.U. Anderson, D.M. Sparlin. "Oxidation-Reduction Behavior of Undoped and Sr-Doped LaMnO3 Nonstoichiometry and Defect Structure". <u>Journal of Solid State Chemistry</u>. 83 (1989) 52-60.

108. E.P. Murray, T. Tsai, S.A. Barnett. "Oxygen Transfer Processes in (La, Sr)MnO3/Y2O3 Stabilized ZrO2 Cathodes: An Impedance Spectroscopy Study". <u>Solid State Ionics</u>. 110 (1998) 235-243.

109. D.J. Clark, R.W. Losey, J.W. Suitor. "Zirconia Solid Electrolyte Membranes for Oxygen Transport". <u>Jet Propulsion Laboratory, California Institute of Technology</u>. (1999).

110. S. Otsuka, Y. Matsumura, Z. Kozuka. "Electrochemical Study of Oxygen Released from Stabilized Zirconia Electrolyte". <u>Solid State Ionics</u>. 3-4 (1981) 495-498.

111. C. Viazzi, J.P. Bonino, F. Ansart. "Synthesis by Sol-Gel Route and Characterization of Yttria Stabilized Zirconia Coatings for Thermal Barrier Applications". <u>Surface Coatings Technology</u>. 201, 7 (2006) 3889-3893. <http://www.sciencedirect.com>

112. K.R. Sridhar, B.T. Vaniman. "Oxygen Production on Mars using Solid Oxide Electrolysis". <u>Solid State Ionics</u>. 93 (1997) 321-328.

113. D.L. Meixner, et al. "Electrochemical Oxygen Separation using Solid Electrolyte Ion Transport Membranes". <u>Journal of the Electrochemical Society</u>. 149 (2002) 132-136.

114. Y. Suzuki. "Activation Energy for Electrical Conduction of Y2O3 Stabilized ZrO2 Containing 8 mol% Y2O3". <u>Solid State Ionics</u>. 91 (1996) 239-241.

115. G.M. Ingo. "Origin of Darkening in 8 wt% Yttria-Zirconia Plasma Sprayed Thermal Barrier Coatings". <u>Journal of the American Ceramic Society</u>. 74, 2 (1991) 381-386.

116. Y. Chen, W.J. Wei. "Processing and Characterization of Ultra-Thin Yttria Stabilized Zirconia (YSZ) Electrolytic Films for SOFC". <u>Solid State Ionics</u>. 177 (2006) 351-357. <http://www.sciencedirect.com>

117. S.C. Singhal. "Solid Oxide Fuel Cells for Stationary, Mobile, and Military Applications". <u>Solid State Ionics</u>. 152-153 (2002) 405-410. <http://www.sciencedirect.com>

118. J. Livage, C. Sanchez. "Sol-Gel Chemistry". <u>Journal of Non-Crystalline Solids</u>. 145 (1992) 11-19.

119. L.C. Klein, L. Laby, G. Lous. "Sol-Gel Processing for Lithium Battery Materials". Ed. F.D. Gnanam. International Workshop on Sol-Gel Processing of Advanced Ceramics. January 1996.

120. C.J. Brinker, G.W. Scherer. Sol-Gel Science. New York: Academic Press, 1990.

121. L.C. Klein, N. Giszpenc. "Sol-Gel Processing for Gas Separation Membranes". American Ceramic Society Bulletin. 69 (1990) 1821-1825. <http://hwwilsonweb.com>

122. E.A. Lee, et al. "Sol-Gel Derived (La0.8M0.2)CrO3(MCa, Sr) Coating Layer on Stainless Steel Substrate for use as a Separator in Intermediate Temperature Solid Oxide Fuel Cell". Journal of Power Sources. 157, 2 (2006) 709-713. <http://www.sciencedirect.com>

123. S. Hong, S.W. Nam. "Application of Sol-Gel Techniques in Fabrication of Fuel Cells". Studies in Surface Science and Catalysis. 159 (2006) 79-84. <http://www.sciencedirect.com>

124. J. Liu, et al. "Oxygen Reduction at Sol-Gel Derived La0.8Sr0.2Co0.8Fe0.2O3 Cathodes". Solid State Ionics. 177, 3-4 (2006) 377-387. <http://www.sciencedirect.com>

125. R. Jiang, H.R. Kunz, J.M. Fenton. "Composite Silica/Nafion® Membranes Prepared by Tetraethylorthosilicate Sol-Gel Reaction and Solution Casting for Direct Methanol Fuel Cells". Journal of Membrane Science. 272, 1-2 (2006) 116-124. <http://www.sciencedirect.com>

126. L. Rose, et al. "Application of Sol Gel Spin Coated Yttria Stabilized Zirconia Layers for the Improvement of Solid Oxide Fuel Cell Electrolytes Produced by Atmospheric Plasma Spraying". Journal of Power Sources. 167, 2 (2007) 340-348. <http://www.sciencedirect.com>

127. C. Viazzi, et al. "Synthesis of Yttria Stabilized Zirconia by Sol–Gel Route: Influence of Experimental Parameters and Large Scale Production". Solid State Sciences. 8, 9 (2006) 1023-1028. <http://www.sciencedirect.com>

128. J.L. Shi, M.L. Ruan, T. S. Yen. "Crystallite Growth in Yttria-Doped Superfine Zirconia Powders and Their Compacts: A Comparison Between Y-TZP and YSZ". Ceramics International. 22, 2 (1996) 137-142. <http://www.sciencedirect.com>

129. F. Mauvy, et al. "Electrochemical Characterization of YSZ Thick Films Deposited by Dip-Coating Process". Journal of Power Sources. 171 (2007) 783-788. <http://www.sciencedirect.com>

130. R. Arroyave. L. Kaufman. T. Edgar. "Thermodynamic Modeling of the Zr-O System". <u>Calphad</u>. 26, 1 (2002) 95-118. <http://www.sciencedirect.com>

131. M. Yashima, M. Kakihana, M. Yoshimura. "Metastable-Stable Phase Diagrams in the Zirconia Containing Systems Utilized in Solid Oxide Fuel Cell Application". <u>Solid State Ionics</u>. 86-88 (1996) 1131-1149. <http://www.sciencedirect.com>

132. V. Y. Shevchenko, et al. "Structural Features of Ultrafine Zirconia as Probed by Synchrotron X-Ray Diffraction". <u>Doklady Physical Chemistry</u>. 377, 4-6 (2001) 121-123. <http://www.springerlink.com>

133. P.C. Rivas, et al. "PAC Study of Zirconias Produced by the Sol-Gel Method". <u>Journal of the American Ceramic Society</u>. 78 (1995) 1329-1334.

134. L.C. Klein, et al. "Microporous Oxides by the Sol-Gel Process: Synthesis and Applications". <u>Catalysis Today</u>. 14 (1992) 165.

135. S.D. Kim, et al. "Effects of Anode and Electrolyte Microstructures on Performance of Solid Oxide Fuel Cells". <u>Journal of Power Sources</u>. 169 (2007) 265-270. <http://www.sciencedirect.com>

136. R. Vassen, et al. "Manufacturing of High Performance Solid Oxide Fuel Cells (SOFCs) with Atmospheric Plasma Spraying (APS)". <u>Surface & Coatings Technology</u>. 202 (2007) 499-508. <http://www.sciencedirect.com>

137. C. Lee, J. Bae. "Fabrication and Characterization of Metal-Supported Solid Oxide Fuel Cells". <u>Journal of Power Sources</u>. 176 (2008) 62-69. <http://www.sciencedirect.com>

APPENDIX

Table 8: List of materials

	Component	Vendor	Product #	CAS#
Substrate	Pressed Alumina Thimble	Fisher Scientific	09960E-AL889	
LSM	Lanthanum Chloride (LaCl3*7H2O)	Fisher Scientific	L9-250	10025-84-0
	Manganese Acetate (Mn(CH3OO2)*4H2O)	Alfa Aesar	12351	6156-78-1
	Strontium Nitrate (Sr(NO3)2)	Fisher Scientific	S549-100	10042-76-9
	Citric Acid (C6H8O7)	Fisher Scientific	A940-500	77-92-9
	Ethylene Glycol (C2H6O2)	Fluka	03770	107-21-1
YSZ	Yttrium Nitrate (Y(NO$_3$)$_3$*6H$_2$O)	Alfa Aesar	12898	13494-98-9
	Zirconium Oxychloride (ZrOCl2*nH2O)	Magnesium Elektron, Inc.		7699-43-6
Pt	Pt Paste	Heraeus	LP11-4493	
	Conductrox Paste	Ferro	3804	
Misc	Ammonium Hydroxide (NH4OH)	Fisher Scientific	A669-500	1336-21-6
	Anhydrous Ethyl Alcohol	Fisher Scientific	A405F-1GAL	64-17-5
	Omega Bond Cement	Omega Engineering, Inc.	OB-600	
	Aremco Seal	Aremco Products	617	

CURRICULUM VITAE

Joshua S. Finch

1980	**Born April 12th** **Portsmouth, Virginia**
1994-1998	**Howell High School** **Farmingdale, New Jersey**
1998-2003	**B.S. in Ceramic and Materials Engineering,** **Rutgers, The State University of New Jersey** **Piscataway, New Jersey**
2000-2001	**Project Assistant, Ceramic Engineering Department,** **Rutgers, The State University of New Jersey** **Piscataway, New Jersey**
2001-2003	**Undergraduate Technician, Ceramic Engineering Department,** **Rutgers, The State University of New Jersey** **Piscataway, New Jersey**
2003-2006	**M.S. in Ceramic and Materials Engineering,** **Rutgers, The State University of New Jersey** **New Brunswick, New Jersey**
2003-2007	**Teaching Assistant, General Engineering Department,** **"Introduction to Computers for Engineers"** **Rutgers, The State University of New Jersey** **Piscataway, New Jersey**
2005-2007	**Teaching Assistant, Ceramic Engineering Department,** **"Venture Analysis"** **Rutgers, The State University of New Jersey** **Piscataway, New Jersey**

2007-2008   **Course Coordinator, Dean's Office, School of Engineering,**
                    "Introduction to Computers for Engineers"
                    Rutgers, The State University of New Jersey
                    Piscataway, New Jersey

2003-2008   **Graduate Technician, Ceramic and Materials Department,**
                    Rutgers, The State University of New Jersey
                    Piscataway, New Jersey

2008   **Ph.D in Materials Science and Engineering,**
                    Rutgers, The State University of New Jersey
                    New Brunswick, New Jersey

Papers:

R. Chandran, J. Finch, D. Parekh, L.C. Klein, *"Sol-Gel Thin Film YSZ for Oxygen Generation/Removal and Solid Oxide Fuel Cell Applications"*, **Paper S1 -1693 Symposium S1, "Fifth International Symposium on Ionic and Mixed Conducting Ceramics", 206th Meeting of The Electrochemical Society in Honolulu, HI from October 3-8, 2004.**

R. Chandran, L.C. Klein, and J. Finch, *"Sol-Gel Processed Multilayer Thin Film Design for Solid Oxide Fuel Cell Applications"*, **Paper 1107, "Ninth International Symposium on Solid Oxide Fuel Cells", 207th Meeting of The Electrochemical Society in Quebec City, Canada from May 15-20, 2005.**

Technical Presentations:

J. Finch, L.C. Klein, R. Chandran, *"Sol-Gel Processed Yttria-Stabilized Zirconia (YSZ) for Oxygen Generation"*, **Session, "Solid Electrolytes: Oxide-Ion and Proton Conductors" Symposium S16, "International Symposium on Fuel Cells and Related Systems", 107th Annual Meeting and Exposition of The American Ceramic Society in Baltimore, MD from April 10-13, 2005.**

H. Crawford, D. Kienzle, J. Finch, T. Tirrell, E.S. Willoughby, A. Mendoza, B. Ellerbrock, *"Crystal and the 20-Something Generation"*, **Presentation to the XVII Technical Exchange Conference of the International Crystal Federation in Telfs, Austria, October 7, 2005.**

H. Crawford, D. Kienzle, J. Finch, T. Tirrell, E.S. Willoughby, A. Mendoza, B. Ellerbrock, R. Carpenter, *"Young Adults and Crystal"*, Presentation to the Scandinavian Glass Federation Annual Conference in Oslo, Norway, May 29, 2006.

H. Crawford, D. Kienzle, J. Finch, T. Tirrell, E.S. Willoughby, A. Mendoza, B. Ellerbrock, R. Carpenter, *"Reformulated Crystal: Friend or Foe of the Crystal Industry"*, Presentation to the Scandinavian Glass Federation Annual Conference in Oslo, Norway, May 29, 2006.

H. Crawford, D. Kienzle, J. Finch, T. Tirrell, E.S. Willoughby, A. Mendoza, B. Ellerbrock, R. Carpenter, R. Lehman, *"Physical and Chemical Assessment of Selected Glassware from the USA Market"*, Presentation to the XVIII Technical Exchange Conference in Weiden, Germany, October 8, 2006.

H. Crawford, R. Lehman, J. Pantina, T. Tirrell, J. Finch, *"Reengineering Beauty: The Pros and Cons of Current Crystal Glass Manufacturing Methods Designed to Reduce Lead Migration"*, Presentation to the XVIV Technical Exchange Conference in Siena, Italy, November 4, 2007.